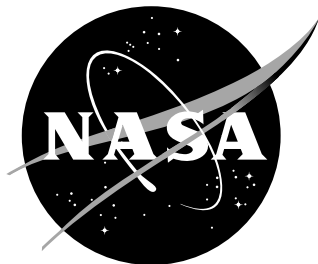


NASA/TM-2016-219348



Wind Tunnel Test of a Risk-Reduction Wing/Fuselage Model to Examine Juncture-Flow Phenomena

Michael A. Kegerise and Dan H. Neuhart
Langley Research Center, Hampton, Virginia

NASA STI Program . . . in Profile

Since its founding, NASA has been dedicated to the advancement of aeronautics and space science. The NASA scientific and technical information (STI) program plays a key part in helping NASA maintain this important role.

The NASA STI program operates under the auspices of the Agency Chief Information Officer. It collects, organizes, provides for archiving, and disseminates NASA's STI. The NASA STI program provides access to the NTRS Registered and its public interface, the NASA Technical Reports Server, thus providing one of the largest collections of aeronautical and space science STI in the world. Results are published in both non-NASA channels and by NASA in the NASA STI Report Series, which includes the following report types:

- **TECHNICAL PUBLICATION.** Reports of completed research or a major significant phase of research that present the results of NASA Programs and include extensive data or theoretical analysis. Includes compilations of significant scientific and technical data and information deemed to be of continuing reference value. NASA counter-part of peer-reviewed formal professional papers but has less stringent limitations on manuscript length and extent of graphic presentations.
- **TECHNICAL MEMORANDUM.** Scientific and technical findings that are preliminary or of specialized interest, e.g., quick release reports, working papers, and bibliographies that contain minimal annotation. Does not contain extensive analysis.
- **CONTRACTOR REPORT.** Scientific and technical findings by NASA-sponsored contractors and grantees.

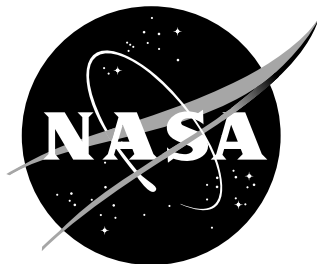
- **CONFERENCE PUBLICATION.** Collected papers from scientific and technical conferences, symposia, seminars, or other meetings sponsored or co-sponsored by NASA.
- **SPECIAL PUBLICATION.** Scientific, technical, or historical information from NASA programs, projects, and missions, often concerned with subjects having substantial public interest.
- **TECHNICAL TRANSLATION.** English-language translations of foreign scientific and technical material pertinent to NASA's mission.

Specialized services also include organizing and publishing research results, distributing specialized research announcements and feeds, providing information desk and personal search support, and enabling data exchange services.

For more information about the NASA STI program, see the following:

- Access the NASA STI program home page at <http://www.sti.nasa.gov>
- E-mail your question to help@sti.nasa.gov
- Phone the NASA STI Information Desk at 757-864-9658
- Write to:
NASA STI Information Desk
Mail Stop 148
NASA Langley Research Center
Hampton, VA 23681-2199

NASA/TM-2016-219348



Wind Tunnel Test of a Risk-Reduction Wing/Fuselage Model to Examine Juncture-Flow Phenomena

Michael A. Kegerise and Dan H. Neuhart
Langley Research Center, Hampton, Virginia

National Aeronautics and
Space Administration

Langley Research Center
Hampton, Virginia 23681-2199

November 2016

The use of trademarks or names of manufacturers in this report is for accurate reporting and does not constitute an official endorsement, either expressed or implied, of such products or manufacturers by the National Aeronautics and Space Administration.

Available from:

NASA STI Program / Mail Stop 148
NASA Langley Research Center
Hampton, VA 23681-2199
Fax: 757-864-6500

Abstract

A wing/fuselage wind-tunnel model was tested in the Langley 14- by 22-foot Subsonic Wind Tunnel in preparation for a highly-instrumented Juncture Flow Experiment to be conducted in the same facility. This test, which was sponsored by the NASA Transformational Tool and Technologies Project, is part of a comprehensive set of experimental and computational research activities to develop revolutionary, physics-based aeronautics analysis and design capability. The objectives of this particular test were to examine the surface and off-body flow on a generic wing/body combination to: 1) choose a final wing for a future, highly instrumented model, 2) use the results to facilitate unsteady pressure sensor placement on the model, 3) determine the area to be surveyed with an embedded laser-doppler velocimetry (LDV) system, 4) investigate the primary juncture corner-flow separation region using particle image velocimetry (PIV) to see if the particle seeding is adequately entrained and to examine the structure in the separated region, and 5) to determine the similarity of observed flow features with those predicted by computational fluid dynamics (CFD). This report documents the results of the above experiment that specifically address the first three goals.

Multiple wing configurations were tested at a chord Reynolds number of 2.4 million. Flow patterns on the surface of the wings and in the region of the wing/fuselage juncture were examined using oil-flow visualization and infrared thermography. A limited number of unsteady pressure sensors on the fuselage around the wing leading and trailing edges were used to identify any dynamic effects of the horseshoe vortex on the flow field. The area of separated flow in the wing/fuselage juncture near the wing trailing edge was observed for all wing configurations at various angles of attack. All of the test objectives were met. The staff of the 14- by 22-foot Subsonic Wind Tunnel provided outstanding support and delivered exceptional value to the experiment, which exceeded expectations.

The results of this test will directly inform the planning for the first of a series of instrumented-model tests at the same Reynolds number. These tests will be performed on a slightly larger-scale model with the selected wing, and will include off-body measurements with LDV and PIV, steady and unsteady pressure measurements, and the flow-visualization techniques that are discussed in this report.

Contents

Nomenclature	3
List of Tables	4
List of Figures	5
1 Introduction	13
2 Experimental Methods	14
2.1 14- by 22-Foot Subsonic Wind Tunnel	14
2.2 Juncture-Flow Model	14
2.3 Infrared Imaging	15
2.4 Oil-Flow Visualization	15
2.5 Unsteady Measurements	16
3 Data Analysis Methods	17
4 Results	19
4.1 Flow Visualization Results	19
4.1.1 Configuration 1: F6 Wing and F6 Wing with Leading-Edge Horn	19
4.1.2 Configuration 2: NACA 0015 Wing and NACA 0015mod Wing	22
4.1.3 Configuration 3: F6 S12 Wing and COCA Wing	24
4.1.4 Configuration 4: F6 Wings with Leading-Edge Horns	24
4.2 Unsteady Pressure Results	25
4.2.1 F6 Wing	25
4.2.2 F6 Wing with Leading-Edge Horn	27
4.2.3 NACA 0015 Wing	27
4.2.4 F6 S12 Wing	28
4.3 Accelerometer Results	29
5 Conclusions	29
References	30
Appendix A. Uncertainty Analysis	32

Nomenclature

a	acceleration
c	chord length at wing break
d_k	primary input to adaptive noise canceler at time step k
f	frequency
G	filter gain
G_{aa}	auto-spectral density of acceleration
G_{pp}	auto-spectral density of fluctuating pressure
k	filter time step in samples
ℓ	length of corner-flow separation
L	filter length
N	number of independent samples
p	fluctuating pressure
q_∞	freestream dynamic pressure, $q_\infty = \rho_\infty U_\infty^2 / 2$
Re_c	Reynolds number based on chord length at wing break
Re_s	Reynolds number based on distance along surface
RMS	root-mean-squared value
R_{pp}	autocorrelation of the unsteady pressure
s	distance along surface or static sensitivity of pressure sensor
St	Strouhal number, ft/U_∞
t	thickness of wing trailing edge
T	maximum thickness of wing-root section
T_p	integral time scale of unsteady pressure
U_ℓ	uncertainty in the corner-flow separation length measurement
U_w	uncertainty in the corner-flow separation width measurement
U_∞	freestream velocity
v	voltage
w	width of corner-flow separation
\mathbf{W}_k	filter weight vector at time step k
x	streamwise distance from model nose tip
x_k	filter input at time step k
\mathbf{X}_k	filter input vector at time step k
y	spanwise distance from model nose tip
y_k	filter output at time step k
z	flow-normal distance from model nose tip
α	model angle of attack
δ	boundary-layer thickness
ε_k	error signal in adaptive noise canceler at time step k
μ	gain constant in adaptive noise canceler algorithm
μ_r	exact r th-order central moment of a probability distribution
ρ_∞	freestream density
σ_p	standard deviation of the unsteady pressure
<i>Operators</i>	
$\bar{(\cdot)}$	mean value
$E[\cdot]$	expected value

List of Tables

1	Juncture-flow model wing configurations and nominal angles of attack.	35
2	Unsteady pressure sensor locations on the juncture-flow model fuselage.	35
3	Measured widths and lengths (with uncertainties) of the corner-flow separation for the F6 wing (port side). Configuration 1 at $Re_c = 2.4$ million.	36
4	Measured widths and lengths (with uncertainties) of the corner-flow separation for the F6 wing with leading-edge horn (starboard side). Configuration 1 at $Re_c = 2.4$ million.	36
5	Measured widths and lengths (with uncertainties) of the corner-flow separation for the NACA 0015 wing (port side). Configuration 2 at $Re_c = 2.4$ million.	36
6	Measured widths and lengths (with uncertainties) of the corner-flow separation for the NACA 0015mod wing (starboard side). Configuration 2 at $Re_c = 2.4$ million.	37
7	Measured widths and lengths (with uncertainties) of the corner-flow separation for the F6 wing with leading-edge horn (port side). Configuration 4 at $Re_c = 2.4$ million.	37
8	Measured widths and lengths (with uncertainties) of the corner-flow separation for the F6 wing with leading-edge horn (port side). Configuration 4 at $Re_c = 2.7$ million.	37
9	Measured widths and lengths (with uncertainties) of the corner-flow separation for the F6 wing with leading-edge horn (starboard side). Configuration 4 at $Re_c = 2.7$ million.	37

List of Figures

1	Image of the Juncture-Flow Model installed in the 14x22 Subsonic Wind Tunnel.	38
2	Front-view image of the Juncture-Flow Model installed in the 14x22 Subsonic Wind Tunnel.	38
3	Wing root section profiles. The numbered circular symbols denote the locations of the pressure transducers on the port side of the fuselage and the solid black lines in each figure denote the top and bottom of the fuselage.	39
4	Example pictures of trip-dot placement on the juncture-flow model.	40
5	Definition of corner-flow separation length, ℓ , and width, w , from an example oil-flow visualization (F6 wing with leading edge horn, $\alpha = 5^\circ$, $Re_c = 2.4$ million).	40
6	Auto spectral density of pressure sensor 1 versus angle of attack. F6 wing at $Re_c = 2.4$ million.	41
7	Block diagram of adaptive noise cancellation method for removal of facility background noise.	41
8	Infrared images of the port-side fuselage versus model angle of attack. The model was clean (no trip elements). F6 wing geometry (configuration 1) at $Re_c = 2.4$ million.	42
9	Infrared images of the port-side fuselage versus model angle of attack. The fuselage boundary layer was tripped with $218.4 \mu\text{m}$ trip dots located at an arc-distance of 30.48 cm from the model nose tip. F6 wing geometry (configuration 1) at $Re_c = 2.4$ million.	43
10	Infrared images of the F6 wing with leading-edge horn (starboard side) versus model angle of attack. The wing surface was clean (no trip elements) and the fuselage boundary layer was tripped. F6 wing geometry (configuration 1) at $Re_c = 2.4$ million.	44
11	Infrared images of the F6 wing with leading-edge horn (starboard side) versus model angle of attack. The wing surface was tripped at 1.6% chord with $142.2 \mu\text{m}$ trip dots and the fuselage boundary layer was tripped. F6 wing geometry (configuration 1) at $Re_c = 2.4$ million.	45
12	Infrared images of the F6 wing (port side) versus model angle of attack. The wing surface was tripped at 1.6% chord with $142.2 \mu\text{m}$ trip dots and the fuselage boundary layer was tripped. F6 wing geometry (configuration 1) at $Re_c = 2.4$ million.	46
13	Planform view of the oil-flow visualization for configuration 1 versus model angle of attack. The F6 wing is on the port side and the F6 wing with leading-edge horn is on the starboard side. $Re_c = 2.4$ million.	47
14	Oil-flow visualizations in the trailing-edge corner region of the F6 wing (port side) versus model angle of attack. F6 wing geometry (configuration 1) at $Re_c = 2.4$ million.	48
15	Oil-flow visualizations in the trailing-edge corner region of the F6 wing with leading-edge horn (starboard side) versus model angle of attack. F6 wing geometry (configuration 1) at $Re_c = 2.4$ million.	49
16	Corner-flow separation width versus model angle of attack for the F6 wing and the F6 wing with leading-edge horn (configuration 1). $Re_c = 2.4$ million.	50
17	Corner-flow separation length versus model angle of attack for the F6 wing and the F6 wing with leading-edge horn (configuration 1). $Re_c = 2.4$ million.	50
18	Oil-flow visualizations at the leading edge of the F6 wing (port side) versus model angle of attack. F6 wing geometry (configuration 1) at $Re_c = 2.4$ million.	51
19	Oil-flow visualization in the leading-edge region of the F6 wing at $\alpha = 5^\circ$ and $Re_c = 2.4$ million.	52

20	Close-up image of the oil-flow visualization in the leading-edge region of the F6 wing at $\alpha = 5^\circ$ and $Re_c = 2.4$ million.	52
21	Oil-flow visualizations at the leading edge of the F6 wing with leading-edge horn (starboard side) versus model angle of attack. F6 wing geometry (configuration 1) at $Re_c = 2.4$ million.	53
22	Oil-flow visualizations of the trailing-edge separation induced by a flow structure emanating from the F6 leading-edge horn. $Re_c = 2.4$ million.	54
23	Oil-flow visualization showing the footprint of the vortical structures associated with trip dots that are not fully effective. F6 wing with leading-edge horn at $\alpha = -7.5^\circ$ and $Re_c = 2.4$ million.	54
24	Effect of Reynolds number on the surface-flow topology of the F6 wing (port side) and the F6 wing with leading-edge horn (starboard side). Configuration 1 at $\alpha = 5^\circ$.	55
25	Infrared images of the NACA 0015mod wing (starboard side) versus model angle of attack. The wing surface was clean (no trip elements) and the fuselage boundary layer was tripped. Configuration 2 at $Re_c = 2.4$ million.	56
26	Infrared images of the NACA 0015mod wing (starboard side) versus model angle of attack. The wing surface was tripped at 6.4% chord with $142.2 \mu\text{m}$ trip dots and the fuselage boundary layer was tripped. Configuration 2 at $Re_c = 2.4$ million.	57
27	Infrared images of the NACA 0015 wing (port side) versus model angle of attack. The wing surface was clean (no trip elements) and the fuselage boundary layer was tripped. Configuration 2 at $Re_c = 2.4$ million.	58
28	Infrared images of the NACA 0015 wing (port side) versus model angle of attack. The wing surface was tripped at 6.4% chord with $142.2 \mu\text{m}$ trip dots and the fuselage boundary layer was tripped. Configuration 2 at $Re_c = 2.4$ million.	59
29	Planform view of the oil-flow visualization for configuration 2 versus model angle of attack. The NACA 0015 wing is on the port side and the NACA 0015mod wing is on the starboard side. $Re_c = 2.4$ million.	60
30	Oil-flow visualizations in the trailing-edge corner region of the NACA 0015 wing (port side) versus model angle of attack. Configuration 2 at $Re_c = 2.4$ million.	61
31	Oil-flow visualizations in the trailing-edge corner region of the NACA 0015mod wing (starboard side) versus model angle of attack. Configuration 2 at $Re_c = 2.4$ million.	62
32	Corner-flow separation width versus model angle of attack for the F6 wings (configuration 1) and the NACA 0015 wings (configuration 2). $Re_c = 2.4$ million.	63
33	Corner-flow separation length versus model angle of attack for the F6 wings (configuration 1) and the NACA 0015 wings (configuration 2). $Re_c = 2.4$ million.	63
34	Effect of Reynolds number on the surface-flow topology of the NACA 0015 wing (port side) and the NACA 0015mod wing (starboard side). Configuration 2 at $\alpha = 10^\circ$.	64
35	Infrared images of the COCA wing (starboard side) versus model angle of attack. The wing surface was clean (no trip elements) and the fuselage boundary layer was tripped. Configuration 3 at $Re_c = 2.4$ million.	65
36	Infrared images of the COCA wing (starboard side) versus model angle of attack. The wing surface was tripped at 1.6% chord with $182.9 \mu\text{m}$ trip dots and the fuselage boundary layer was tripped. Configuration 3 at $Re_c = 2.4$ million.	66

37	Infrared images of the F6 S12 wing (port side) versus model angle of attack. The wing surface was clean (no trip elements) and the fuselage boundary layer was tripped. Configuration 3 at $Re_c = 2.4$ million.	67
38	Infrared images of the F6 S12 wing (port side) versus model angle of attack. The wing surface was tripped at 1.6% chord with $182.9 \mu\text{m}$ trip dots and the fuselage boundary layer was tripped. Configuration 3 at $Re_c = 2.4$ million.	68
39	Planform view of the oil-flow visualization for configuration 3 versus model angle of attack. The F6 S12 wing is on the port side and the COCA wing is on the starboard side. $Re_c = 2.4$ million.	69
40	Oil-flow visualizations in the trailing-edge corner region of the F6 S12 wing (port side) versus model angle of attack. Configuration 3 at $Re_c = 2.4$ million.	70
41	Oil-flow visualizations in the trailing-edge corner region of the COCA wing (port side) versus model angle of attack. Configuration 3 at $Re_c = 2.4$ million.	71
42	Planform view of the oil-flow visualization for configuration 4 versus model angle of attack. Both F6 wings were configured with the leading-edge horn. $Re_c = 2.4$ million.	72
43	Oil-flow visualizations in the trailing-edge corner region of the F6 wings with leading-edge horn. Configuration 4 at $\alpha = 5^\circ$ and $Re_c = 2.4$ million.	73
44	Corner-flow separation width versus model angle of attack for the F6 wings with leading-edge horn (configuration 4). $Re_c = 2.4$ million.	74
45	Corner-flow separation length versus model angle of attack for the F6 wings with leading-edge horn (configuration 4). $Re_c = 2.4$ million.	74
46	Effect of Reynolds number on the corner-flow separation width of the F6 wings with leading-edge horn (configuration 4).	75
47	Effect of Reynolds number on the corner-flow separation length of the F6 wings with leading-edge horn (configuration 4).	75
48	Pressure sensor locations in the the leading-edge region of the F6 wing. Oil-flow visualization at $\alpha = 5^\circ$ and $Re_c = 2.4$ million.	76
49	Pressure sensor locations in the the leading-edge region of the F6 wing with leading-edge horn. Oil-flow visualization at $\alpha = 5^\circ$ and $Re_c = 2.4$ million.	76
50	Auto spectral density of pressure sensor 1 versus angle of attack. F6 wing at $Re_c = 2.4$ million, with pressure sensor 2 as a reference for facility noise removal.	77
51	Probability density of pressure sensor 1 versus angle of attack. F6 wing at $Re_c = 2.4$ million, with pressure sensor 2 as a reference for facility noise removal.	77
52	Auto spectral density of pressure sensor 3 versus angle of attack. F6 wing at $Re_c = 2.4$ million, with pressure sensor 2 as a reference for facility noise removal.	78
53	Probability density of pressure sensor 3 versus angle of attack. F6 wing at $Re_c = 2.4$ million, with pressure sensor 2 as a reference for facility noise removal.	78
54	Auto spectral density of pressure sensor 4 versus angle of attack. F6 wing at $Re_c = 2.4$ million, with pressure sensor 2 as a reference for facility noise removal.	79
55	Probability density of pressure sensor 4 versus angle of attack. F6 wing at $Re_c = 2.4$ million, with pressure sensor 2 as a reference for facility noise removal.	79
56	RMS for pressure sensors 1, 3, and 4 versus angle of attack. F6 wing at $Re_c = 2.4$ million, with pressure sensor 2 as a reference for facility noise removal.	80

57	Skewness for pressure sensors 1, 3, and 4 versus angle of attack. F6 wing at $Re_c = 2.4$ million, with pressure sensor 2 as a reference for facility noise removal.	80
58	Flatness for pressure sensors 1, 3, and 4 versus angle of attack. F6 wing at $Re_c = 2.4$ million, with pressure sensor 2 as a reference for facility noise removal.	81
59	Auto spectral density of pressure sensor 7 versus angle of attack. F6 wing at $Re_c = 2.4$ million, with pressure sensor 6 as a reference for facility noise removal.	82
60	Probability density of pressure sensor 7 versus angle of attack. F6 wing at $Re_c = 2.4$ million, with pressure sensor 6 as a reference for facility noise removal.	82
61	Auto spectral density of pressure sensor 8 versus angle of attack. F6 wing at $Re_c = 2.4$ million, with pressure sensor 6 as a reference for facility noise removal.	83
62	Probability density of pressure sensor 8 versus angle of attack. F6 wing at $Re_c = 2.4$ million, with pressure sensor 6 as a reference for facility noise removal.	83
63	Auto spectral density of pressure sensor 9 versus angle of attack. F6 wing at $Re_c = 2.4$ million, with pressure sensor 6 as a reference for facility noise removal.	84
64	Probability density of pressure sensor 9 versus angle of attack. F6 wing at $Re_c = 2.4$ million, with pressure sensor 6 as a reference for facility noise removal.	84
65	Auto spectral density of pressure sensor 10 versus angle of attack. F6 wing at $Re_c = 2.4$ million, with pressure sensor 6 as a reference for facility noise removal.	85
66	Probability density of pressure sensor 10 versus angle of attack. F6 wing at $Re_c = 2.4$ million, with pressure sensor 6 as a reference for facility noise removal.	85
67	RMS for pressure sensors 7, 8, 9, and 10 versus angle of attack. F6 wing at $Re_c = 2.4$ million, with pressure sensor 6 as a reference for facility noise removal.	86
68	Skewness for pressure sensors 7, 8, 9, and 10 versus angle of attack. F6 wing at $Re_c = 2.4$ million, with pressure sensor 6 as a reference for facility noise removal.	86
69	Flatness for pressure sensors 7, 8, 9, and 10 versus angle of attack. F6 wing at $Re_c = 2.4$ million, with pressure sensor 6 as a reference for facility noise removal.	87
70	Auto spectral density of pressure sensor 11 versus angle of attack. F6 wing at $Re_c = 2.4$ million, with pressure sensor 14 as a reference for facility noise removal.	88
71	Probability density of pressure sensor 11 versus angle of attack. F6 wing at $Re_c = 2.4$ million, with pressure sensor 14 as a reference for facility noise removal.	88
72	Auto spectral density of pressure sensor 12 versus angle of attack. F6 wing at $Re_c = 2.4$ million, with pressure sensor 14 as a reference for facility noise removal.	89
73	Probability density of pressure sensor 12 versus angle of attack. F6 wing at $Re_c = 2.4$ million, with pressure sensor 14 as a reference for facility noise removal.	89

74	Auto spectral density of pressure sensor 13 versus angle of attack. F6 wing at $Re_c = 2.4$ million, with pressure sensor 14 as a reference for facility noise removal.	90
75	Probability density of pressure sensor 13 versus angle of attack. F6 wing at $Re_c = 2.4$ million, with pressure sensor 14 as a reference for facility noise removal.	90
76	RMS for pressure sensors 11, 12, and 13 versus angle of attack. F6 wing at $Re_c = 2.4$ million, with pressure sensor 14 as a reference for facility noise removal.	91
77	Skewness for pressure sensors 11, 12, and 13 versus angle of attack. F6 wing at $Re_c = 2.4$ million, with pressure sensor 14 as a reference for facility noise removal.	91
78	Flatness for pressure sensors 7, 8, 9, and 10 versus angle of attack. F6 wing at $Re_c = 2.4$ million, with pressure sensor 14 as a reference for facility noise removal.	92
79	Auto spectral density of pressure sensor 1 versus angle of attack. F6 wing with leading-edge horn at $Re_c = 2.4$ million, with pressure sensor 2 as a reference for facility noise removal.	93
80	Auto spectral density of pressure sensor 4 versus angle of attack. F6 wing with leading-edge horn at $Re_c = 2.4$ million, with pressure sensor 2 as a reference for facility noise removal.	93
81	RMS for pressure sensors 1 and 4 versus angle of attack. F6 wing with leading-edge horn at $Re_c = 2.4$ million, with pressure sensor 2 as a reference for facility noise removal.	94
82	Skewness for pressure sensors 1 and 4 versus angle of attack. F6 wing with leading-edge horn at $Re_c = 2.4$ million, with pressure sensor 2 as a reference for facility noise removal.	94
83	Flatness for pressure sensors 1 and 4 versus angle of attack. F6 wing with leading-edge horn at $Re_c = 2.4$ million, with pressure sensor 2 as a reference for facility noise removal.	95
84	Auto spectral density of pressure sensor 7 versus angle of attack. F6 wing with leading-edge horn at $Re_c = 2.4$ million, with pressure sensor 6 as a reference for facility noise removal.	96
85	Auto spectral density of pressure sensor 8 versus angle of attack. F6 wing with leading-edge horn at $Re_c = 2.4$ million, with pressure sensor 6 as a reference for facility noise removal.	96
86	Auto spectral density of pressure sensor 9 versus angle of attack. F6 wing with leading-edge horn at $Re_c = 2.4$ million, with pressure sensor 6 as a reference for facility noise removal.	97
87	Auto spectral density of pressure sensor 10 versus angle of attack. F6 wing with leading-edge horn at $Re_c = 2.4$ million, with pressure sensor 6 as a reference for facility noise removal.	97
88	RMS for pressure sensors 7, 8, 9, and 10 versus angle of attack. F6 wing with leading-edge horn at $Re_c = 2.4$ million, with pressure sensor 6 as a reference for facility noise removal.	98
89	Skewness for pressure sensors 7, 8, 9, and 10 versus angle of attack. F6 wing with leading-edge horn at $Re_c = 2.4$ million, with pressure sensor 6 as a reference for facility noise removal.	98
90	Flatness for pressure sensors 7, 8, 9, and 10 versus angle of attack. F6 wing with leading-edge horn at $Re_c = 2.4$ million, with pressure sensor 6 as a reference for facility noise removal.	99

91	Auto spectral density of pressure sensor 11 versus angle of attack. F6 wing with leading-edge horn at $Re_c = 2.4$ million, with pressure sensor 14 as a reference for facility noise removal.	99
92	Auto spectral density of pressure sensor 12 versus angle of attack. F6 wing with leading-edge horn at $Re_c = 2.4$ million, with pressure sensor 14 as a reference for facility noise removal.	100
93	Auto spectral density of pressure sensor 13 versus angle of attack. F6 wing with leading-edge horn at $Re_c = 2.4$ million, with pressure sensor 14 as a reference for facility noise removal.	100
94	RMS for pressure sensors 11, 12, and 13 versus angle of attack. F6 wing with leading-edge horn at $Re_c = 2.4$ million, with pressure sensor 14 as a reference for facility noise removal.	101
95	Skewness for pressure sensors 11, 12, and 13 versus angle of attack. F6 wing with leading-edge horn at $Re_c = 2.4$ million, with pressure sensor 14 as a reference for facility noise removal.	101
96	Flatness for pressure sensors 7, 8, 9, and 10 versus angle of attack. F6 wing with leading-edge horn at $Re_c = 2.4$ million, with pressure sensor 14 as a reference for facility noise removal.	102
97	Auto spectral density of pressure sensor 2 versus angle of attack. NACA 0015 wing with leading-edge horn at $Re_c = 2.4$ million, with pressure sensor 1 as a reference for facility noise removal.	103
98	Auto spectral density of pressure sensor 3 versus angle of attack. NACA 0015 wing with leading-edge horn at $Re_c = 2.4$ million, with pressure sensor 1 as a reference for facility noise removal.	103
99	RMS for pressure sensors 2 and 3 versus angle of attack. NACA 0015 with leading-edge horn at $Re_c = 2.4$ million, with pressure sensor 1 as a reference for facility noise removal.	104
100	Skewness for pressure sensors 2 and 3 versus angle of attack. NACA 0015 with leading-edge horn at $Re_c = 2.4$ million, with pressure sensor 1 as a reference for facility noise removal.	104
101	Flatness for pressure sensors 2 and 3 versus angle of attack. NACA 0015 with leading-edge horn at $Re_c = 2.4$ million, with pressure sensor 1 as a reference for facility noise removal.	105
102	Auto spectral density of pressure sensor 8 versus angle of attack. NACA 0015 wing with leading-edge horn at $Re_c = 2.4$ million, with pressure sensor 6 as a reference for facility noise removal.	106
103	Auto spectral density of pressure sensor 9 versus angle of attack. NACA 0015 wing with leading-edge horn at $Re_c = 2.4$ million, with pressure sensor 6 as a reference for facility noise removal.	106
104	Auto spectral density of pressure sensor 10 versus angle of attack. NACA 0015 wing with leading-edge horn at $Re_c = 2.4$ million, with pressure sensor 14 as a reference for facility noise removal.	107
105	Auto spectral density of pressure sensor 11 versus angle of attack. NACA 0015 wing with leading-edge horn at $Re_c = 2.4$ million, with pressure sensor 14 as a reference for facility noise removal.	107
106	RMS for pressure sensors 8, 9, 10 and 11 versus angle of attack. NACA 0015 with leading-edge horn at $Re_c = 2.4$ million, with pressure sensors 6 (for sensors 8 and 9) and 14 (for sensors 10 and 11) as references for facility noise removal.	108

107	Skewness for pressure sensors 8, 9, 10 and 11 versus angle of attack. NACA 0015 with leading-edge horn at $Re_c = 2.4$ million, with pressure sensors 6 (for sensors 8 and 9) and 14 (for sensors 10 and 11) as references for facility noise removal.	108
108	Flatness for pressure sensors 8, 9, 10 and 11 versus angle of attack. NACA 0015 with leading-edge horn at $Re_c = 2.4$ million, with pressure sensors 6 (for sensors 8 and 9) and 14 (for sensors 10 and 11) as references for facility noise removal.	109
109	Auto spectral density of pressure sensors 8, 9, 10, and 11 at $\alpha = 0^\circ$. NACA 0015 wing with leading-edge horn at $Re_c = 2.4$ million, with pressure sensors 6 (for sensors 8 and 9) and 14 (for sensors 10 and 11) as references for facility noise removal.	109
110	Auto spectral density of pressure sensor 2 versus angle of attack. F6 S12 wing with leading-edge horn at $Re_c = 2.4$ million, with pressure sensor 1 as a reference for facility noise removal.	110
111	Auto spectral density of pressure sensor 3 versus angle of attack. F6 S12 wing with leading-edge horn at $Re_c = 2.4$ million, with pressure sensor 1 as a reference for facility noise removal.	110
112	RMS for pressure sensors 2 and 3 versus angle of attack. F6 S12 with leading-edge horn at $Re_c = 2.4$ million, with pressure sensor 1 as a reference for facility noise removal.	111
113	Skewness for pressure sensors 2 and 3 versus angle of attack. F6 S12 with leading-edge horn at $Re_c = 2.4$ million, with pressure sensor 1 as a reference for facility noise removal.	111
114	Flatness for pressure sensors 2 and 3 versus angle of attack. F6 S12 with leading-edge horn at $Re_c = 2.4$ million, with pressure sensor 1 as a reference for facility noise removal.	112
115	Auto spectral density of pressure sensor 8 versus angle of attack. F6 S12 wing with leading-edge horn at $Re_c = 2.4$ million, with pressure sensor 6 as a reference for facility noise removal.	113
116	Auto spectral density of pressure sensor 9 versus angle of attack. F6 S12 wing with leading-edge horn at $Re_c = 2.4$ million, with pressure sensor 6 as a reference for facility noise removal.	113
117	Auto spectral density of pressure sensor 10 versus angle of attack. F6 S12 wing with leading-edge horn at $Re_c = 2.4$ million, with pressure sensor 14 as a reference for facility noise removal.	114
118	Auto spectral density of pressure sensor 11 versus angle of attack. F6 S12 wing with leading-edge horn at $Re_c = 2.4$ million, with pressure sensor 14 as a reference for facility noise removal.	114
119	RMS for pressure sensors 8, 9, 10 and 11 versus angle of attack. F6 S12 with leading-edge horn at $Re_c = 2.4$ million, with pressure sensors 6 (for sensors 8 and 9) and 14 (for sensors 10 and 11) as references for facility noise removal.	115
120	Skewness for pressure sensors 8, 9, 10 and 11 versus angle of attack. F6 S12 with leading-edge horn at $Re_c = 2.4$ million, with pressure sensors 6 (for sensors 8 and 9) and 14 (for sensors 10 and 11) as references for facility noise removal.	115
121	Flatness for pressure sensors 8, 9, 10 and 11 versus angle of attack. F6 S12 with leading-edge horn at $Re_c = 2.4$ million, with pressure sensors 6 (for sensors 8 and 9) and 14 (for sensors 10 and 11) as references for facility noise removal.	116
122	Auto spectral densities of acceleration components versus model angle of attack. F6 wing with leading-edge horn at $Re_c = 2.4$ million.	117

- 123 RMS of acceleration components versus model angle of attack. F6 wing with leading-edge horn at $Re_c = 2.4$ million. 118

1 Introduction

Geometric junctures (intersections of two structural parts) are common features on most aerodynamic and hydrodynamic vehicles. Wing-body juncture flow is of particular interest to aircraft design engineers, because flow behavior such as flow separations in these juncture areas can have an adverse impact on aircraft performance.

One of the biggest challenges in computing aerodynamic flow fields using computational fluid dynamics (CFD) is the accurate prediction of turbulent separated flows. For example, on a flow geometry where separation is known to occur empirically, different turbulence models can predict a range of outcomes from fully-attached flow to massively-separated flow. Even in cases where a given turbulence model predicts a separated flow field geometry that agrees well with empirical observation, there is some concern that the agreement is merely fortuitous and that the model is not capturing the underlying physics correctly. To understand why a particular turbulence model fails or succeeds in a particular separated flow situation, more detailed analysis of the calculated results is required. To assist in that analysis, careful and detailed flow-field measurements need to be made, including experimental determination of higher-order turbulence quantities. The NASA juncture flow experiment is designed to achieve this goal as well as to enlighten and inform the understanding of juncture-flow physics [1]. Juncture flows have been studied in detail for many decades and Simpson [2] has written a very thorough review of the field.

The flows of interest in this experiment are located in the areas of the wing root leading edge at the wing/fuselage juncture, and the trailing-edge juncture region on the wing upper surface. At the wing leading edge, the approaching fuselage boundary layer flow encounters a pressure gradient due to the presence of the wing, which initiates unsteady flow separation. In the average sense, within this separated flow, a vortical flow forms with rotation in the sense of the approaching boundary layer vorticity. This flow splits around the wing root and flows to either side, forming the horseshoe vortex that trails downstream. Often, a small, counter-rotating vortex is formed between the horseshoe vortex and the wing root leading edge, again in the average flow sense.

The actual, instantaneous nature of the flow has been found to be much different. As described by Devenport and Simpson [3], a region exhibiting a bimodal velocity probability distribution exists upstream of the wing root. In this region, an aperiodic switching is thought to occur between one flow mode and another. These two flow states were designated “backflow” mode and “zero-flow” mode [4], relating to the peaks in the velocity histograms where the peak was either at a large negative velocity or near zero. This unsteady nature of the flow has been identified by Simpson [2] as being a region where there is not one horseshoe vortex, but a number of them that overtake and merge with each other in a very dynamic way upstream of a line of low shear—a location at which the local surface shear stress drops off, but does not vanish. Between the line of low shear and the wing leading edge is a region of high surface shear stress that is manifested by a strong “scrubbing” of surface oil flow visualization materials, presumably by the action of the horseshoe vortex system.

At the wing trailing edge, on the upper surface at the wing/fuselage juncture, there can exist a corner separation that varies in size with angle of attack. As was mentioned in a review by Gand [5], early studies concentrated on more fundamental configurations, like corner flows, in which the source of the separation was related to the gradients of Reynolds stresses. However, as Gand points out, Barber [6] described a flow scenario involving the interplay between the horseshoe vortex and the corner separation on a wing/flat plate junction. In this case, it was found that the extent of separation in the corner was dependent on the thickness of the incoming boundary layer for a given angle of attack. For an incoming boundary layer that was thicker, the horseshoe vortex dominated the flow and suppressed the separated flow region. This happened by the entrainment over the vortex of high-momentum

fluid into the corner region and suppressing separation by sustaining high adverse pressure gradients before separating. For thinner incoming boundary layers, the viscous wake in the corner dominated the flow and was larger. This was due to the smaller-scale vortex produced by the thinner incoming boundary layer that could not prevent low-momentum fluid from coming into the corner region, and thus separating more easily. In spite of these proposed flow scenarios, Gandy [7] does state that the precise connection between the corner separation size and incoming boundary layer thickness is still in question and needs more research. A future experiment with a highly-instrumented model at NASA Langley will be conducted, in part, to help answer this question. The current experiment reported herein was conducted to help facilitate the design of such future, in-depth experiments.

The purpose of this experiment was to examine the surface and off-body flow on a generic wing/body combination to: 1) choose a final wing for a future, highly-instrumented model, 2) use the results to facilitate unsteady pressure sensor placement on the model, 3) determine the area to be surveyed with an embedded LDV system, 4) investigate the primary juncture corner flow separation region using particle image velocimetry (PIV) to see if the particle seeding is adequately entrained and to examine the structure in the separated region, and 5) to determine the similarity of observed flow features with those predicted by computational fluid dynamics (CFD).

The current report documents the results of the above experiment that specifically address the first three goals. The preliminary PIV measurements that were performed during the test are not documented here and we do not make comparative observations between the experimental results and CFD. Nevertheless, the results presented in this report provide a basis for achieving the ultimate goal of generating a carefully-acquired set of experimental data for use in better understanding the physics of juncture flows and in better validating CFD turbulence models.

2 Experimental Methods

2.1 14- by 22-Foot Subsonic Wind Tunnel

The experiment was performed in the Langley 14- by 22-Foot Subsonic Tunnel, which is a closed-circuit, atmospheric-pressure wind tunnel capable of operating in an open, partially closed, or closed test-section mode. Raising and lowering of the north and south walls and ceiling creates the various modes of tunnel geometry. The floor of the test section is formed by two model carts that are moved to and from the test section front and back bays. The carts are raised and lowered on hydraulic lifts and transported along the floor under the test section on air pads. Once in place, the tunnel floor is fixed during testing. Measurements for this test were made in the closed test section mode. In this mode, the test section measures 4.42 m (14.5 ft) high and 6.63 m (21.75 ft) wide, and the maximum free-stream velocity is 103 m/s (338 ft/s). The tunnel contraction ratio is 9 to 1. Further details about the tunnel can be found in Gentry *et al.* [8]. The flow condition of primary interest for this experiment was $Re_c = 2.4$ million. The model angle of attack, α , was varied from -10° to 10° .

2.2 Juncture-Flow Model

The juncture-flow model was a large aluminum model consisting of a fuselage (≈ 3.66 m long) and a number of interchangeable wing candidates (wing span of ≈ 2.44 m). The model was painted with a black lusterless polyurethane paint that was suitable for both infrared thermography and oil-flow visualizations on the model surface. The model was attached to a long sting that could be raised or lowered via a motorized sting mast to keep a reference point on the model near the center of the test section during an angle-of-attack adjustment.

Six different wing candidates were considered in the test: an F6 wing, an F6 wing with a leading-edge horn, a symmetric wing with an NACA 0015 root profile, a symmetric wing with a modified NACA 0015 root profile, a symmetric F6 variant (F6 S12 wing), and a symmetric wing designed with CDISC [9] using skin-friction constraints (COCA wing). The NACA 0015, the NACA 0015 mod, the F6 S12, and the COCA wings were all designed with a leading-edge horn. Further details on the wing designs are reported in Rumsey *et al.* [1]. Over the course of the test, the model was configured with the different wing pairs listed in Table 1. Photographs of the juncture-flow model with wing-configuration 1, as installed in the 14- by 22-Foot Subsonic Wind Tunnel test section, are shown in Figs. 1 and 2. The wing root section profiles for the six wing candidates are shown in Fig. 3.

To ensure a turbulent boundary layer on the fuselage and the upper surfaces of the wing candidates, trip-dot arrays were used to fix the transition location. The trip dots, which were spaced 2.54 mm apart and had a diameter of 1.27 mm, were applied to the model with a commercially-produced trip-dot tape that was available in a range of heights. Example pictures of the trip-dot placement on the juncture-flow model are shown in Figs. 4a and 4b. The lower surfaces of the wing candidates were not tripped in this test. Specific details on the trip-dot placement and height selection for the fuselage and each of the wing candidates will be presented in the Results section below.

2.3 Infrared Imaging

Infrared (IR) imaging was used to determine the location of boundary-layer transition on the juncture-flow model. This method is based on the detection of surface temperature differences brought about by the increased heat-transfer rates that occur as the boundary layer transitions from laminar to turbulent flow. Although these surface temperature changes are small in low-speed flows, the current generation of IR cameras can resolve temperature differences on the order of milliKelvins, which is sufficient to reveal the transition location for our test conditions. For the present experiment, two IR cameras with cooled Indium Antimonide (InSb) detectors were used. These cameras provide temperature measurements in the mid-wavelength infrared (MWIR) range of 3 to 5 μm and were calibrated for a temperature range from -20° C to 500° C with an accuracy of $\pm 2^\circ \text{ C}$ or 2% of reading. One of the cameras was fitted with a 25 mm, $f/4.0$ lens for a wide field of view and the other camera was fitted with a 50 mm, $f/4.0$ lens for a more standard field of view. Both cameras were connected to a host PC via a GigE Vision interface for camera control and image acquisition.

2.4 Oil-Flow Visualization

To help guide the selection of the final wing configuration for the forthcoming, fully-instrumented juncture-flow model, an oil-flow visualization study was performed. The oil-flow visualizations were used to observe whether corner-flow separation occurred for a given wing candidate and if so, to observe the progression of the corner-flow separation with model angle of attack. The oil-flow visualizations were also used to observe the surface topology in the leading-edge region of the wing-fuselage juncture and over the wing planform.

For the present study, the oil-flow material was a mixture of 1 part titanium dioxide (TiO_2), 2 parts kerosene, and 0.3 parts oleic acid. The TiO_2 , which serves as a pigment for the mixture, was white and contrasted well against the black painted model surface. The kerosene, which serves as carrier liquid for the pigment, facilitated the flow visualization by moving under the influence of the local surface shear stress and then evaporated to leave a mean-flow pattern of pigment on the surface. The oleic acid, which serves as a dispersant, kept the TiO_2 from clumping. In addition, by increasing the proportion of oleic acid, the viscosity of the mixture could be increased, if needed. Prior to a given run, the

oil-flow material was applied to the model surface with foam paint brushes. The tunnel was then ramped up to the desired chord Reynolds number and a live video feed was used to determine when the oil-flow material stopped flowing. After the run, post-test imagery of the oil-flow visualization was acquired. An overhead planform view of the flow visualization was acquired with a 36 megapixel digital SLR. Close-up images of the corner-flow separation, the wing leading-edge region, and any other flow features of interest from a given run were acquired with 12 megapixel digital SLRs. A video recording of the oil-flow development during a run was also recorded. An example oil-flow visualization is shown in Fig. 5 and here, the corner-flow separation in the trailing-edge region of the F6 wing with leading-edge horn is clearly revealed.

Although the oil-flow visualizations are generally regarded as qualitative in nature, they were used in the present study to obtain measurements of the width and length of the corner-flow separation versus model angle of attack. These measurements were useful for defining the area to be surveyed with an embedded laser doppler velocimetry (LDV) system that will be a key component in the forthcoming, fully-instrumented juncture-flow model. They were also useful for selecting the positions of the unsteady pressure sensors that will be installed in that model. Generally, the corner-flow separations are marked by a diffuse band of oil-flow material at the boundary of the separation. This is due to the unsteady nature of the corner-flow separation and the “history” of the oil-flow development as a run proceeds. As such, it is difficult to say precisely where the mean separation line is located. For this present study, we report the outer extent (length and width) of this band of oil-flow material, and an example width, w , and length, ℓ , measurement is annotated in Fig. 5. With this definition, it is likely that the true length and width bounding the mean separation line is less than what is reported here. Nevertheless, it was felt that the measurements were of sufficient accuracy to aid in the future model design. A ruler with 1 mm divisions was used to measure the length and width of the corner-flow separation.

2.5 Unsteady Measurements

Unsteady pressure measurements were performed to gain insight into the dynamic nature of the flow in specific regions near the wing-root section. Additionally, these measurements were used to inform the selection and layout of pressure transducers for the forthcoming, fully-instrumented juncture-flow model. Fourteen miniature piezoresistive pressure transducers were embedded in the port side of the fuselage at the locations listed in Table 2. The transducer locations are also plotted in Fig. 3 to illustrate their positioning relative to the wing root section profiles. The differential pressure transducers had a full scale range of 34.5 kPa (5 psid) and a nominal static sensitivity of 8.7 mV/kPa (60 mV/psid). Each of the sensors were referenced to the ambient pressure in the control room of the wind-tunnel facility. The frequency responses of the transducers, as per the manufacturer, were flat from DC to roughly 20 kHz. The acceleration sensitivity of the transducers was 0.0014 kPa/g equivalent; which for the acceleration levels measured during the test, produces equivalent pressures that are below the noise floor of the measurement system.

To improve the spatial resolution of the pressure measurements, each of the transducers were mounted behind a small pin hole with a diameter of 0.5 mm. Using the analysis of Panton and Miller [10], the specific geometry of the pin hole was designed to produce a Helmholtz frequency of roughly 20 kHz. However, the actual Helmholtz frequency was found to be lower (11 to 12 kHz). This is due to the fact that we did not account for the finite model paint thickness, which increased the length of the pin-hole orifice and therefore, decreased the Helmholtz frequency.

To quantify the vibration levels on the model during a wind-tunnel run, the juncture-flow model was instrumented with accelerometers to measure the three orthogonal components of acceleration. These accelerometers had a nominal sensitivity of 5 g/V and were mounted

inside the model to a fixture on the wing box.

The voltage signals from the pressure transducers and accelerometers were AC coupled at 0.25 Hz, pre-amplified, and then passed through an 8th-order low pass filter with a cutoff frequency of 20 kHz for anti-aliasing. The signals were then digitized with a 24-bit A-to-D converter at a sample rate of 50 kHz. Each channel was sampled simultaneously for a duration of 40 seconds, yielding a total of 2 million samples per channel.

3 Data Analysis Methods

The voltage time series from the pressure transducers and accelerometers were first converted to engineering units. Since both types of sensors have a linear response, this amounted to multiplying the time series by the respective sensitivities of the sensors. For the pressure transducers, the static sensitivities were determined via an *in situ* calibration with a pressure standard that was applied to the reference ports of the transducers. For the accelerometers, the manufacturers reported calibrations were used.

The pressure and accelerometer times series were then processed via the Welch method to obtain estimates of the auto-spectral densities. There, a blocksize of 10,000 samples was used and a Hanning window with 50% overlap was applied. A total of 400 block averages were performed and the frequency resolution of the auto-spectral densities was 5 Hz.

Initial estimates of the pressure auto-spectral densities revealed that the unsteady pressures were contaminated by facility-induced noise. As an example, auto-spectral densities for pressure sensor 1 versus model angle of attack, acquired with the F6 wing, are shown in Fig. 6. Generally, the facility-induced noise lies below 1 kHz, and includes a tonal component corresponding to the blade passage frequency (≈ 35 Hz) of the wind tunnel drive fan and a region of tonal and broadband noise in the range of several hundred hertz. The spectral peak around 11-12 kHz corresponds to the Helmholtz resonance of the transducer pin hole and is not due to facility noise. The facility noise signature was observed in all of the fuselage pressure transducers and does not appear to be related to the pressure field induced by the local turbulent flow structures in the model boundary layer.

Facility-induced noise contamination is a common problem in the measurement of surface pressure fluctuations beneath a turbulent flow. This is particularly true in low-speed flows, where the facility noise signature can overwhelm the low-level turbulent fluctuations. Previous studies have considered noise-cancellation schemes to remove the facility noise from the pressure signals. One approach is to use subtraction-based methods, where the signals from two pressure transducers are subtracted and subsequently processed to yield noise-free estimates of 2nd-order statistics (e.g., RMS and spectra). Several variants of this approach, each with a different set of assumptions, have been reported in the literature [11–13]. While subtraction-based methods can be successful, their main drawback is that they are limited to corrections of the 2nd-order statistics. Another approach is to use optimal-filtering methods for noise cancellation [14]. Two sensors are still used in this approach, but the only requirement is that they are spaced far enough apart so that the local turbulent pressure fluctuations sensed by each one are uncorrelated. The main advantage of optimal-filtering methods is that the facility noise is removed in the time domain, and the resulting noise-free time series can be subsequently processed to obtain statistics, probability densities, and spectral estimates.

In the present study, an adaptive noise-cancellation method was used to remove the facility-induced noise from the unsteady pressures. This method is applicable to both non-stationary and stationary time series, and in the latter case, the adaptive noise canceler converges to the optimal filter of Naguib *et al.* [14]. A block diagram of the adaptive noise cancellation scheme is shown in Fig. 7. Here, the primary input is a pressure sensor signal from which we want to remove the facility-induced noise. This signal is comprised of the

local turbulent pressure fluctuations, p_{1t} , and the facility noise, p_{1a} . The reference input is provided by a second pressure sensor that also senses local turbulent pressure fluctuations, p_{2t} , and facility noise, p_{2a} . Note that the facility noise signals sensed by both the primary and reference transducers are from the same source, but they can be different—due, for example, to transport delays—and that difference is reflected by the transfer function $H(z)$. Furthermore, knowledge of that transfer function is not required by the adaptive noise canceler. The only requirement for the adaptive noise canceler is that the primary and reference inputs are far enough apart so that the turbulent pressure fluctuations sensed by each one are uncorrelated. In the processing of the current data set, the primary and reference inputs were spaced more than one boundary-layer thickness, δ , apart.

With the primary and reference pressure sensors defined, the adaptive noise canceler was implemented as follows. The reference input, denoted here as x_k , was input to a single-input transversal filter:

$$y_k = \mathbf{X}_k^T \mathbf{W}_k = \mathbf{W}_k^T \mathbf{X}_k \quad (1)$$

where the filter weight vector was defined as:

$$\mathbf{W}_k = [w_{0k} \ w_{1k} \ \cdots \ w_{Lk}]^T \quad (2)$$

and the filter input vector was defined as:

$$\mathbf{X}_k = [x_k \ x_{k-1} \ \cdots \ x_{k-L}]^T \quad (3)$$

Here, y_k is the filter output at the current time step or sample k , and L is the length of the transversal filter. Equation 1 indicates that the filter output at the current time step is the weighted sum of the current and past L input values. The filter output is then subtracted from the primary input, denoted here as d_k , to form an error signal at time step k :

$$\varepsilon_k = d_k - y_k = d_k - \mathbf{X}_k^T \mathbf{W}_k \quad (4)$$

The objective of the adaptive noise canceler is to produce a system output that is a best fit in the least-squares sense to the desired turbulent pressure signal, $p_{1t}(k)$. This is accomplished by adjusting the coefficients of the filter $W(z)$ through an adaptive algorithm so that the mean squared error, $E[\varepsilon_k^2]$, is minimized. When that is achieved, the filter effectively produces a prediction of the facility noise, $p_{1a}(k)$, at the filter output and that is subsequently subtracted from the primary input to produce a pressure signal, $p_{1t}(k) \approx \varepsilon_k$, that is free of the facility noise. In the present study, a gradient-descent algorithm was used to iteratively update the filter coefficients, \mathbf{W}_k , to find the minimum mean-squared error. More specifically, we used the least-mean-square (LMS) algorithm to update the filter coefficients at each time step according to [15]:

$$\mathbf{W}_{k+1} = \mathbf{W}_k + 2\mu\varepsilon_k \mathbf{X}_k \quad (5)$$

where μ is a gain constant that regulates the speed and stability of the adaptation. Further details on the LMS algorithm and guidelines for selecting the gain constant to achieve good performance are provided in Widrow and Stearns [15]. For the present study, a filter length of $L = 1400$ and a gain constant of $\mu = 0.005 \text{ kPa}^{-2}$ were found to be effective for removal of the facility-induced noise.

As an example of the adaptive noise cancellation method, consider the pressure time series used to generate the auto-spectral densities in Fig. 6. The time series for pressure sensor 1 (primary input) and pressure sensor 2 (reference input) were run through the adaptive algorithm and auto-spectral densities for the resulting noise-free time series of pressure sensor 1 were estimated. The results are shown in Fig. 50 and here, we observe an auto-spectral density that is more broadband in character and indicative of the pressure spectrum associated with an attached turbulent boundary layer [16].

All of the unsteady pressure results presented in the Results section were processed through the adaptive noise cancellation algorithm. Then, auto-spectral density estimates were made as discussed earlier. For statistical estimates, such as RMS, skewness, flatness, and probability distributions, the noise-cancelled time series were first digitally low-pass filtered at 5 kHz to remove the influence of the Helmholtz resonance on the signal statistics.

4 Results

In this section, the results of the flow-visualizations for the four wing configurations are presented and discussed. The results of the unsteady pressure measurements for the four different wings considered are then presented, followed by a presentation of the accelerometer measurements.

4.1 Flow Visualization Results

4.1.1 Configuration 1: F6 Wing and F6 Wing with Leading-Edge Horn

For this configuration, the juncture-flow model was configured with the F6 wing on the port side of the fuselage and the F6 wing with leading-edge horn on the starboard side of the fuselage. Our first task with this model configuration was to determine the location of natural transition on the fuselage, and if necessary, to fix the transition location with boundary-layer trip dots so that a turbulent boundary layer was ensured over most of the model fuselage. To that end, one IR camera with a 25 mm lens was placed behind an open hole in a tunnel sidewall panel to provide a view of the port side of the fuselage. Infrared images of the clean fuselage (no boundary layer trip dots) versus model angle of attack and $Re_c = 2.4$ million are shown in Fig. 8. In the images, dark tones correspond to lower (cooler) temperatures and lighter tones correspond to higher (warmer) temperatures. Since the model was cooler than the air temperature, the initially laminar boundary layer on the fuselage nose is marked by dark tones. Boundary-layer transition on the fuselage is then marked by the sudden shift toward lighter tones, where the increased heat transfer associated with the turbulent flow increases the fuselage temperature. It can be seen that the natural transition pattern is somewhat irregular and that the transition location changes slightly with angle of attack. There is also a wedge of turbulent flow ahead of the natural transition location which was found to emanate from a small protuberance of paint near the bottom of the fuselage nose.

To ensure a consistent transition location for the fuselage boundary layer, trip dots were placed on the model at a fixed surface distance of 304.8 mm (12 in.) from the fuselage nose. This location was chosen so that: 1) the trip dots were nominally positioned just downstream of the suction peak as determined from computed pressure distributions at our test conditions and 2) the local Reynolds number, Re_s , was greater than 100,000 to ensure fully effective trip dots [17]. The height of the trip dots was based on the roughness correlations of Braslow and Knox [18], and for our test conditions, the trip dots had a height of 218.4 μm (0.0086 in.). Infrared images for the tripped fuselage versus model angle of attack and $Re_c = 2.4$ million are shown in Fig. 9. Here, it is observed that the transition location is fixed at the trip dots and does not vary with angle of attack. In this set of images, the turbulent wedge associated with the protuberance near the nose is still observed. For subsequent runs, this protuberance was removed from the model.

Our next task with this model configuration was to determine the location of natural transition on the wings and then to fix the transition location with trip dots. Infrared images of the clean F6 wing with leading-edge horn (starboard side) are shown in Fig. 10. For this set of images, the IR camera was fitted with a 50 mm lens and positioned above the model behind an opening in the test-section ceiling. Although the field of view is limited

to the inboard region of the wing, we were still able to obtain a sense of the boundary-layer state on the wing. The first thing to note from these images is the lighter tones on the wing leading-edge horn. This indicates that turbulent flow from the fuselage boundary layer contaminates the wing leading edge. However, as we move outboard along the leading edge, the darker tones indicate that the flow has relaminarized, and this is due to the fact that the attachment line Reynolds number has decreased to a value that is too low to sustain turbulent flow. At $\alpha = -2.5^\circ$, we first observe the transition location on the wing planform, and that approaches the wing leading edge as α is increased to 0° . Then, at $\alpha = 2.5^\circ$, rather than continuing to gradually move toward the leading edge, the transition location snaps forward to very near the leading edge and stays there throughout the rest of the angle-of-attack sweep. This behavior suggests that a leading-edge separation bubble forms and reattaches turbulent, very near the leading edge.

To eliminate the leading-edge separation bubble, trip dots with a height of $142.2 \mu\text{m}$ (0.0056 in.) were placed just upstream of the separation bubble at 1.6% of chord. The resulting IR images versus model angle of attack are shown in Fig. 11. For the two lowest model angles, -10° and -7.5° , the boundary layer was still laminar near the wing leading edge. This is likely due to the fact that the trip dots are in a region of accelerated flow and therefore, due to the stabilizing effect of the favorable pressure gradient, are not fully effective. Once the model is moved to $\alpha = -5^\circ$, it appears that, except for a few small streaks, transition was fixed at the trip dots and stays that way throughout the rest of the angle-of-attack range.

Infrared images of the tripped F6 wing (port side) are shown in Fig. 12. To provide a full view of the port-wing planform, the camera was fitted with a 25 mm lens and positioned above the model behind an opening in the test-section ceiling. Infrared images of the clean F6 wing were not acquired. Nevertheless, it was assumed that a leading-edge separation bubble existed on this wing as well and therefore, the trip dots (with a height of $142.2 \mu\text{m}$) were placed at 1.6% of chord to eliminate the bubble. In contrast to the starboard wing (with the horn), turbulent flow from the fuselage boundary layer does not appear to contaminate the port wing leading edge. This is because the attachment-line Reynolds number, even at the wing root, is too low to sustain turbulent flow on the wing leading edge. Similar to the starboard wing, the trip dots were not fully effective for the two lowest model angles and there, a considerable region of laminar flow is observed on the wing planform. For model angles of $\alpha = -5^\circ$ and greater, the transition location was fixed at the trip dots.

With the fuselage and wing boundary layers tripped, we next performed oil-flow visualizations to observe the occurrence and progression of separation in the trailing-edge corner of the wing-fuselage juncture. Planform views of the oil-flow visualizations for configuration 1 versus model angle of attack and $Re_c = 2.4$ million are shown in Fig. 13. As the model angle of attack is increased from -5° to 10° , the trailing-edge corner-flow separation is observed to grow in size. Although the size of the corner-flow separation on the port wing appears to be larger than that on the starboard wing in these images, measurements of the corner-flow separation size indicate that they are comparable. This apparent discrepancy is due to a slight displacement of the camera to the port side of the model, which distorts the image. Other notable features in the planform views include a region of trailing-edge separation just outboard of the corner flow on the starboard wing for $\alpha \geq 5^\circ$. This appears to be induced by a flow structure emanating from the leading-edge horn of the starboard wing. In contrast, this feature is absent from the port wing, which does not have a leading-edge horn. There is also noticeable trailing-edge separation outboard of the trailing-edge wing break on both wings at $\alpha = 10^\circ$.

Close-up views of the corner-flow separation for the port and starboard wings of configuration 1 are shown in Figs. 14 and 15. Both figures show the growth of the corner-flow separation as the model angle of attack is varied from $\alpha = -10^\circ$ to 10° . In neither case is the corner flow fully attached for any of the model angles considered. As with the planform

views of the oil-flow (Fig. 13), a region of separated flow at the trailing edge, outboard of the corner flow, is observed on the starboard wing and it grows in size with increasing model angle. In contrast to the planform views, the close-up views allow us to see that the trailing-edge separation actually begins earlier at $\alpha = 2.5^\circ$. This flow feature is absent on the port wing.

Measurements of the corner-flow separation width, w , and length, ℓ , of configuration 1 were made using the approach described in Section 2.4. To reiterate earlier comments, these measurements are suitable for defining survey regions for detailed measurements on the forthcoming fully-instrumented juncture-flow model and for identifying trends; but they are not suitable for exact comparison with other analyses, such as CFD calculations. In addition to the limitations of oil-flow visualization discussed earlier, the detailed analysis by Squire [19] and comments from other experts in flow-visualization techniques [20–23] suggest that quantitative comparisons with surface-flow visualizations are not generally warranted. The measured corner-flow separation width and length versus model angle of attack are shown in Figs. 16 and 17. The error bars on each data point in the plots represent the 95% confidence interval, and the uncertainty analysis from which they were derived is provided in Appendix A. The width and lengths, along with the uncertainties, for both wings are also provided in Tables 3 and 4. From Fig. 16, the width of the corner-flow separation increases with model angle for angles higher than $\alpha = -7.5^\circ$. The difference between the widths for the F6 wing and the F6 wing with leading-edge horn is generally within the measurement uncertainty. From Fig. 17, the length of the corner-flow separation is essentially unchanged up to $\alpha = -5^\circ$ and then increases with increasing model angle. As before, the difference between the lengths for the two wings is generally within the measurement uncertainty.

In addition to the oil-flow visualizations on the wing planform, oil-flow visualizations on the fuselage were performed. Oil-flow visualizations in the wing leading-edge juncture region for the F6 wing (port side) versus model angle of attack are shown in Fig. 18. Here, there is clear evidence of scrubbing by the mean action of the horseshoe vortex system near the leading edge at several of the model angles. Depending on the mobility of the flow-visualization material, this scrubbing may or may not have appeared as clearly in a given run. More specifically, a lack of detail in a given image does not necessarily imply an absence of flow structure, but instead is a limitation of the oil-flow technique. A closer view of the leading-edge juncture region is shown in Fig. 19 for $\alpha = 5^\circ$. The surface flow feature farthest to the left side indicates a separation line, where flow moves into a stagnation point that is a topological saddle point. The flow moves around and away from this stagnation point to either side and also comes to the stagnation point from downstream. The next distinct line is called a line of low shear, as defined by Devenport and Simpson [4]. This is not a separation line, but is a line where the shear stress at the surface is minimized and oil-flow pigment accumulates there upstream of the horseshoe vortex scrubbing area. As mentioned above, Simpson [2] has pointed out that there are a number of vortices that overtake and merge with each other to form a system of vortices. Evidence for a strong horseshoe vortex system can be seen in Fig. 20, where an area between the wing leading edge and the line of low shear displays a loss of oil-flow pigment due to the scrubbing action of this vortical flow. This is an area of high surface shear stress, and just upstream of that area, oil-flow pigment accumulates. The distance between the wing leading edge and the line of low shear is approximately $0.1T$, where T is the maximum thickness of the wing root section. In contrast, Devenport and Simpson [4] reported a distance of $0.28T$. This difference is likely due to differences in the experimental configuration, which for our case include a wing that is less blunt, non-symmetric, swept, tapered, and at an angle of incidence.

Oil-flow visualizations in the wing leading-edge juncture region for the F6 wing with leading-edge horn (starboard side) versus model angle of attack are shown in Fig. 21. For this wing, there appears to be a separation line that lies very close to the leading edge of the horn. However, the distinct scrubbing by the action of a horse vortex system, as seen on the

port wing, is not clearly evident in these images. A few of the images (Figs. 21g and 21i) have a secondary streak of oil-flow pigment that may indicate the trace of a horseshoe vortex, and if that is the case, then the horseshoe vortex may be forming on the leading-edge of the horn itself. Although the actual strength of the vortex system cannot be determined from the flow visualizations, the lack of distinct surface scrubbing suggests that any horseshoe vortex system that may be present is relatively weak.

Additional close-up views of the trailing-edge separation on the F6 wing with leading-edge horn are shown in Fig. 22. Following the surface streak pattern from this separation forward to the leading edge leads directly to the horn area, implicating the horn as the generator of a structure that induces this separation. It was also noted that the trailing-edge separation region grows in size and moves farther outboard along the wing trailing edge as the model angle of attack was increased.

Oil-flow visualization on a planform section of the F6 wing with leading-edge horn at $\alpha = -7.5^\circ$ is shown in Fig. 23. Here we observe prominent streaky structures in the oil-flow pattern that are the footprint of the vortical structures generated by the trip dots. As was indicated in the IR images for this model angle (see Fig. 11b), the trip dots were not fully effective due to their placement in a favorable pressure gradient. Therefore, we observe a long run of these vortical structures before they break down to turbulence. For larger model angles, where the trip dots were fully effective, we do not observe these streaky structures in the oil-flow pattern.

The effect of Reynolds number on the surface topology of wing configuration 1 at $\alpha = 5^\circ$ is shown in Fig. 24. Oil-flow visualization for a smaller-scale model (2.4 times smaller than the present model) tested in the Virginia Tech Stability Wind Tunnel at $Re_c = 0.62$ million is shown in Fig. 24a [24] and oil-flow visualization for the present model at $Re_c = 2.4$ million is shown in Fig. 24b. Clearly, there is significant trailing-edge separation along the wing span for the lower Reynolds number case while there is none for the higher Reynolds number case. In addition, if the corner separation width on the smaller model is directly scaled to the present model size, the scaled width is larger than the actual width. More specifically, the corner-separation widths as measured on the present model were, on average, 85% of the scaled widths from the smaller model. This implies that increasing Reynolds number has an attenuating effect on the corner separation, and therefore geometric scaling is not appropriate when the chord Reynolds number is not maintained.

4.1.2 Configuration 2: NACA 0015 Wing and NACA 0015mod Wing

For this configuration, the juncture-flow model was configured with the NACA 0015 wing on the port side of the fuselage and the NACA 0015mod wing on the starboard side of the fuselage. Both wings were designed with a leading-edge horn. As before, we first evaluated the natural transition location on the wings via IR imagery and then fixed transition with boundary layer trip dots. Infrared images of the clean NACA 0015mod wing (starboard side) are shown in Fig. 25. The lighter tones on the wing horn indicate that turbulent flow from the fuselage contaminates the leading edge and the darker tones that exist outboard on the leading edge suggest that the boundary layer relaminarizes due to the low attachment line Reynolds number. On the wing planform, the transition location is observed to smoothly progress forward with increasing model angle of attack. This is in contrast to the F6 wings of configuration 1, where the transition front snapped forward due to the formation of a leading-edge separation bubble that reattached turbulent. Using the same approach as for the fuselage trip-dot placement and height selection, trip dots with a height of $142.2 \mu\text{m}$ (0.0056 in.) were placed on the NACA 0015mod wing at 6.4% of chord. With the trip dots, the IR images of Fig. 26 show that the transition location is fixed at the trip dots for model angles ranging from 0° to 10° . Note that negative model angles were not considered due to the symmetric shape of the airfoil.

Infrared images of the clean NACA 0015 wing (port side) are shown in Fig. 27. Similar to the NACA 0015mod wing, there is leading-edge contamination on the wing horn and the transition location on the wing planform smoothly progresses forward with increasing model angle of attack. Although the port wing was “clean” when these IR images were acquired, there were evidently a few protuberances near the wing leading edge that produced the turbulent wedges that appear ahead of the nominal natural transition location (see Figs. 27a and 27b). With trip dots of the same height and location as for the NACA 0015mod wing, the IR images in Fig. 28 show that the transition location is fixed at the trip dots for all of the model angles considered.

Planform views of the oil-flow visualizations for configuration 2 versus model angle of attack and $Re_c = 2.4$ million are shown in Fig. 29. For the NACA 0015 wing on the port side of the fuselage, no corner flow separation is observed except at $\alpha = 10^\circ$, where a very small region of separated flow appears in the trailing-edge corner. For the NACA 0015mod wing on the starboard side of the fuselage, there is corner-flow separation for all model angles of attack, although it appears to be smaller than the corner-flow separations on the F6 wings of configuration 1. A region of separated flow at the trailing edge, outboard of the corner-flow region, is observed at $\alpha = 10^\circ$ on the NACA 0015mod wing while none is observed for the NACA 0015 wing. This may be due to the fact that the trailing-edge closure angle for the NACA 0015mod wing is greater than that of the NACA 0015 wing and therefore, the NACA 0015mod wing may be more susceptible to trailing-edge separation. In that case, any flow structures emanating from the leading-edge horn may better facilitate trailing-edge separation, since the flow is closer to “letting go.”

Close-up views of the trailing-edge corner-flow region for the NACA 0015 wing are shown in Fig. 30. For this case, no corner-flow separation was clearly observed until a model angle of $\alpha = 7.5^\circ$ and after that, the size of the corner-flow separation grows with increasing model angle of attack. There is no apparent trailing-edge separation outboard of the corner-flow region in this case. Close-up views of the trailing-edge corner-flow region for the NACA 0015mod wing are shown in Fig. 31. For this case, corner-flow separation is observed for all model angles and the separated region grows with increasing model angle of attack. The region of trailing-edge separation outboard of the corner-flow region can also be observed to grow with increasing model angle of attack.

The measured corner-flow separation widths and lengths for configuration 2 versus model angle of attack are shown in Figs. 32 and 33. The values of the widths and lengths, along with the associated uncertainties, are also provided in Tables 5 and 6. The measured widths and lengths for the F6 wings of configuration 1 are included in the plots for comparison. For the NACA 0015 wing, no corner-flow separation was observed for model angles below $\alpha = 5^\circ$. Three oil-flow visualizations were performed at $\alpha = 5^\circ$ and two of them indicated no corner-flow separation, while the other one indicated a very small corner-flow separation. That variability is reflected by the two data points at $\alpha = 5^\circ$ for the NACA 0015 wing. At larger model angles, the width and length increase with increasing model angle. For the NACA 0015mod wing, the corner flow is separated for all angles and both the width and length increase with increasing model angle. In general, the corner-flow separation widths and lengths for the wings of configuration 2 are smaller than those for the wings of configuration 1. As noted earlier, negative model angles of attack were not considered for configuration 2 due to the symmetric shape of the airfoils.

The effect of Reynolds number on the surface topology of wing configuration 2 at $\alpha = 10^\circ$ is shown in Fig. 34. As with the wings of configuration 1, there is considerable trailing-edge separation for the smaller-scale, lower-Reynolds-number case. In addition, when the size of the corner-flow separation on the smaller model is scaled to the present model scale, the scaled size is larger than the actual size measured on the present model. This again implies the attenuating effect that increasing Reynolds number has on the size of the corner-flow separation.

4.1.3 Configuration 3: F6 S12 Wing and COCA Wing

For this configuration, the juncture-flow model was configured with the F6 S12 wing on the port side of the fuselage and the COCA wing on the starboard side of the fuselage. Both wings were designed with a leading-edge horn and since these wings had symmetric wing sections, only positive angles of attack were considered. Infrared images of the clean COCA wing (starboard side) are shown in Fig. 35. As with the other wings that had a leading-edge horn, the lighter tones on the wing horn indicate that turbulent flow from the fuselage contaminates the leading edge and the darker tones that exist outboard of the leading edge suggest that the flow relaminarizes due to the low attachment line Reynolds number. On the wing planform, just outboard of the horn, the transition location is observed to smoothly progress forward with increasing model angle of attack. Further outboard, however, the transition location appears to snap forward between $\alpha = 2.5^\circ$ and 5° , suggesting that a leading-edge separation bubble has formed and reattaches turbulent. To eliminate the leading-edge separation bubble, trip dots with a height of $182.9 \mu\text{m}$ (0.0072 in.) were placed at 1.6% of chord. In that case, the IR images of Fig. 36 show that transition was fixed at the trip-dot location for all of the model angles of attack considered.

Infrared images of the clean F6 S12 wing (port side) are shown in Fig. 37. Similar to the COCA wing, there is leading-edge contamination of the wing horn and just outboard of the horn, the transition location smoothly progresses forward with increasing model angle of attack. Further outboard, the transition location again snaps forward between $\alpha = 2.5^\circ$ and 5° , suggesting that a leading-edge separation bubble has formed on this section of the wing as well. With trip dots of the same height and location as for the COCA wing, the IR images in Fig. 38 show that the transition location on the F6 S12 wing was fixed at the trip dots for all of the model angles considered.

Planform views of the oil-flow visualizations for configuration 3 versus model angle of attack are shown in Fig. 39. Corner-flow separations are observed on both wings for all of the model angles considered. For the COCA wing, there is a prominent region of trailing-edge separation just outboard of the corner-flow region. Close-up views of the trailing-edge corner-flow region for the F6 S12 wing are shown in Fig. 40. Here, the oil-flow patterns in the corner-flow region are a bit muddled, and it is suspected that flow sweeping down from the fuselage onto the steep spanwise slope of the wing at the wing root may inhibit the corner-flow separation to some extent. Also for this wing, there is no apparent trailing-edge separation outboard of the corner-flow region. Close-up views of the corner-flow region for the COCA wing are shown in Fig. 41. For this wing, there is an isolated cell of separated flow at $\alpha = 0^\circ$ that lies away from the fuselage and there appears to be a very small corner-flow separation. As the angle of attack is increased, the corner-flow separation grows and then merges with this isolated cell of separated flow. Similar to the F6 S12 wing, flow sweeping down from the fuselage onto the wing may inhibit the corner-flow separation to some degree. Also for this wing, trailing-edge separation outboard of the corner-flow region is observed to begin at $\alpha = 5^\circ$ and then grows in extent with increasing model angle. Given the complex surface topology of the corner-flow separations for the wings of configuration 3, no attempt was made to define a width and length for these separated flow regions.

4.1.4 Configuration 4: F6 Wings with Leading-Edge Horns

In this final configuration, both sides of the juncture-flow model were configured with an F6 wing with leading-edge horn. No infrared imagery was acquired for this configuration. Based on the IR imagery from the F6 wings of configuration 1, it was expected that leading-edge separation bubbles form on the wings of configuration 4. Therefore, to eliminate the leading-edge separation bubbles, trip dots with a height of $182.9 \mu\text{m}$ (0.0072 in.) were placed at 1.6% of chord.

Planform views of the oil-flow visualizations for configuration 4 versus model angle of attack and $Re_c = 2.4$ million are shown in Fig. 42. Here, the progressive growth in the corner-flow separation with increasing model angle of attack and the horn-induced trailing-edge separation at higher angles of attack are observed. In a qualitative sense, the flow topology on the port- and starboard-wing planforms is symmetric. Close-up views of the corner-flow separation on both wings at $\alpha = 5^\circ$ is shown in Fig. 43 and here again, we observe qualitative symmetry in the topology of the corner-flow separation. It should be noted that the oil-flow material was applied to the port and starboard wings by two different people, and given the variability in the individual application of the oil-flow material, the symmetry displayed is remarkable. In addition to the standard oil-flow formulation that we employed throughout most of the test, we also performed a few runs with a more viscous formulation (1 part TiO_2 , 1.6 parts kerosene, and 0.32 parts oleic acid). That formulation did not make any notable difference in the surface topology of the corner-flow separation and therefore, no results with that formulation are shown here.

The measured corner-flow separation widths and lengths for configuration 4 versus model angle of attack are shown in Figs. 44 and 45. The measured width and lengths for the port wing are also provided in Table 7 and those for the starboard wing were previously provided in Table 4. As seen in the figures, the widths and lengths of the corner-flow separation on both wings are the same to within the measurement uncertainty. This agreement underscores the fact that, despite any flow nonuniformity in the freestream and any port-starboard asymmetry in the model geometry that may exist, the corner-flow separation on the model is highly symmetric.

Oil-flow visualizations were also performed on configuration 4 at a slightly higher chord Reynolds number of $Re_c = 2.7$ million. There, the main objective was to observe the effect of Reynolds number on the size of the corner-flow separation and the resulting measured widths and lengths are shown in Figs. 46 and 47. For comparison, the measurements for the lower Reynolds number of 2.4 million are included. The measured widths and lengths at this higher Reynolds number are also provided in Tables 8 and 9. For this small increase in Reynolds number, there is no statistically significant change in the width of the corner-flow separation. Likewise for the length of the corner-flow separation, except for the negative angles of attack where the length of the corner-flow separation is a bit smaller at the higher Reynolds number.

4.2 Unsteady Pressure Results

4.2.1 F6 Wing

Unsteady pressure data for the F6 wing configuration was collected for model angles of attack ranging from -10° to 10° and $Re_c = 2.4$ million. Consider first the unsteady pressure measurements in the leading-edge region of the wing. The approximate locations of the pressure sensors in this region (sensors 1 through 4) relative to the leading-edge surface-flow topology at $\alpha = 5^\circ$ are annotated in Fig. 48. Sensors 1 and 2 are positioned in the approaching flow, ahead of the separation line. Sensor 4 lies on or close to the separation line and sensor 3 lies between the separation line and the line of low shear (refer to the earlier discussion in Section 4.1.1 and Fig. 19). Auto-spectral densities for sensors 1, 3, and 4 are shown in Figs. 50, 52, and 54. Here, sensor 2 was used as a reference sensor in the adaptive noise cancellation scheme for facility-induced noise removal. The corresponding probability densities for sensors 1, 3, and 4 are shown in Figs. 51, 53, and 55. As was previously noted in Section 3, the probability densities were based on the noise-canceled pressure time series after filtering through a low-pass filter with a 5 kHz cut-off frequency. This filtering operation was performed to avoid the influence of the pin-hole Helmholtz resonance on the statistics. However, the resulting bandwidth on which the pressure statistics are based is

too low—by at least an order of magnitude in some cases—to capture the majority of the energy associated with the turbulent pressure field for our test conditions. In addition, the finite size of the sensor pin-hole orifice most likely leads to spatial averaging of the turbulent pressure field, but no corrections for that are made in the results presented here.

The auto-spectral densities for sensor 1 have a broadband character that is indicative of an attached turbulent boundary layer and they are relatively invariant with model angle of attack. The small peak at approximately 2700 Hz is present in all of the sensor 1 spectra and in fact, it is present in the spectra of all the fuselage pressure sensors when the turbulent pressure fluctuations are relatively low. One possible source for this tonal component could be the coherent shedding that occurs at the blunt trailing edge of the wing. As reported by Brooks and Hodgson [25], this appears at a Strouhal number of $St = ft/U_\infty \approx 0.1$, which for our trailing-edge thickness of 3.6 mm and freestream velocity of 97 m/s, is exactly the Strouhal number of the peak we observe. The probability densities for sensor 1 are nearly Gaussian and are relatively invariant with model angle of attack.

For sensor 3, which lies between the separation line and the line of low shear stress, the spectral levels are much higher and vary with model angle of attack. This variation is probably related to the movement in the surface-flow topology with model angle, where the separation saddle point lies above the sensor at negative angles of attack and below the sensor at positive angles of attack. The corresponding probability densities also deviate from a Gaussian distribution and display a negative skewness. However, we do not observe a bimodal probability distribution at this sensor location and that is consistent with the results of Ölçmen and Simpson [26]. They found a bimodal probability distribution only when the pressure sensor was located close to or inside of the line of low shear stress. For sensor 4, which lies on or near the separation line, the spectral levels are also observed to vary with model angle of attack and the probability distributions are slightly non-Gaussian.

The RMS, $\sqrt{\bar{p^2}}/q_\infty$, the skewness, $\bar{p^3}/(\bar{p^2})^{3/2}$, and the flatness (kurtosis), $\bar{p^4}/(\bar{p^2})^2$, for sensors 1, 3, and 4 versus model angle of attack are shown in Figs. 56, 57, and 58. The uncertainty analysis on which the error bars in the plots are based, is provided in Appendix A. For sensor 1, the statistics are relatively invariant with model angle and the skewness and flatness are close to the values for a Gaussian distribution (0 and 3, respectively). The statistics for sensors 3 and 4, are dependent on the model angle and display non-Gaussian statistics.

Shifting the focus to the array of sensors near the streamwise location of the wing trailing edge (see Fig. 3a), auto-spectral densities for pressure sensors 7, 8, 9, and 10 are shown in Figs. 59, 61, 63, and 65. Here, sensor 6 was used as a reference sensor to remove facility-induced noise. The corresponding probability densities are shown in Figs. 60, 62, 64, and 66. Pressure sensors 7, 8, and 9 are generally in a region of attached flow on the fuselage, but they are likely influenced by the vortical structures emanating from the wing leading-edge juncture region, which wrap around the wing and propagate downstream. The exact nature of this influence is, however, unclear without more detailed flow-field measurements. For sensor 10, the spectra show a general shift towards lower frequencies as the model angle of attack is increased. At the largest negative angles of attack, the corner-flow separation is relatively small and sensor 10 lies outside the separated flow region. As the angle of attack is increased, however, the corner-flow separation covers the sensor and the shift in the spectral content to lower frequencies may be related to the large-scale flow recirculation in the separated flow region. The RMS, skewness, and flatness for sensors 7, 8, 9, and 10 versus model angle of attack are shown in Figs. 67, 68, and 69. The skewness and flatness for sensors 7, 8, and 9 show some deviations from Gaussian behavior, while sensor 10 shows larger deviations, especially when the corner-flow separation is large enough to encompass the sensor.

Auto-spectral densities for pressure sensors 11, 12, and 13 are shown in Figs. 70, 72, and

74. Here, sensor 14 was used as a reference sensor to remove facility-induced noise. The corresponding probability densities are shown in Figs. 71, 73, and 75. In general, the spectra for these sensors show a shift in the energy from higher frequencies to lower frequencies as the model angle of attack is increased. The exact reason for this trend is unclear without more detailed measurements. However, oil-flow visualizations under the wing and near the trailing edge do appear to indicate attached flow. The RMS, skewness, and flatness for sensors 11, 12, and 13 are shown in Figs. 76, 77, and 78. The RMS pressure does not vary significantly with angle of attack, so the observed shift in spectral energy from higher frequencies to low frequencies occurs with nearly constant broadband energy. The skewness and flatness indicate that the pressure fluctuations for these sensors have small deviations from Gaussian behavior.

4.2.2 F6 Wing with Leading-Edge Horn

Unsteady pressure data for the F6 wing with leading-edge horn configuration was collected for model angles of attack ranging from -10° to 10° and $Re_c = 2.4$ million. As before, consider first the unsteady pressure measurements in the leading-edge region of the wing. The approximate locations of the pressure sensors in this region (sensors 1, 2, and 4—sensor 3 was located underneath the leading-edge horn) relative to the leading-edge surface-flow topology at $\alpha = 5^\circ$ are annotated in Fig. 49. Sensors 1 and 2 lie just ahead of the separation line and sensor 4 lies downstream of the separation line and below the leading-edge horn. Auto-spectral densities for sensors 1 and 4 are shown in Figs. 79 and 80. Sensor 2 was used as the reference sensor for facility noise removal. The probability densities for these sensors—and for all further pressure-sensor data presented below—are not shown for brevity and in general, they were found to be similar to those presented above for the F6 wing. For sensor 1, the spectra are broadband in character with weak dependence on the model angle. For sensor 4, the spectral levels increase significantly with increasing model angle. The RMS, skewness, and flatness for pressure sensors 1 and 4 are shown in Figs. 81, 82, and 83.

Auto-spectral densities for sensors 7, 8, 9, and 10, located near the wing trailing edge, are shown in Figs. 84, 85, 86, and 87. Sensor 6 was used as the reference sensor for facility noise removal. The spectra for sensors 7, 8, and 9 are similar to those obtained for the F6 wing configuration (Figs. 59, 61, and 63), except that there is more energy at lower frequencies (below 100 Hz) for the F6 wing with leading-edge horn. If the turbulent pressure fluctuations at these sensors are influenced by flow structures emanating from the leading-edge region of the wing, then the addition of the leading-edge horn may account for the observed differences. For sensor 10, the pressure spectra are qualitatively similar to the pressure spectra for the F6 wing (see Fig. 65) and they show the shift in the spectral energy towards lower frequencies with increasing model angle of attack. The RMS, skewness, and flatness for pressure sensors 7, 8, 9, and 10 are shown in Figs. 88, 89, and 90.

Auto-spectral densities for sensors 11, 12, and 13, located below the wing trailing edge, are shown in Figs. 91, 92, and 93. Sensor 14 was used as the reference sensor for facility noise removal. Similar to the F6 wing, the pressure spectra at sensors 11, 12, and 13 display a shift from higher frequencies to lower frequencies with an increasing model angle of attack. The RMS, skewness, and flatness for pressure sensors 11, 12, and 13 are shown in Figs. 94, 95, and 96.

4.2.3 NACA 0015 Wing

Unsteady pressure data for the NACA 0015 wing configuration was collected for model angles of attack ranging from 0° to 10° and $Re_c = 2.4$ million. Auto-spectral densities for sensors 2 and 3, which lie in the leading-edge region of the wing (see Fig. 3b), are shown in Figs. 97 and 98. Sensor 1 was used as the reference sensor for facility noise removal. Sensor

2 lies in the approach flow, directly ahead of the wing leading edge, and the spectra for this sensor are invariant with model angle. Sensor 3 lies downstream of the leading edge and above the upper surface of the wing, and the spectra for this sensor show a slight shift in the spectral energy from low frequencies to higher frequencies as the model angle increases. Despite this shift, the broadband RMS pressure is relatively constant with model angle as observed in Fig. 99. The skewness and flatness for sensors 2 and 3 are shown in Figs. 100 and 101.

Auto-spectral densities for sensors 8 and 9, which lie above the trailing edge of the wing, are shown in Fig. 102 and 103. Sensor 6 was used as the reference sensor for facility noise removal. Given the small size of the corner-flow separation for this wing (see Section 4.1.2), sensor 9 lies outside of the separated flow region for all of the model angles considered. Therefore, unlike the F6 wings where the corner-flow separations encompass the pressure sensor, we do not observe a dramatic increase in spectral energy and we do not see a shift in the frequency content towards lower frequencies as the model angle of attack is increased. Auto-spectral densities for sensors 10 and 11, which lie below the trailing edge of the wing, are shown in Figs. 104 and 105. Sensor 14 was used as the reference sensor for facility noise removal. Similar to the pressure spectra below the trailing edge of the F6 wings, sensor 10 shows a shift in the frequency content from higher-frequencies to lower frequencies as the model angle of attack is increased. The RMS, skewness, and flatness for pressure sensors 8, 9, 10, and 11 are shown in Figs. 106, 107, and 108. Of particular note is that the RMS, skewness, and flatness at $\alpha = 0^\circ$ are equal for sensors 8 and 11 and for sensors 9 and 10. This equality is expected since the NACA 0015 wing is symmetric and the two sensor pairs are positioned roughly symmetrically about the wing trailing edge. As a final example of the symmetry in the turbulent pressure field, consider the auto-spectral densities shown in Fig. 109 for sensors 8, 9, 10, and 11 at $\alpha = 0^\circ$. Here, the spectra for sensors 8 and 11 and for sensors 9 and 10 are remarkably similar.

4.2.4 F6 S12 Wing

Unsteady pressure data for the F6 S12 wing configuration was collected for model angles of attack ranging from 0° to 10° and $Re_c = 2.4$ million. Auto-spectral densities for sensors 2 and 3, which lie in the leading-edge region of the wing (see Fig. 3c), are shown in Figs. 110 and 111. Sensor 1 was used as the reference sensor for facility noise removal. Similar to the NACA 0015, sensor 2 lies in the approach flow, directly ahead of the wing leading edge, and the spectra are nearly invariant with model angle. For sensor 3, which lies downstream of the leading edge and above the upper surface of the wing, the spectra generally show an increase in energy across all frequencies as the model angle is increased. The RMS, skewness, and flatness for sensors 2 and 3 are shown in Figs. 112, 113, and 114.

Auto-spectral densities for sensors 8 and 9, which lie above the trailing edge of the wing are shown in Figs. 115 and 116. Sensor 6 was used as the reference sensor for facility noise removal. For sensor 9, which is closest to the wing trailing edge, there is a general shift in the frequency content toward lower frequencies with increasing model angle. That behavior is similar to the sensor 10 spectra for the F6 wings (see Figs. 65 and 87) where the corner-flow separation was large enough to encompass the sensor as the model angle was increased. Auto-spectral densities for sensors 10 and 11, which lie below the trailing edge of the wing, are shown in Figs. 117 and 118. Sensor 14 was used as the reference sensor for facility noise removal. Similar to the pressure spectra below the trailing edge for the other wings considered, sensor 10 shows a shift in frequency content from higher frequencies to lower frequencies as the model angle of attack is increased. The RMS, skewness, and flatness for pressure sensors 8, 9, 10, and 11 are shown in Figs. 119, 120, and 121. Similar to the NACA 0015 wings, the RMS, skewness and flatness at $\alpha = 0^\circ$ are nearly equal for sensors 8 and 11 and for sensors 9 and 10. This equality is again expected due to the symmetric shape

of the F6 S12 wing section and to the symmetric positioning of the sensor pairs about the wing trailing edge.

4.3 Accelerometer Results

For each of the model configurations, time series for the three orthogonal components of acceleration were measured. As noted earlier in Section 2.5, these measurements were provided by accelerometers mounted inside the model to a fixture on the wing box. From one configuration to another, the characteristics of the acceleration measurements were generally similar, and so here, we provide an example data set for configuration 4 (F6 wings with leading-edge horns). Auto-spectral densities for the x -, y -, and z -components of the acceleration are shown in Fig. 122 for model angles ranging from -10° to 10° and $Re_c = 2.4$ million. Generally, the spectra indicate a broad range of active frequencies up to the bandwidth of the accelerometers (≈ 5 kHz) and the spectral content is weakly dependent of the model angle. Using the measured acceleration amplitudes and the acceleration sensitivity of the pressure transducers, we found the equivalent pressures produced by the model motion to be below the noise floor of our measurement system.

The RMS acceleration for the x -, y -, and z -components are shown in Fig. 123 for chord Reynolds numbers of 1.8, 2.4, and 2.6 million. Here, we observe the x - and z -components of RMS acceleration to increase with increasing Reynolds number. For the lateral model motion (y -component), the dependence on Reynolds number is much weaker.

5 Conclusions

In this report, we presented the results of a risk-reduction wind-tunnel test on a juncture-flow model that consisted of a generic fuselage and a set of six candidate wing designs. The primary objective of the test was to provide data that would help guide the selection of a wing design for a forthcoming, fully-instrumented juncture-flow model. The ideal wing design would be one in which the flow at the wing trailing-edge corner was fully-attached and then progressed through incipient separation to fully separated corner-flow as the model was swept through a range of increasing angles of attack. To assess the state of the flow in the trailing-edge corner regions of the six wing candidates, oil-flow visualizations were performed. Except for the NACA 0015 wing, none of the other wing candidates displayed a fully-attached corner-flow region for the model angles that were considered. Instead, the F6, the F6 with leading-edge horn, the NACA 0015 mod, the F6 S12, and the COCA wings all displayed corner-flow separations that grew in size with increasing model angle. While the corner-flow on the NACA 0015 wing did eventually separate at model angles of attack above 5° , the size of the separation was small and it would be difficult to achieve adequate resolution of the flow field with off-body measurement techniques. In contrast, the F6 wings—with or without a leading-edge horn—showed a smooth progression from a relatively small corner-flow separation to a large one with increasing angle of attack and the size is adequate for off-body measurements. The F6 S12 and COCA wings were found to have corner flow separations with a more complex surface topology and the geometry of the wing, particularly near the wing root, would limit the survey region of LDV measurements.

Oil-flow visualizations were also performed in the leading-edge regions of the six wing candidates. For the F6 wing in particular, the surface flow suggested the presence of a horseshoe-vortex system and displayed a surface topology that was consistent with previous studies of wing-body juncture flows [2, 4]. The other wings, all with leading-edge horns, displayed less distinct surface-flow patterns and any horseshoe-vortex system that may have been present, appeared to be weakened by the leading-edge horn. However, several of these wings displayed a region of separated flow at the trailing edge, just outboard of the

corner-flow region, and that appeared to be induced by a flow structure emanating from the leading-edge horn.

Measurements of the corner flow separation size were reported for several of the candidate wing designs and that information will be used to define the survey regions for the embedded LDV and PIV measurements that are planned for the fully-instrumented juncture-flow model. The corner flow separation size measurements will also be used to guide the placement of unsteady pressure transducers on the fully-instrumented model. Oil-flow visualizations in the leading-edge regions of the wings will be used to define the survey regions for a 2nd embedded LDV system and they will also guide the placement of pressure transducers to capture the unsteady dynamics of the leading-edge horseshoe-vortex system.

Unsteady pressure measurements on the fuselage were found to be contaminated by facility-induced noise. To remove that noise from the unsteady pressure time series, an adaptive noise cancellation (ANC) algorithm was employed. In this approach, two pressure transducers—a primary sensor and a reference sensor—are required and they must be separated by a sufficient distance so that the turbulent pressure fluctuations sensed by each one are uncorrelated. Once the time series were processed through the ANC algorithm, they were additionally processed to obtain auto-spectral densities, probability densities, and statistics (RMS, skewness, and flatness). In light of the need for facility-noise removal, specific reference sensors will be placed on the fully-instrumented juncture-flow model to remove facility-induced noise from the primary sensors that are of interest.

References

1. Rumsey, C. L.; Neuhart, D. H.; and Kegerise, M. A.: The NASA Juncture Flow Experiment: Goals, Progress, and Preliminary Testing (Invited). AIAA Paper 2016-1557, January 2016.
2. Simpson, R. L.: Juncture Flows. *Annual Review of Fluid Mechanics*, vol. 33, 2001, pp. 415–443.
3. Devenport, W. J.; and Simpson, R. L.: Turbulence Structure Near the Nose of a Wing-Body Junction. AIAA Paper 87-1310, June 1987.
4. Devenport, W. J.; and Simpson, R. L.: Time-Dependent and Time-Averaged Turbulence Structure Near the Nose of a Wing-Body Junction. *Journal of Fluid Mechanics*, vol. 210, 1990, pp. 23–55.
5. Gand, F.; Brunet, V.; and Deck, S.: A Combined Experimental, RANS, and LES Investigation of a Wing Body Junction Flow. AIAA Paper 2010-4753, July 2010.
6. Barber, T. J.: An Investigation of Strut-Wall Intersection Losses. *Journal of Aircraft*, vol. 15, no. 10, October 2010, pp. 676–681.
7. Gand, F.; Deck, S.; and Brunet, V.: Flow Dynamics Past a Simplified Wing Body Junction. *Physics of Fluids*, vol. 22, no. 11, November 2010, p. 115111.
8. Gentry, G. L.; Quinto, F. P.; Gatlin, G. G.; and Applin, Z. T.: The Langley 14- by 22-Foot Subsonic Tunnel. NASA TP 3008, 1990.
9. Campbell, R. L.: Efficient Viscous Design of Realistic Aircraft Configurations. AIAA Paper 98-2539, June 1998.
10. Panton, R. L.; and Miller, J. M.: Resonant Frequencies of Cylindrical Helmholtz Resonators. *J. Acoust. Soc. Am.*, vol. 57, no. 6, June 1975, pp. 1533–1535.

11. Simpson, R. L.; Ghodbane, M.; and McGrath, B. E.: Surface Pressure Fluctuations in a Separating Turbulent Boundary Layer. *Journal of Fluid Mechanics*, vol. 177, April 1987, pp. 167–186.
12. Agarwal, N. K.; and Simpson, R. L.: A New Technique for Obtaining the Turbulent Pressure Spectrum from the Surface Pressure Spectrum. *Journal of Sound and Vibration*, vol. 135, no. 2, December 1989, pp. 346–350.
13. Goody, M. C.: An Experimental Investigation of Pressure Fluctuations in Three-Dimensional Turbulent Boundary Layers. Ph.D. Thesis, Virginia Polytechnic Institute and State University, Blacksburg, VA, September 1999.
14. Naguib, A. M.; Gravante, S. P.; and Wark, C. E.: Extraction of Turbulent Wall-Pressure Time-Series using an Optimal Filtering Scheme. *Experiments in Fluids*, vol. 22, 1996, pp. 14–22.
15. Widrow, B.; and Stearns, S. D.: *Adaptive Signal Processing*. Prentice Hall, Upper Saddle River, NJ, 1985.
16. Gravante, S. P.; Naguib, A. M.; Wark, C. E.; and Nagib, H. M.: Characterization of the Pressure Fluctuations Under a Fully Developed Turbulent Boundary Layer. *AIAA Journal*, vol. 36, no. 10, October 1998, pp. 1808–1816.
17. Braslow, A. L.; Hicks, R. M.; and Harris, R. V.: Use of Grit-Type Boundary-Layer-Transition Trips on Wind-Tunnel Models. NASA TN D-3579, September 1966.
18. Braslow, A. L.; and Knox, E. C.: Simplified Method for Determination of Critical Height of Distributed Roughness Particles for Boundary-Layer Transition at Mach Numbers from 0 to 5. NASA TN 4363, September 1958.
19. Squire, L. C.: The Motion of a Thin Oil Sheet under the Steady Boundary Layer on a Thin Body. *Journal of Fluid Mechanics*, vol. 11, no. 2, September 1961, pp. 161–179.
20. Merzkirch, W.: *Flow Visualization*. Academic Press, New York, NY, 1974.
21. Yang, W., ed.: *Handbook of Flow Visualization*, Hemisphere Publishing Corporation, chapter 7. 1989, p. 97.
22. Merzkirch, R.: Techniques of Flow Visualization. AGARD AG 301, 1987.
23. Lu, F. K.: Surface Oil Flow Visualization. *Eur. Phys. J. Special Topics*, vol. 182, 2010, pp. 51–63.
24. Kuester, M. S.; Borgoltz, A.; and Devenport, W. J.: Experimental Visualization of Juncture Separation Bubbles at Low- to Moderate-Reynolds Numbers. AIAA Paper 2016-3880, June 2016.
25. Brooks, T. F.; and Hodgson, T. H.: Trailing Edge Noise Prediction from Measured Surface Pressures. *Journal of Sound and Vibration*, vol. 78, no. 1, 1981, pp. 69–117.
26. Ölçmen, S. M.; and Simpson, R. L.: Influence of Wing Shapes on Surface Pressure Fluctuations at Wing-Body Junctions. *AIAA Journal*, vol. 32, no. 1, January 1994, pp. 6–15.
27. Benedict, L. H.; and Gould, R. D.: Towards Better Uncertainty Estimates for Turbulence Statistics. *Experiments in Fluids*, vol. 22, 1996, pp. 129–136.

Appendix A. Uncertainty Analysis

A.1. Uncertainty in the Corner-Flow Separation Size

In this section, we provide an uncertainty analysis for the measurements of the corner-flow separation width and length. To facilitate the discussion, the uncertainty analysis for the F6 wing with leading-edge horn is used as an example. For the width measurement, the distance between the fuselage and the outer edge of the collection of oil-flow pigment at the trailing-edge boundary of the corner separation was measured with a ruler that had 1 mm divisions. Therefore, the systematic measurement uncertainty was ± 0.5 mm. To derive a random measurement uncertainty, multiple oil-flow runs were performed at a model angle of attack of $\alpha = 5^\circ$. Five runs were performed, four with our standard oil-flow formula and one with a modified, more viscous formula. Three of the runs were performed early in the test campaign and two runs were performed later in the test campaign, after several wing changes. The standard deviation in the measured width for these five runs was 2.65 mm. Assuming that these five measurements were drawn from a population with a Gaussian distribution, the random uncertainty for a 95% confidence interval was found to be ± 7.34 mm. That is approximately 16% of the measured corner-flow separation width at $\alpha = 5^\circ$. To obtain the random uncertainties in the width at other model angles, where multiple oil-flow runs were not performed, we assumed a similar percent random uncertainty. The total uncertainty for the width measurement was then calculated as the root-sum-square of the systematic and random uncertainties.

The length of the corner-flow separation was also measured with the ruler. However, due to the diffuse collection of oil-flow pigment at the wing root, it was more difficult to identify where the corner-flow separation began and so, by observation, the systematic uncertainty in the length measurement was approximately ± 2 mm. For the five oil-flow runs, the standard deviation in the length measurement was 4.87 mm and assuming a Gaussian distribution, the 95% confidence interval was found to be ± 13.5 mm. This is approximately 13% of the length measurement at $\alpha = 5^\circ$. As before, we then assumed a similar percent random uncertainty for the other model angles of attack and calculated the total uncertainty as the root-sum-square of the systematic and random uncertainties.

A.2. Uncertainty in the Unsteady Pressure Statistics

In this section, we provide an uncertainty analysis for the unsteady pressure statistics. This uncertainty analysis applies only to the statistics derived from a given pressure time series acquired during a given run. Uncertainties associated with run-to-run variability are not accounted for because those data were not acquired and it was beyond the scope of the present risk-reduction experiment.

Consider first the data reduction equation used to calculate the unsteady pressure from the measured voltage time series:

$$p(t) = \frac{sv(t)}{G} \quad (6)$$

where s is the sensitivity of the sensor as determined by calibration, $v(t)$ is the AC-coupled voltage time series, and G is the filter gain. The r th-order central moment of the unsteady pressure is defined as:

$$\bar{p}^r = \frac{1}{N} \sum_{i=1}^N (p_i - \bar{p})^r \quad (7)$$

where N is the number of independent samples, p_i is the i th pressure reading, \bar{p} is the mean pressure (which in our case is zero since $\bar{v} = 0$), and r is an integer. Combining Equations

6 and 7 we obtain:

$$\bar{p}^r = \left(\frac{s}{G}\right)^r \frac{1}{N} \sum_{i=1}^N (v_i - \bar{v})^r = \left(\frac{s}{G}\right)^r \bar{v}^r \quad (8)$$

where \bar{v}^r is the r th-order central moment of the voltage time series. Assuming that the variables in Eq. 8 are independent of one another and that the uncertainties of these variables are independent of one another, the uncertainty in the r th-order central moment of the unsteady pressure is given by:

$$U_{\bar{p}^r}^2 = \left(\frac{\partial \bar{p}^r}{\partial s}\right)^2 U_s^2 + \left(\frac{\partial \bar{p}^r}{\partial G}\right)^2 U_G^2 + \left(\frac{\partial \bar{p}^r}{\partial \bar{v}^r}\right)^2 U_{\bar{v}^r}^2 \quad (9)$$

Evaluating the partial derivatives in this equation, we obtain:

$$U_{\bar{p}^r}^2 = r^2 \left(\frac{s^{r-1}}{G^r} \bar{v}^r\right)^2 U_s^2 + r^2 \left(\frac{s^r}{G^{r+1}} \bar{v}^r\right)^2 U_G^2 + \left(\frac{s}{G}\right)^{2r} U_{\bar{v}^r}^2 \quad (10)$$

and from this equation, expressions for the uncertainty in the 2nd-, 3rd-, and 4th-order central moments ($r = 2, 3$, and 4) of the unsteady pressure can be obtained.

The uncertainty in the pressure sensor sensitivity, U_s , was found to be $\pm 1.35\%$ of s on the basis of a Monte-Carlo uncertainty analysis of the sensor calibration data. The uncertainty in the filter gain, U_G , was 0.02% of the gain. The uncertainties in the r th-order central moments of the voltage time series are due to the sampling variance. The sampling variance in the r th-order central moments of the voltage is given as [27]:

$$\text{var}(\bar{v}^r) = \frac{1}{N} (\mu_{2r} - \mu_r^2 + r^2 \mu_{r-1}^2 \mu_2 - 2r \mu_{r+1} \mu_{r-1}) \quad (11)$$

where the μ_r represent the exact r th-order central moments of the probability distribution. We generally do not know these values, but large sampling theory arguments ($N > 1000$) allow us to replace the μ_r with the central moment sampling statistics, \bar{v}^r . From the sampling variance, the 95% confidence interval for the r th-order central moment is:

$$\bar{v}^r \pm 1.96 [\text{var}(\bar{v}^r)]^{1/2} \quad (12)$$

and so, for the purposes of our uncertainty analysis, the uncertainty in the r th-order central moment is:

$$U_{\bar{v}^r} = \pm 1.96 [\text{var}(\bar{v}^r)]^{1/2} \quad (13)$$

In the use of Eq. 11, the samples are assumed to be independent. This requires that the data rate be less than $1/(2T_p)$ where T_p is the integral time scale of the unsteady pressure:

$$T_p = \frac{1}{\sigma_p^2} \int_o^\infty R_{pp}(\tau) d\tau \quad (14)$$

where $R_{pp}(\tau)$ is the autocorrelation of the unsteady pressure and σ_p is the standard deviation of the unsteady pressure. Generally, we sample the unsteady pressure at a much higher rate, so when we calculate the sampling variance, we only consider samples separated in time by $2T_p$. This can result in an N that is considerably less than the total number of samples we acquired, and it varies depending on where the pressure sensor is located.

The following are the specific formulas used for the variances of the 2nd-, 3rd-, and 4th-order central moments. The variance for the 2nd-order central moment is given as:

$$\text{var}(\bar{v}^2) = \frac{1}{N} (\bar{v}^4 - \bar{v}^2)^2 + 4\bar{v}^2 \bar{v}^2 - 4\bar{v}^3 \bar{v} = \frac{1}{N} (\bar{v}^4 - \bar{v}^2)^2 \quad (15)$$

where the fact that $\bar{v} = 0$ was used. The variance for the 3rd-order central moment is given as:

$$\text{var}(\bar{v}^3) = \frac{1}{N} (\bar{v}^6 - \bar{v}^{3^2} - 6\bar{v}^4 \bar{v}^2 + 9\bar{v}^{2^3}) \quad (16)$$

and the variance for the 4th-order central moment is given as:

$$\text{var}(\bar{v}^4) = \frac{1}{N} (\bar{v}^8 - \bar{v}^{4^2} - 8\bar{v}^5 \bar{v}^3 + 16\bar{v}^{3^2} \bar{v}^2) \quad (17)$$

Generally, we plot the 2nd-, 3rd-, and 4th-order moments of the unsteady pressure in a nondimensional form. For the RMS pressure, we plot $\sqrt{\bar{p}^2}/q_\infty$, and the uncertainty associated with that quantity is:

$$U_{RMS} = \pm \left[\frac{1}{4} \left(\frac{1}{\bar{p}^2 q_\infty^2} \right) U_{\bar{p}^2}^2 + \left(\frac{\bar{p}^2}{q_\infty^4} \right) U_{q_\infty}^2 \right]^{1/2} \quad (18)$$

where U_{q_∞} is the uncertainty in the freestream dynamic pressure, which was ± 0.01 kPa for the present test. The skewness factor is defined as $\bar{p}^3/\bar{p}^2^{3/2}$ and the uncertainty is given by:

$$U_{SF} = \pm \left[\left(\frac{1}{\bar{p}^2 \bar{p}^3} \right) U_{\bar{p}^3}^2 + \frac{9}{4} \left(\frac{\bar{p}^3}{\bar{p}^5} \right) U_{\bar{p}^2}^2 \right]^{1/2} \quad (19)$$

Finally, the flatness factor is defined as \bar{p}^4/\bar{p}^2^2 and the uncertainty is given by:

$$U_{FF} = \pm \left[\left(\frac{1}{\bar{p}^4} \right) U_{\bar{p}^4}^2 + \left(\frac{4\bar{p}^4}{\bar{p}^6} \right) U_{\bar{p}^2}^2 \right]^{1/2} \quad (20)$$

Table 1. Juncture-flow model wing configurations and nominal angles of attack.

Configuration	Port Wing	Starboard Wing	α (degrees)
1	F6	F6 with L.E. horn	-10, -7.5, -5, -2.5, 0, 2.5, 5, 7.5, 10
2	NACA 0015 with L.E. horn	NACA 0015mod with L.E. horn	0, 2.5, 5, 7.5, 10
3	F6 S12 with L.E. horn	COCA with L.E. horn	0, 2.5, 5, 7.5, 10
4	F6 with L.E. horn	F6 with L.E. horn	-10, -7.5, -5, -2.5, 0, 2.5, 5, 7.5, 10

Table 2. Unsteady pressure sensor locations on the juncture-flow model fuselage.

Sensor Number	x (cm)	z (cm)
1	141.91	4.62
2	139.95	0.00
3	148.59	3.96
4	147.60	0.00
5	174.00	7.87
6	222.25	14.58
7	222.25	6.81
8	222.25	4.27
9	222.25	1.73
10	222.25	-1.73
11	222.25	-4.95
12	222.25	-6.48
13	222.25	-7.98
14	222.25	-14.58

Table 3. Measured widths and lengths (with uncertainties) of the corner-flow separation for the F6 wing (port side). Configuration 1 at $Re_c = 2.4$ million.

α (degrees)	w (mm)	U_w (mm)	ℓ (mm)	U_ℓ (mm)
-10.00	12.00	2.76	60.00	13.59
-7.50	16.00	3.66	63.00	14.26
-5.00	17.00	3.88	60.00	13.59
-2.50	21.50	4.89	67.50	15.26
0.00	22.50	5.12	62.50	14.15
2.50	32.00	7.26	73.00	16.48
5.00	38.00	8.62	88.00	19.82
7.50	43.00	9.75	104.50	23.50
10.00	54.00	12.24	120.00	26.96

Table 4. Measured widths and lengths (with uncertainties) of the corner-flow separation for the F6 wing with leading-edge horn (starboard side). Configuration 1 at $Re_c = 2.4$ million.

α (degrees)	w (mm)	U_w (mm)	ℓ (mm)	U_ℓ (mm)
-10.00	13.00	1.77	54.50	5.39
-7.50	13.00	1.77	57.00	5.60
-5.00	18.50	2.47	58.50	5.73
-2.50	25.00	3.31	70.00	6.73
0.00	31.00	4.09	76.00	7.25
2.50	40.00	5.26	90.00	8.50
5.00	46.00	6.04	107.20	10.04
7.50	51.00	6.69	120.00	11.19
10.00	65.70	8.61	130.70	12.16

Table 5. Measured widths and lengths (with uncertainties) of the corner-flow separation for the NACA 0015 wing (port side). Configuration 2 at $Re_c = 2.4$ million.

α (degrees)	w (mm)	U_w (mm)	ℓ (mm)	U_ℓ (mm)
0.00	0.00	0.00	0.00	0.00
2.50	0.00	0.00	0.00	0.00
5.00	3.00	0.50	8.00	2.00
5.00	0.00	0.00	0.00	0.00
5.00	0.00	0.00	0.00	0.00
7.50	5.50	0.50	15.30	2.00
10.00	8.00	0.50	43.00	2.00

Table 6. Measured widths and lengths (with uncertainties) of the corner-flow separation for the NACA 0015mod wing (starboard side). Configuration 2 at $Re_c = 2.4$ million.

α (degrees)	w (mm)	U_w (mm)	ℓ (mm)	U_ℓ (mm)
0.00	15.00	2.74	34.00	4.92
2.50	19.00	3.44	43.00	6.03
5.00	22.30	4.03	49.67	6.87
7.50	35.00	6.30	68.00	9.22
10.00	46.00	8.26	80.00	10.77

Table 7. Measured widths and lengths (with uncertainties) of the corner-flow separation for the F6 wing with leading-edge horn (port side). Configuration 4 at $Re_c = 2.4$ million.

α (degrees)	w (mm)	U_w (mm)	ℓ (mm)	U_ℓ (mm)
-10.00	13.00	1.77	51.00	5.09
-5.00	18.00	2.41	63.00	6.12
0.00	33.00	4.35	80.00	7.61
5.00	48.50	6.36	107.00	10.02
10.00	64.50	8.45	128.00	11.91

Table 8. Measured widths and lengths (with uncertainties) of the corner-flow separation for the F6 wing with leading-edge horn (port side). Configuration 4 at $Re_c = 2.7$ million.

α (degrees)	w (mm)	U_w (mm)	ℓ (mm)	U_ℓ (mm)
-10.00	12.00	1.65	45.50	4.63
-5.00	17.00	2.28	51.00	5.09
0.00	31.50	4.15	72.00	6.90
5.00	47.50	6.23	99.00	9.30
10.00	68.00	8.91	121.00	11.28

Table 9. Measured widths and lengths (with uncertainties) of the corner-flow separation for the F6 wing with leading-edge horn (starboard side). Configuration 4 at $Re_c = 2.7$ million.

α (degrees)	w (mm)	U_w (mm)	ℓ (mm)	U_ℓ (mm)
-10.00	13.00	1.77	40.00	4.18
-5.00	17.00	2.28	46.00	4.67
0.00	32.00	4.22	70.00	6.73
5.00	45.00	5.91	100.00	9.39
10.00	71.00	9.30	134.00	12.46

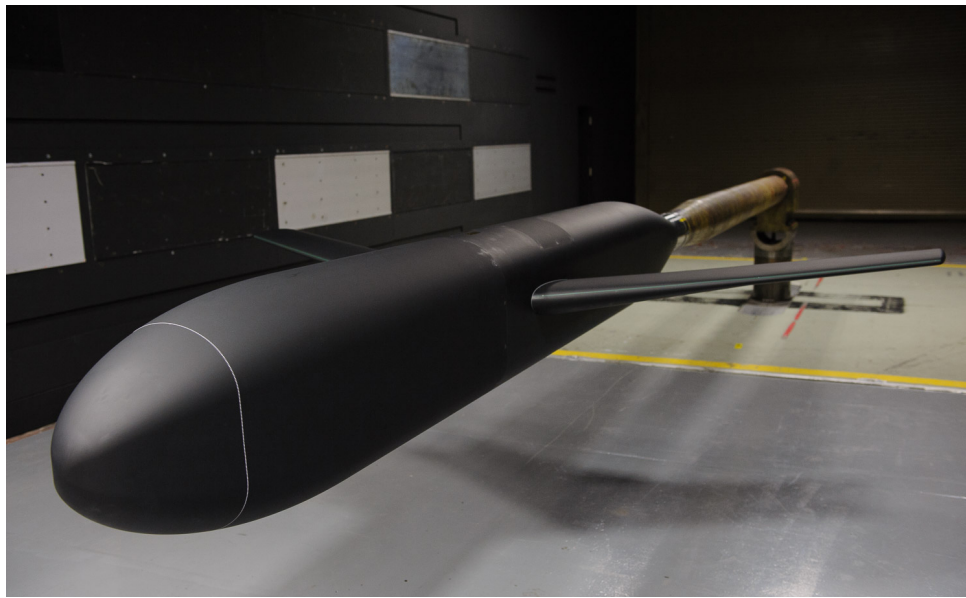
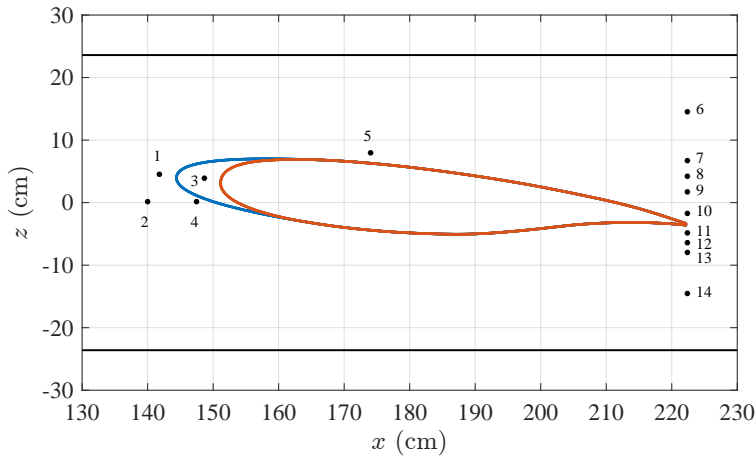


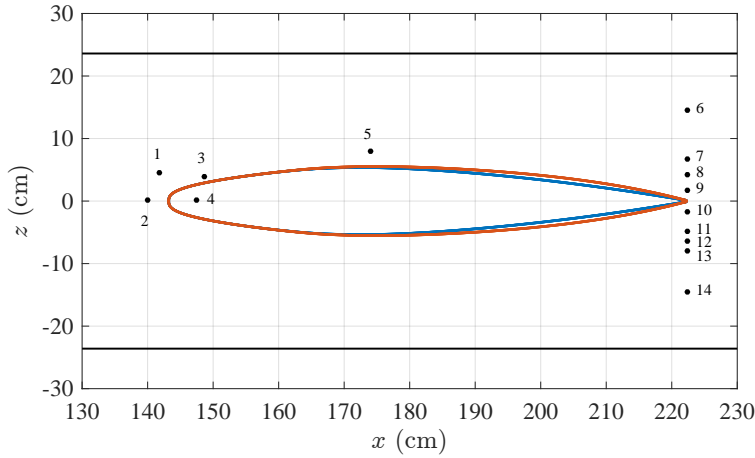
Figure 1. Image of the Juncture-Flow Model installed in the 14x22 Subsonic Wind Tunnel.



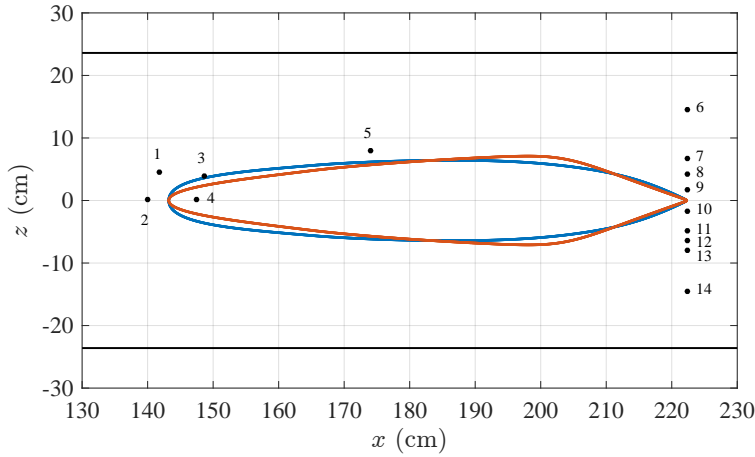
Figure 2. Front-view image of the Juncture-Flow Model installed in the 14x22 Subsonic Wind Tunnel.



(a) F6 (blue) and F6 with leading-edge horn (red).



(b) NACA 0015 (blue) and NACA 0015mod (red).



(c) F6 S12 (blue) and COCA (red).

Figure 3. Wing root section profiles. The numbered circular symbols denote the locations of the pressure transducers on the port side of the fuselage and the solid black lines in each figure denote the top and bottom of the fuselage.

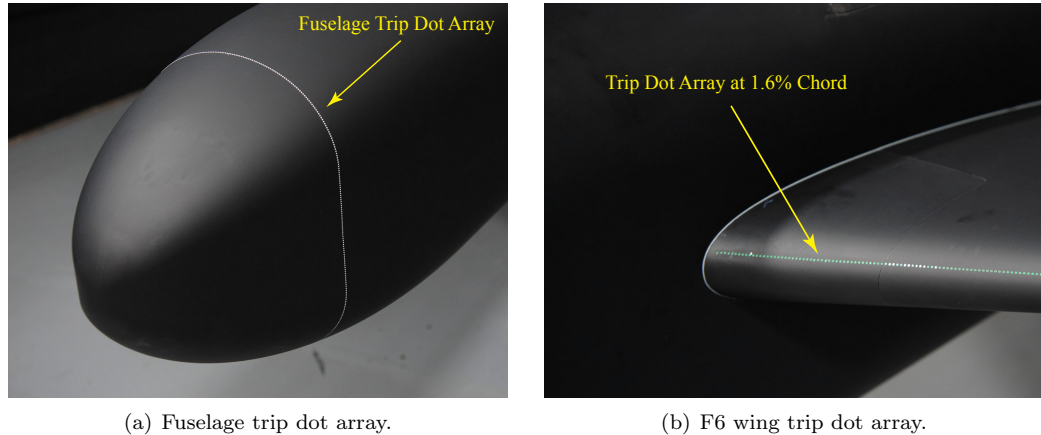


Figure 4. Example pictures of trip-dot placement on the juncture-flow model.

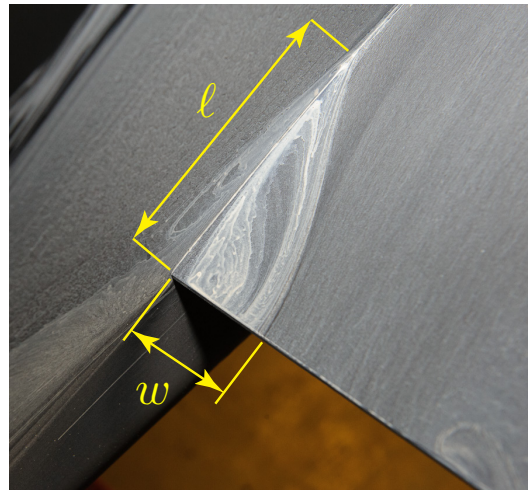


Figure 5. Definition of corner-flow separation length, ℓ , and width, w , from an example oil-flow visualization (F6 wing with leading edge horn, $\alpha = 5^\circ$, $Re_c = 2.4$ million).

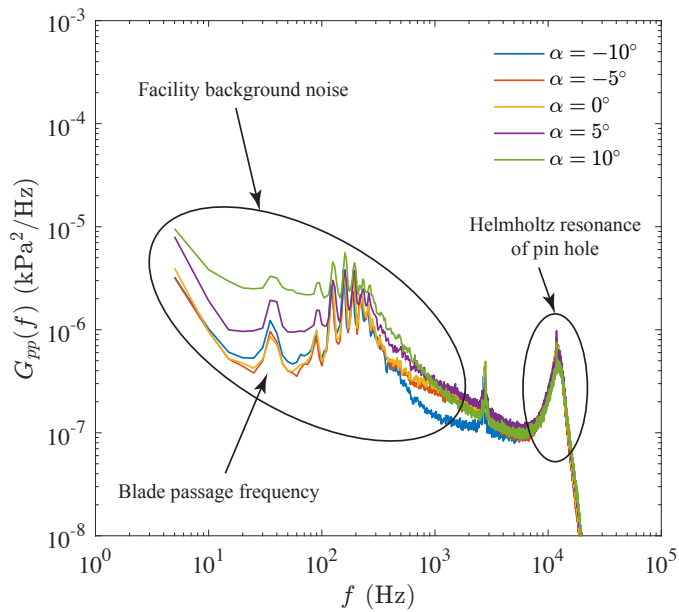


Figure 6. Auto spectral density of pressure sensor 1 versus angle of attack. F6 wing at $Re_c = 2.4$ million.

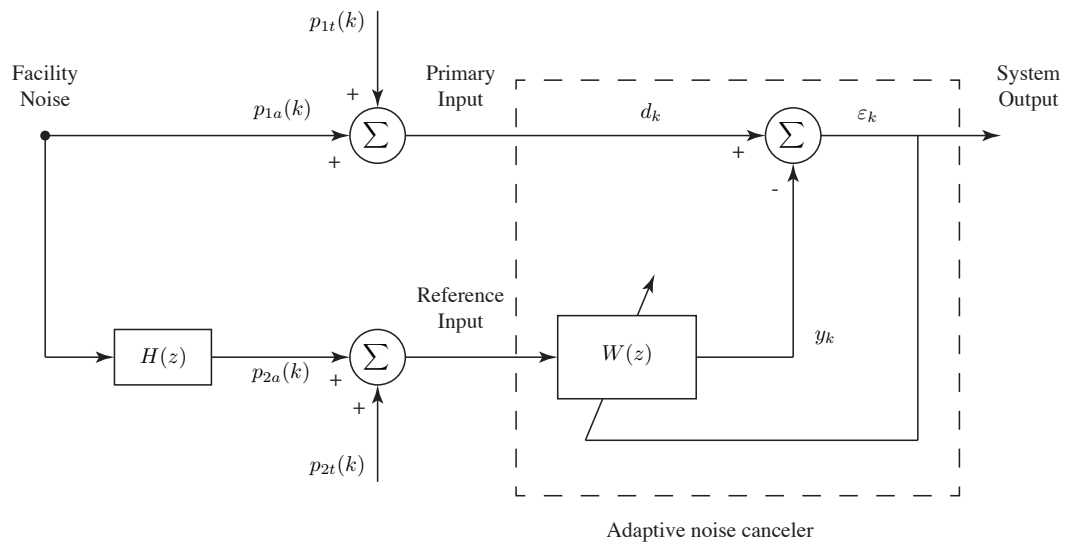


Figure 7. Block diagram of adaptive noise cancellation method for removal of facility background noise.

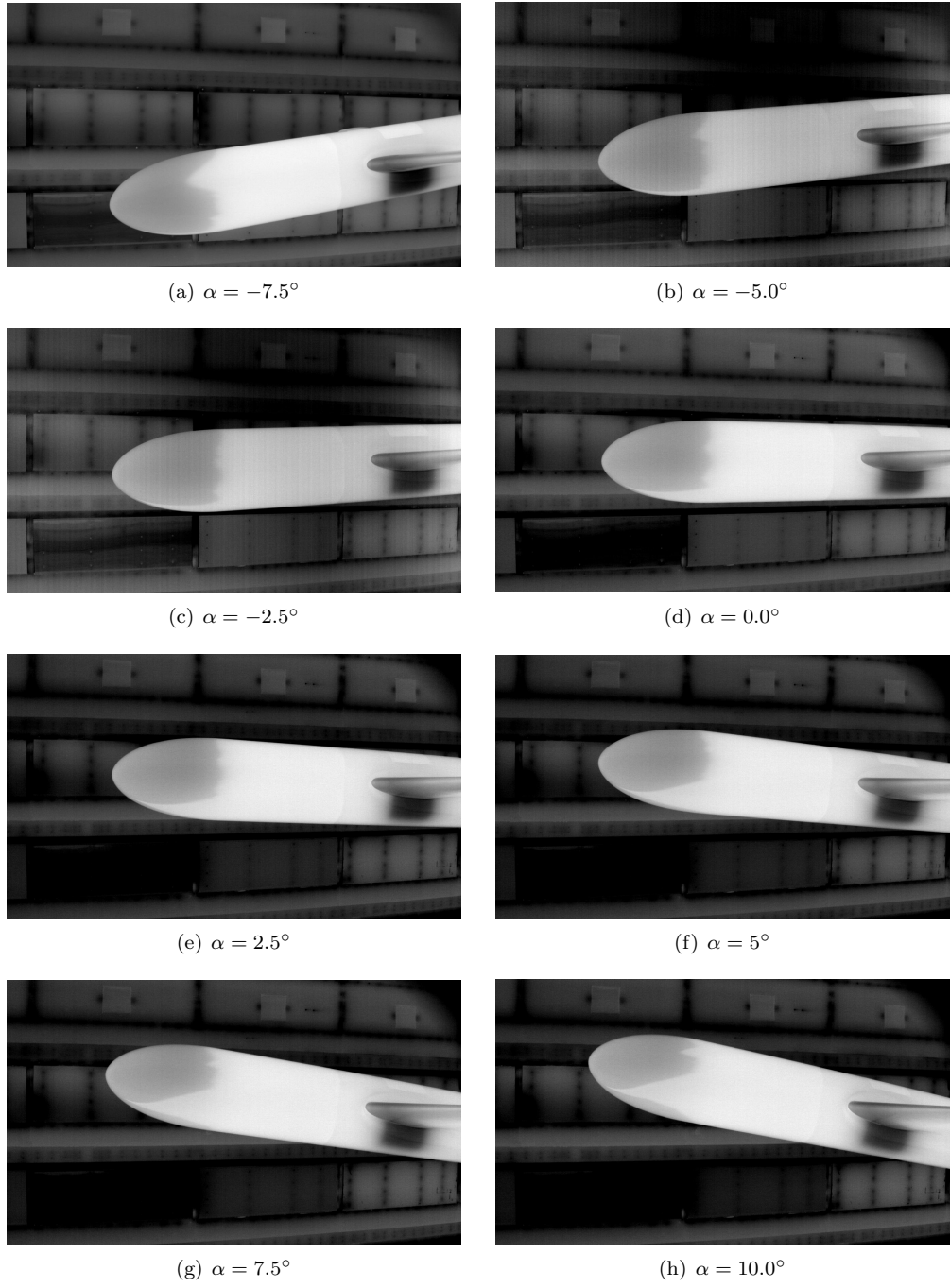


Figure 8. Infrared images of the port-side fuselage versus model angle of attack. The model was clean (no trip elements). F6 wing geometry (configuration 1) at $Re_c = 2.4$ million.

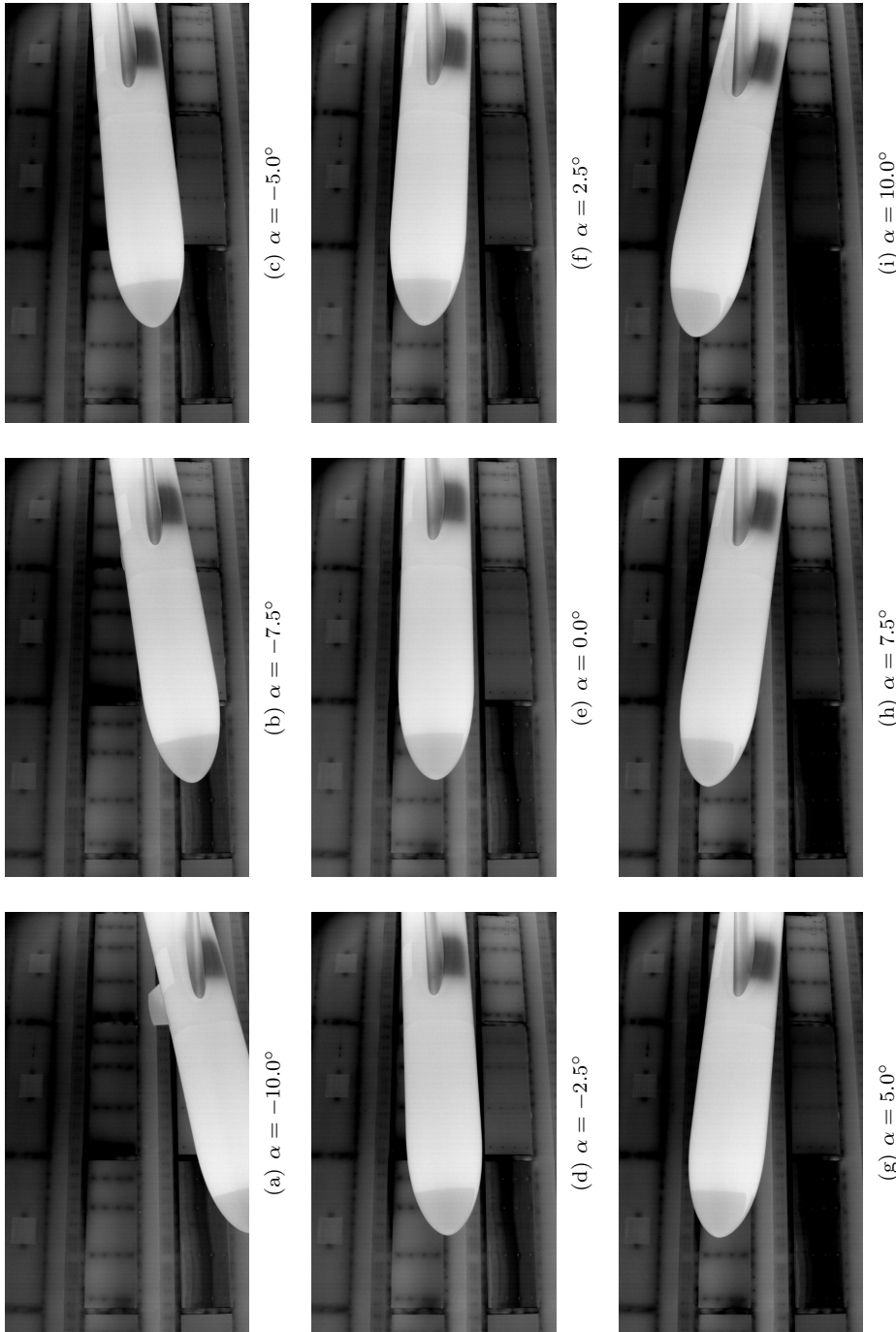


Figure 9. Infrared images of the port-side fuselage versus model angle of attack. The fuselage boundary layer was tripped with $218.4 \mu\text{m}$ trip dots located at an arc-distance of 30.48 cm from the model nose tip. F6 wing geometry (configuration 1) at $Re_c = 2.4$ million.

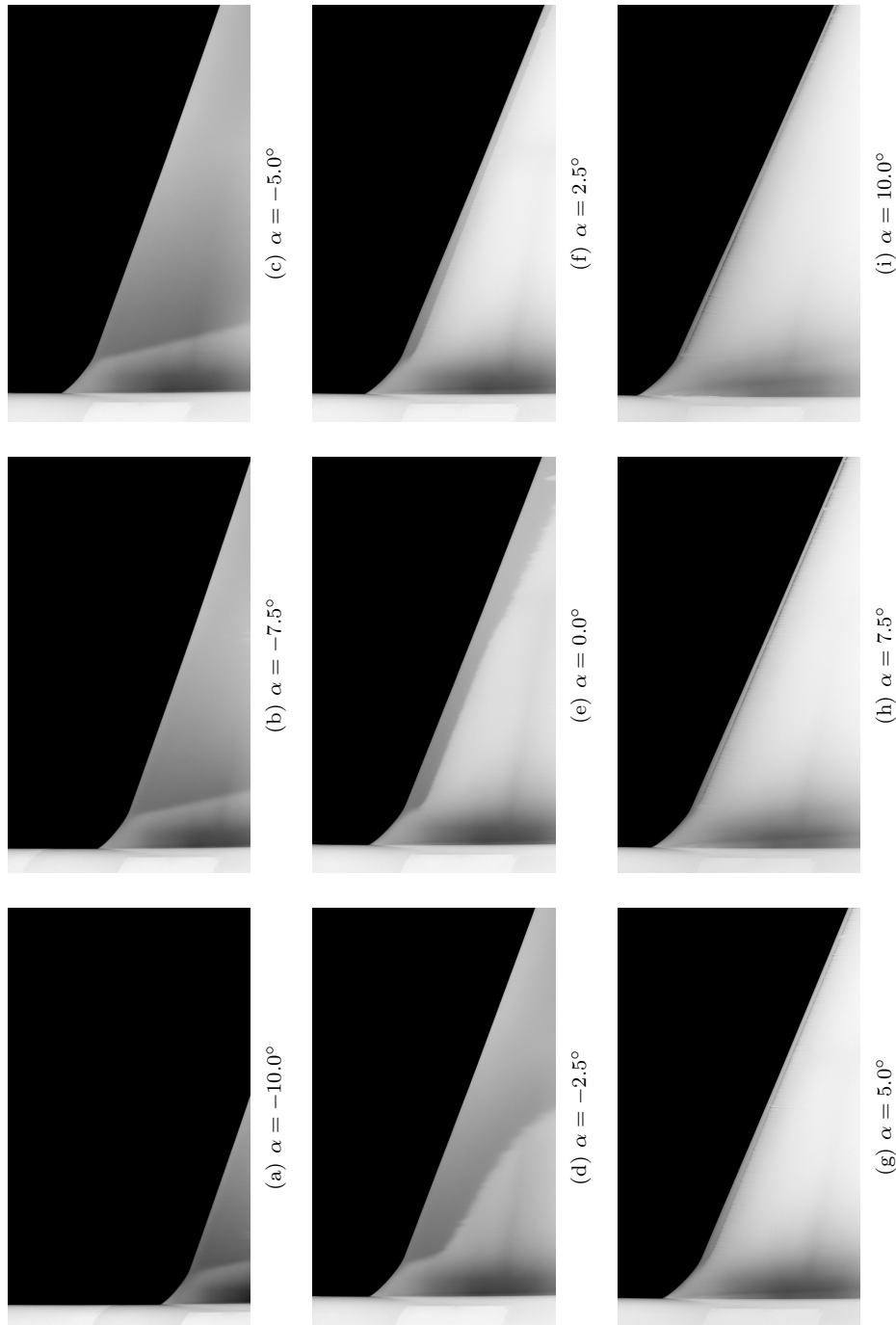


Figure 10. Infrared images of the F6 wing with leading-edge horn (starboard side) versus model angle of attack. The wing surface was clean (no trip elements) and the fuselage boundary layer was tripped. F6 wing geometry (configuration 1) at $Re_c = 2.4$ million.

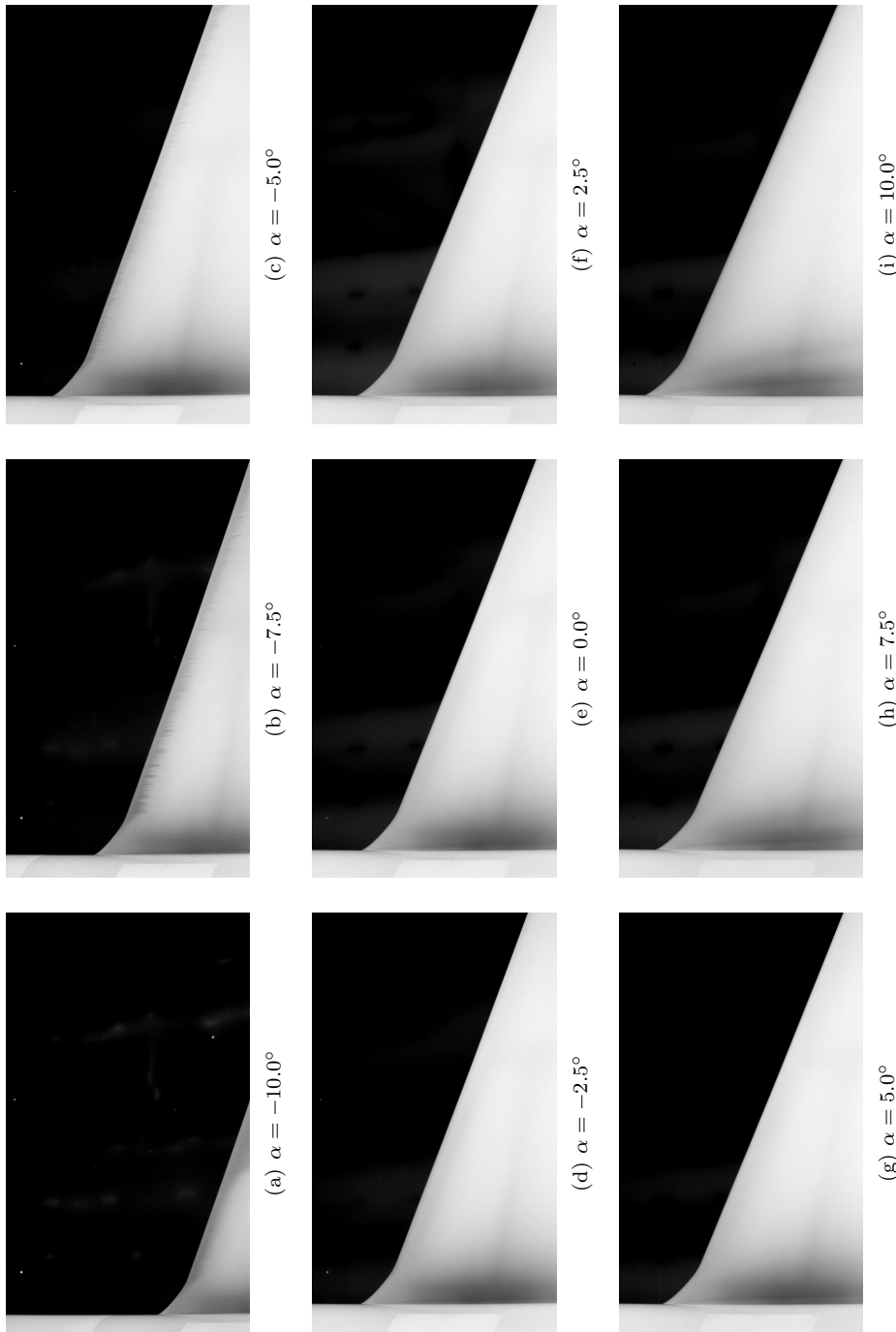


Figure 11. Infrared images of the F6 wing with leading-edge horn (starboard side) versus model angle of attack. The wing surface was tripped at 1.6% chord with $142.2 \mu\text{m}$ trip dots and the fuselage boundary layer was tripped. F6 wing geometry (configuration 1) at $Re_c = 2.4$ million.

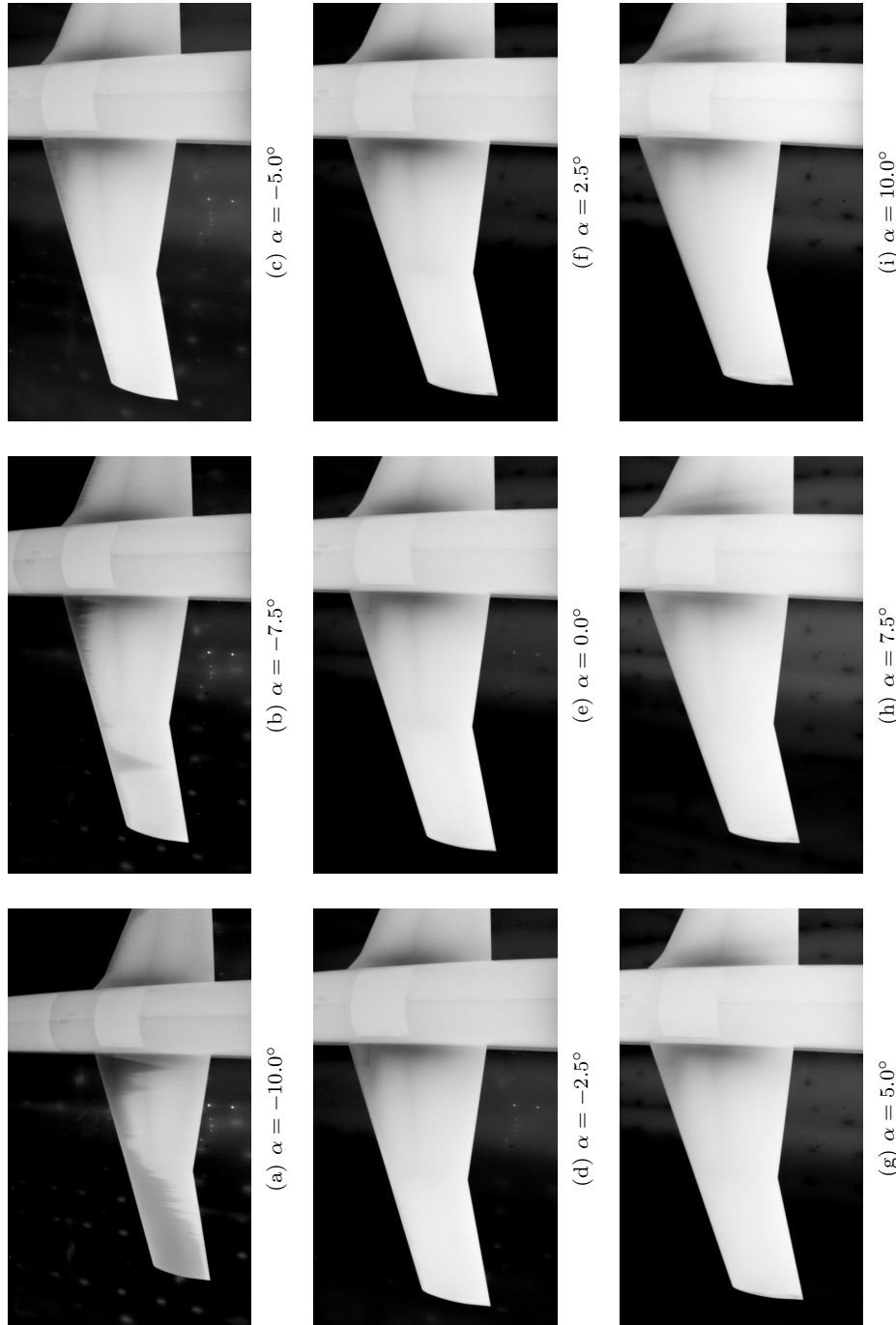


Figure 12. Infrared images of the F6 wing (port side) versus model angle of attack. The wing surface was tripped at 1.6% chord with 142.2 μm trip dots and the fuselage boundary layer was tripped. F6 wing geometry (configuration 1) at $Re_e = 2.4$ million.

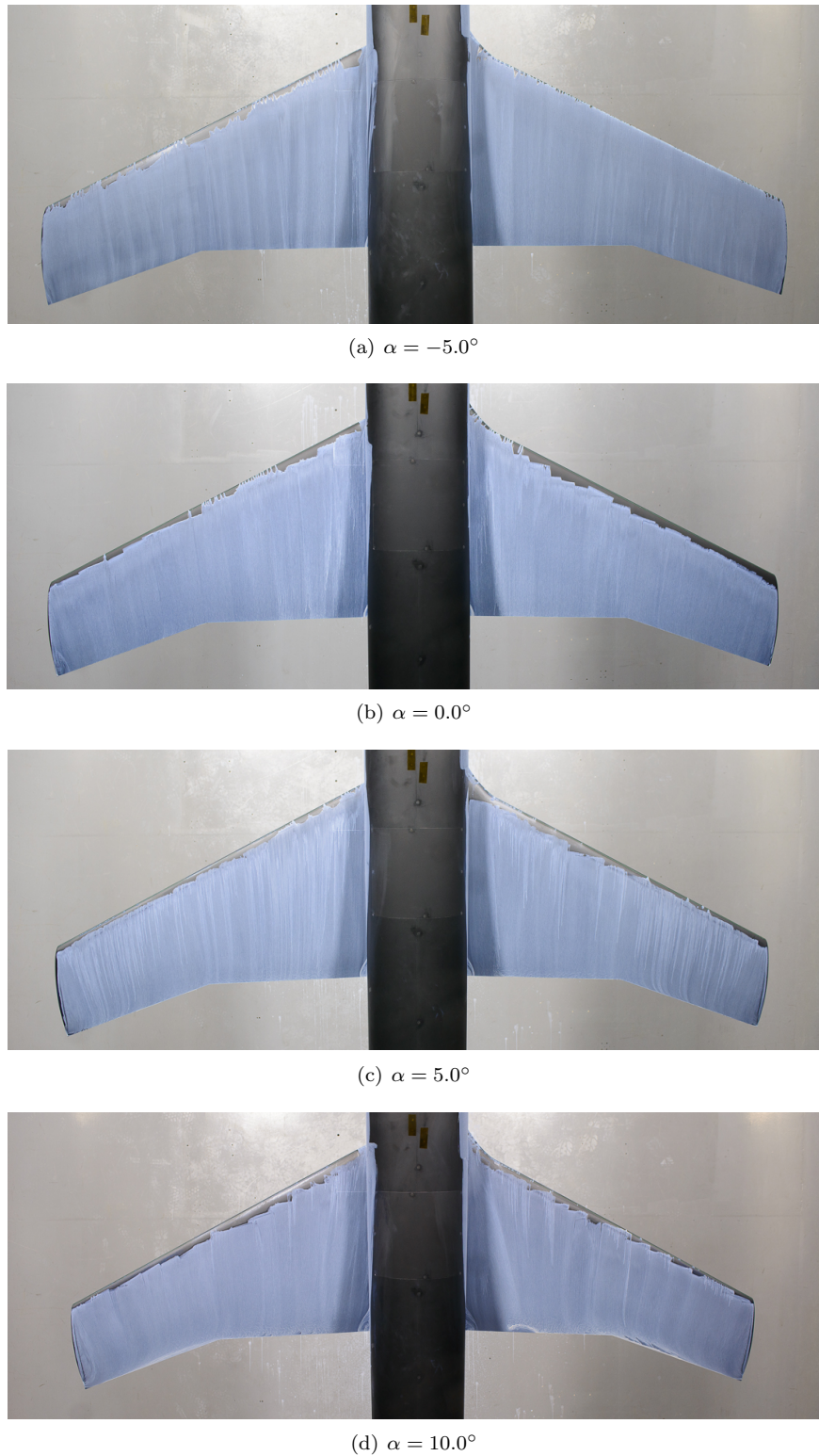


Figure 13. Planform view of the oil-flow visualization for configuration 1 versus model angle of attack. The F6 wing is on the port side and the F6 wing with leading-edge horn is on the starboard side. $Re_c = 2.4$ million.

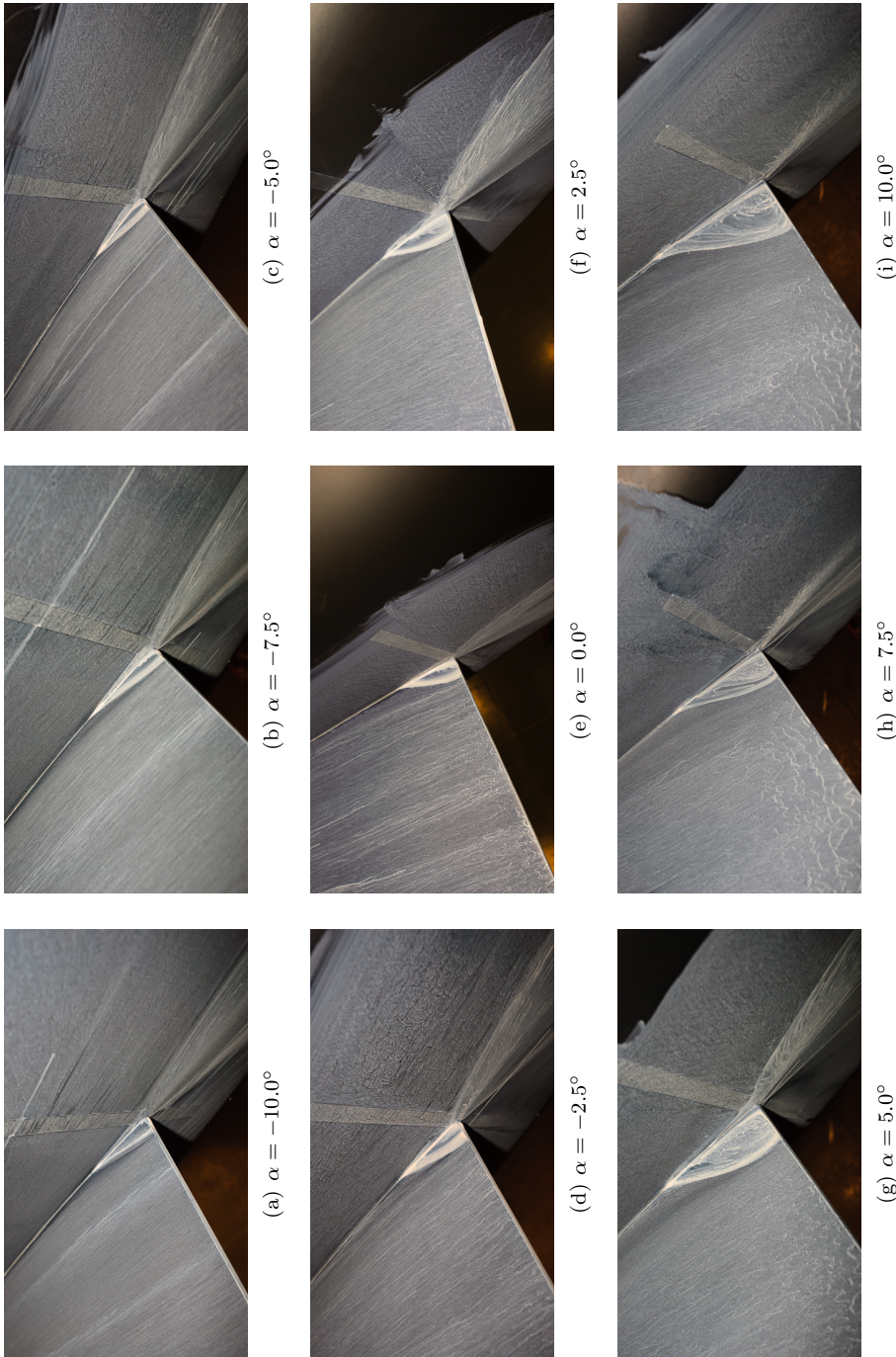


Figure 14. Oil-flow visualizations in the trailing-edge corner region of the F6 wing (port side) versus model angle of attack. F6 wing geometry (configuration 1) at $Re_c = 2.4$ million.

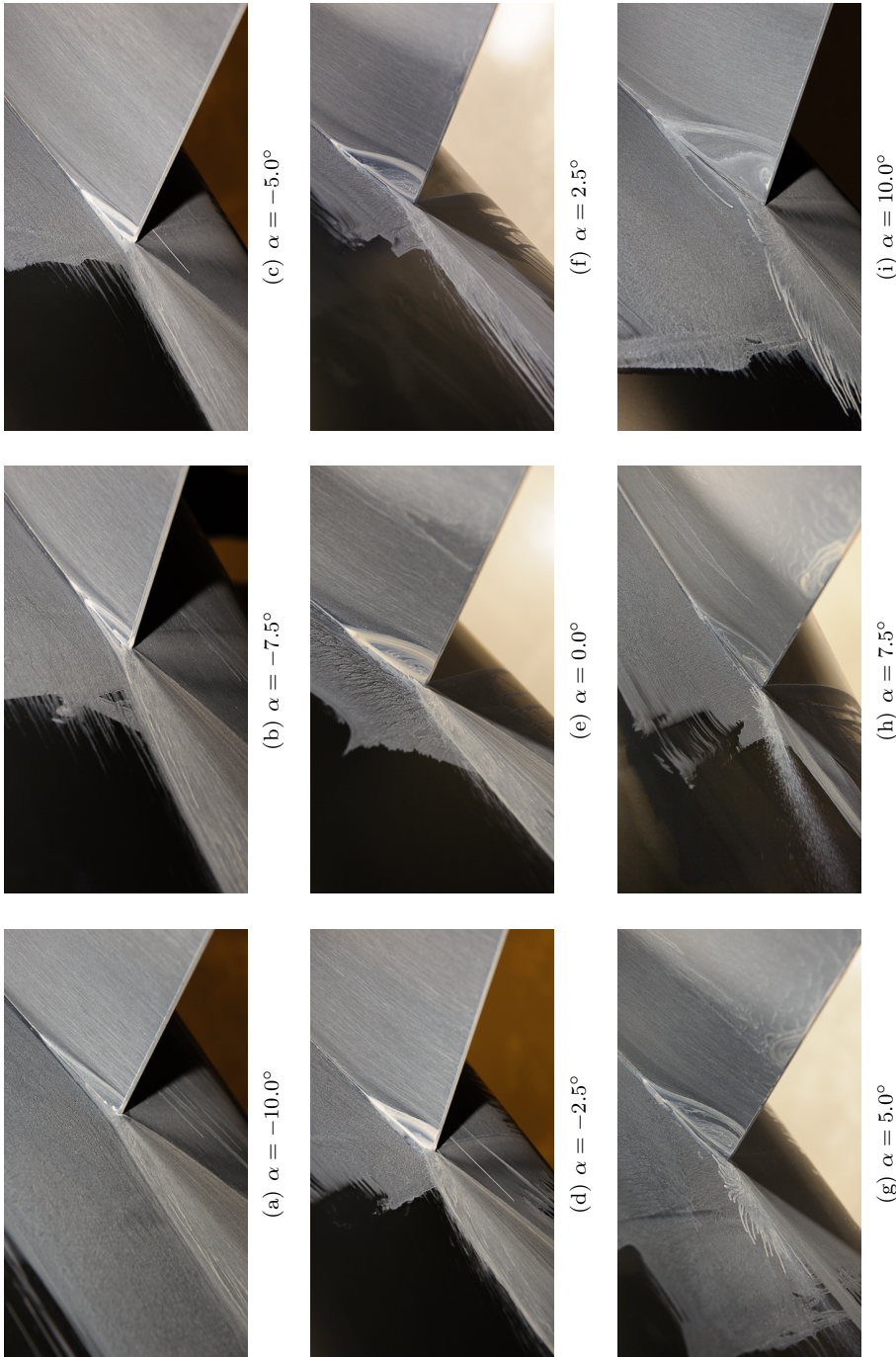


Figure 15. Oil-flow visualizations in the trailing-edge corner region of the F6 wing with leading-edge horn (starboard side) versus model angle of attack. F6 wing geometry (configuration 1) at $Re_c = 2.4$ million.

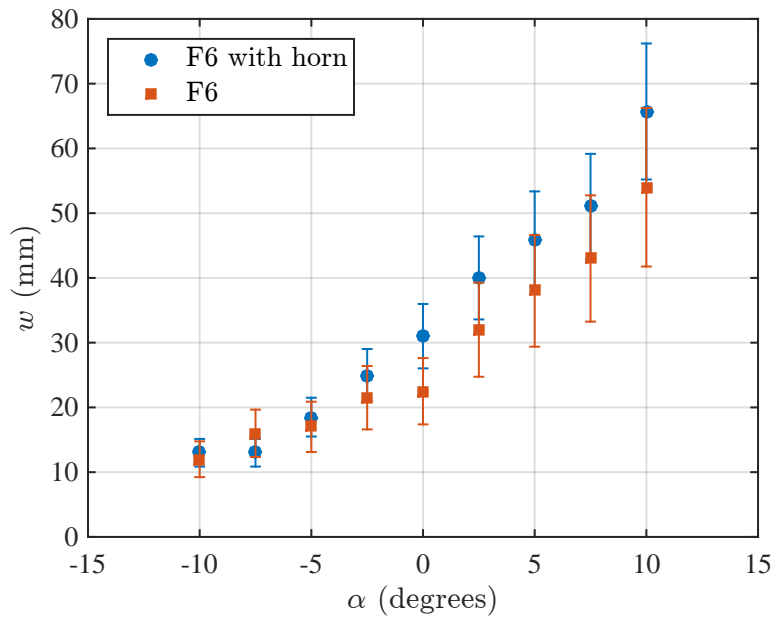


Figure 16. Corner-flow separation width versus model angle of attack for the F6 wing and the F6 wing with leading-edge horn (configuration 1). $Re_c = 2.4$ million.

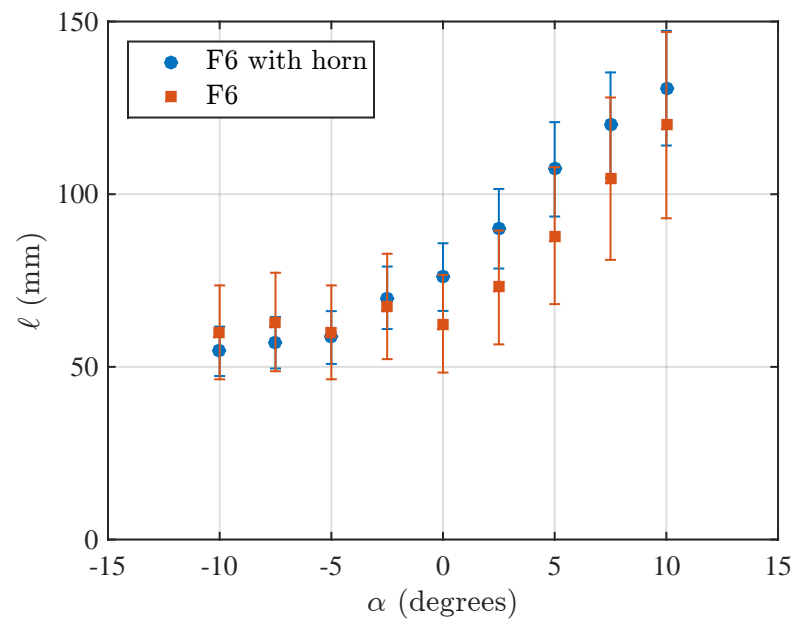


Figure 17. Corner-flow separation length versus model angle of attack for the F6 wing and the F6 wing with leading-edge horn (configuration 1). $Re_c = 2.4$ million.



Figure 18. Oil-flow visualizations at the leading edge of the F6 wing (port side) versus model angle of attack. F6 wing geometry (configuration 1) at $Re_c = 2.4$ million.

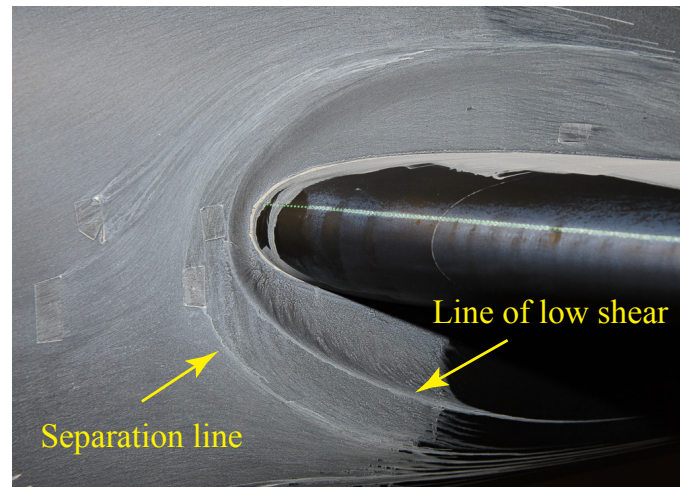


Figure 19. Oil-flow visualization in the leading-edge region of the F6 wing at $\alpha = 5^\circ$ and $Re_c = 2.4$ million.



Figure 20. Close-up image of the oil-flow visualization in the leading-edge region of the F6 wing at $\alpha = 5^\circ$ and $Re_c = 2.4$ million.

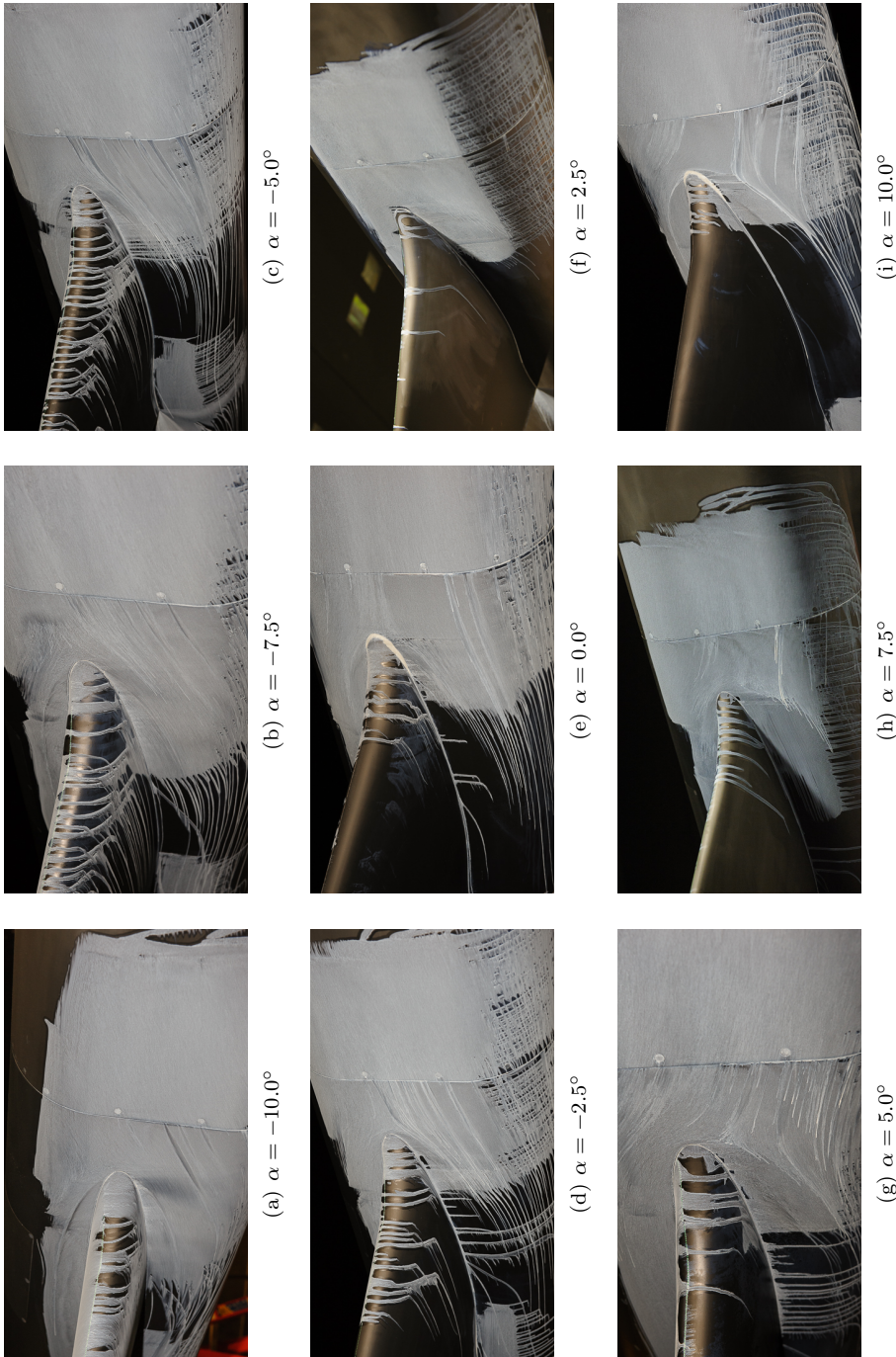


Figure 21. Oil-flow visualizations at the leading edge of the F6 wing with leading-edge horn (starboard side) versus model angle of attack. F6 wing geometry (configuration 1) at $Re_c = 2.4$ million.

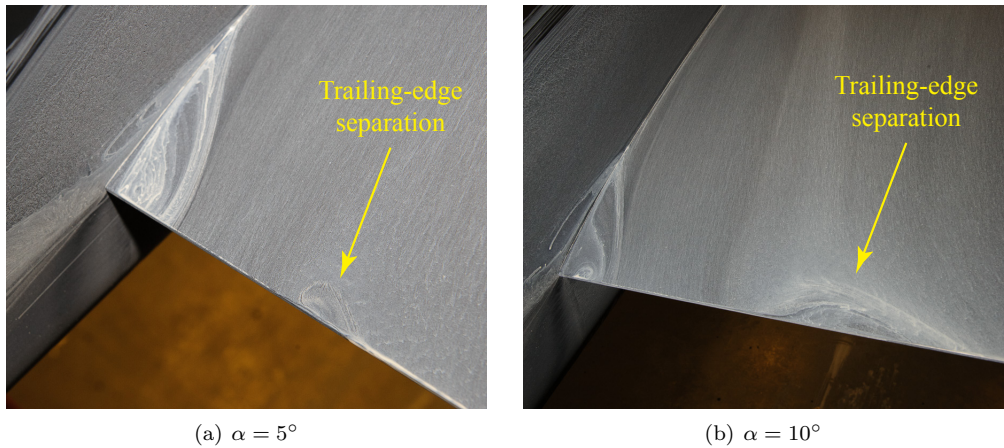


Figure 22. Oil-flow visualizations of the trailing-edge separation induced by a flow structure emanating from the F6 leading-edge horn. $Re_c = 2.4$ million.

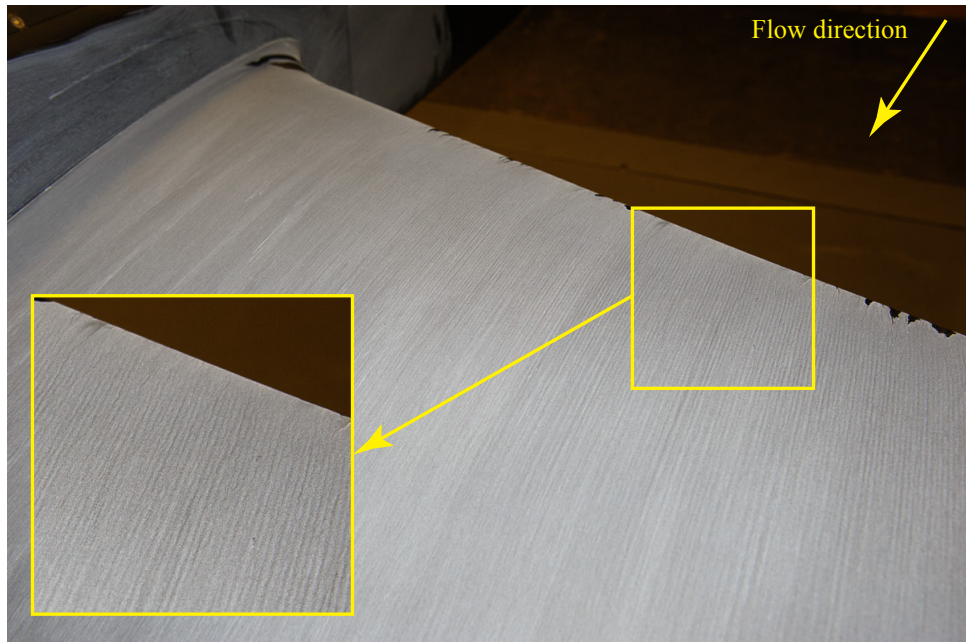


Figure 23. Oil-flow visualization showing the footprint of the vortical structures associated with trip dots that are not fully effective. F6 wing with leading-edge horn at $\alpha = -7.5^\circ$ and $Re_c = 2.4$ million.



(a) Oil-flow visualization in the Virginia Tech Stability Tunnel at $Re_c = 0.62$ million.



(b) Oil-flow visualization in the 14x22 Subsonic Wind Tunnel at $Re_c = 2.4$ million.

Figure 24. Effect of Reynolds number on the surface-flow topology of the F6 wing (port side) and the F6 wing with leading-edge horn (starboard side). Configuration 1 at $\alpha = 5^\circ$.

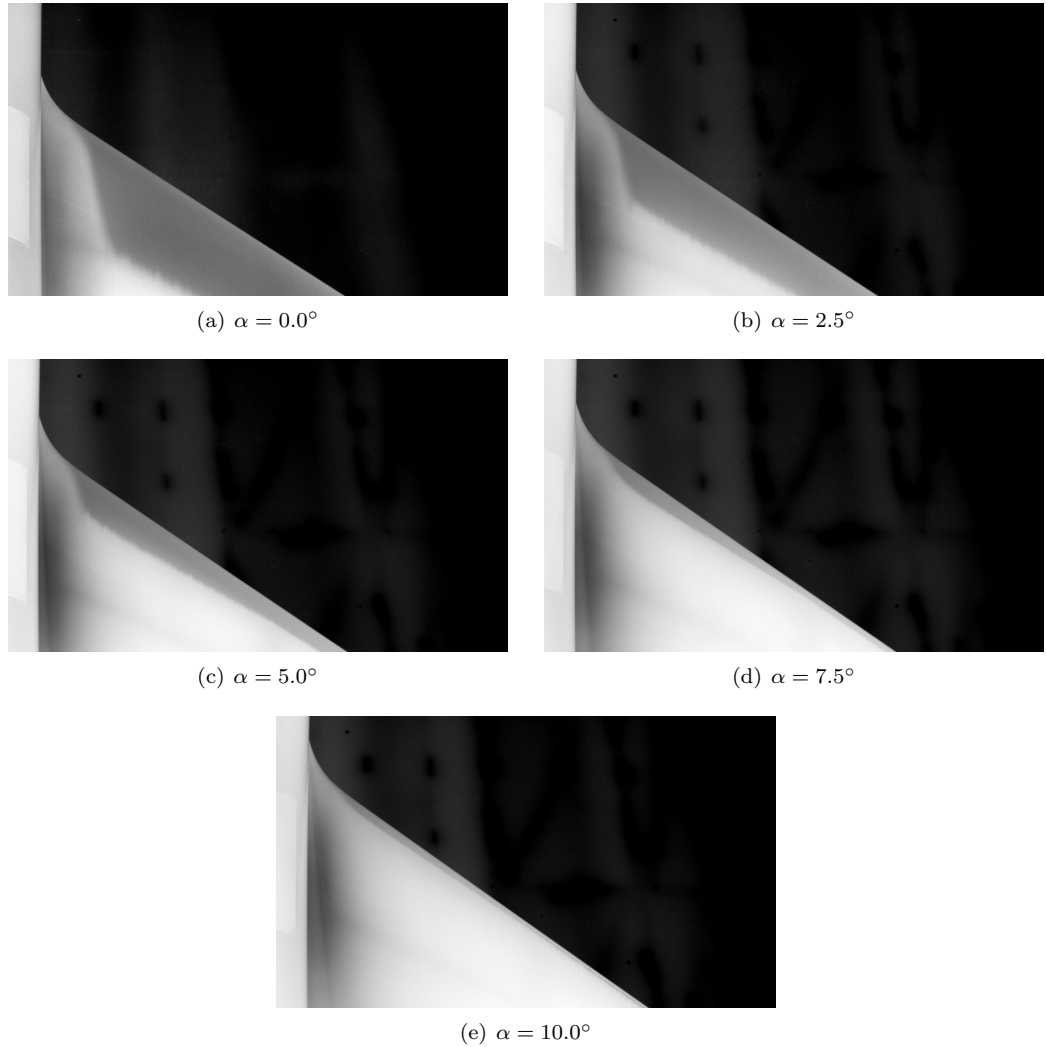


Figure 25. Infrared images of the NACA 0015mod wing (starboard side) versus model angle of attack. The wing surface was clean (no trip elements) and the fuselage boundary layer was tripped. Configuration 2 at $Re_c = 2.4$ million.

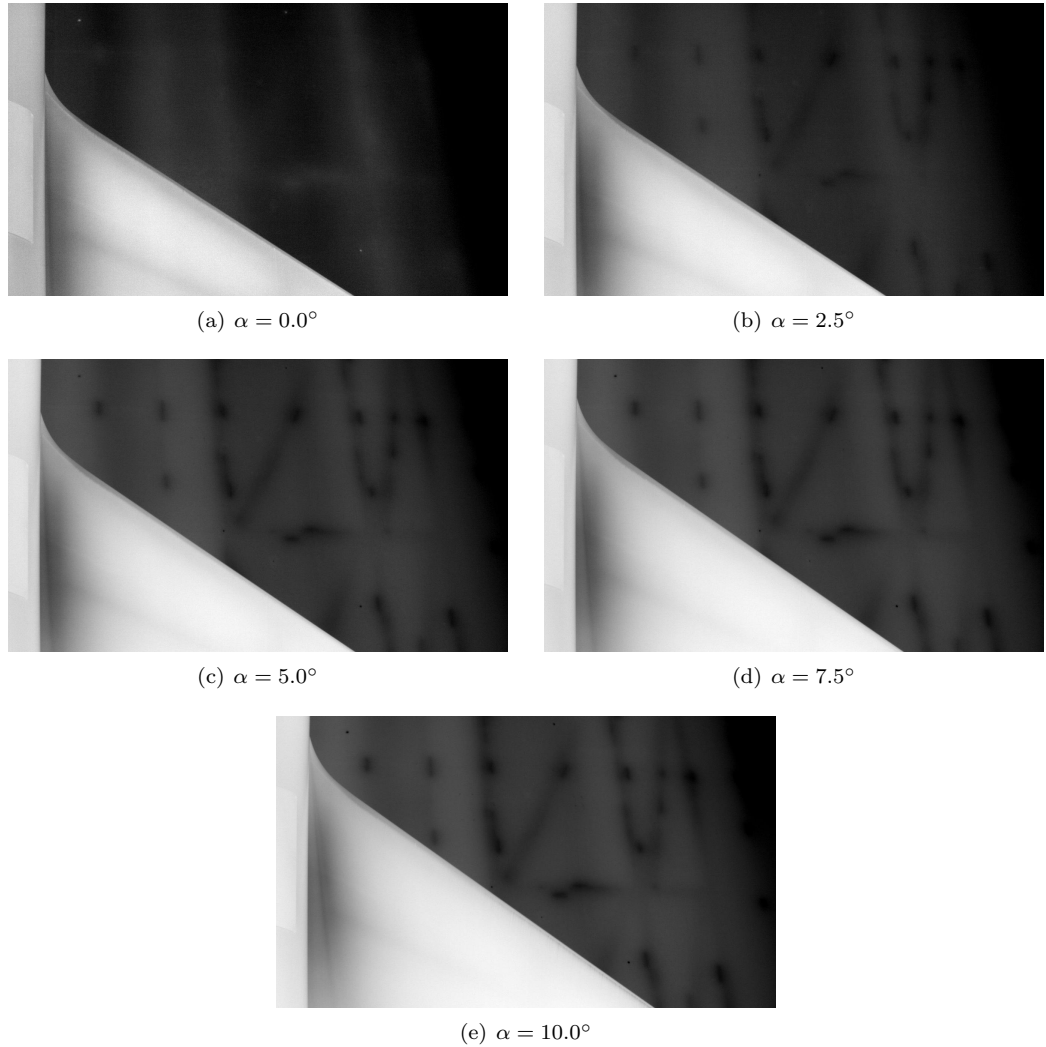


Figure 26. Infrared images of the NACA 0015mod wing (starboard side) versus model angle of attack. The wing surface was tripped at 6.4% chord with $142.2 \mu\text{m}$ trip dots and the fuselage boundary layer was tripped. Configuration 2 at $Re_c = 2.4$ million.

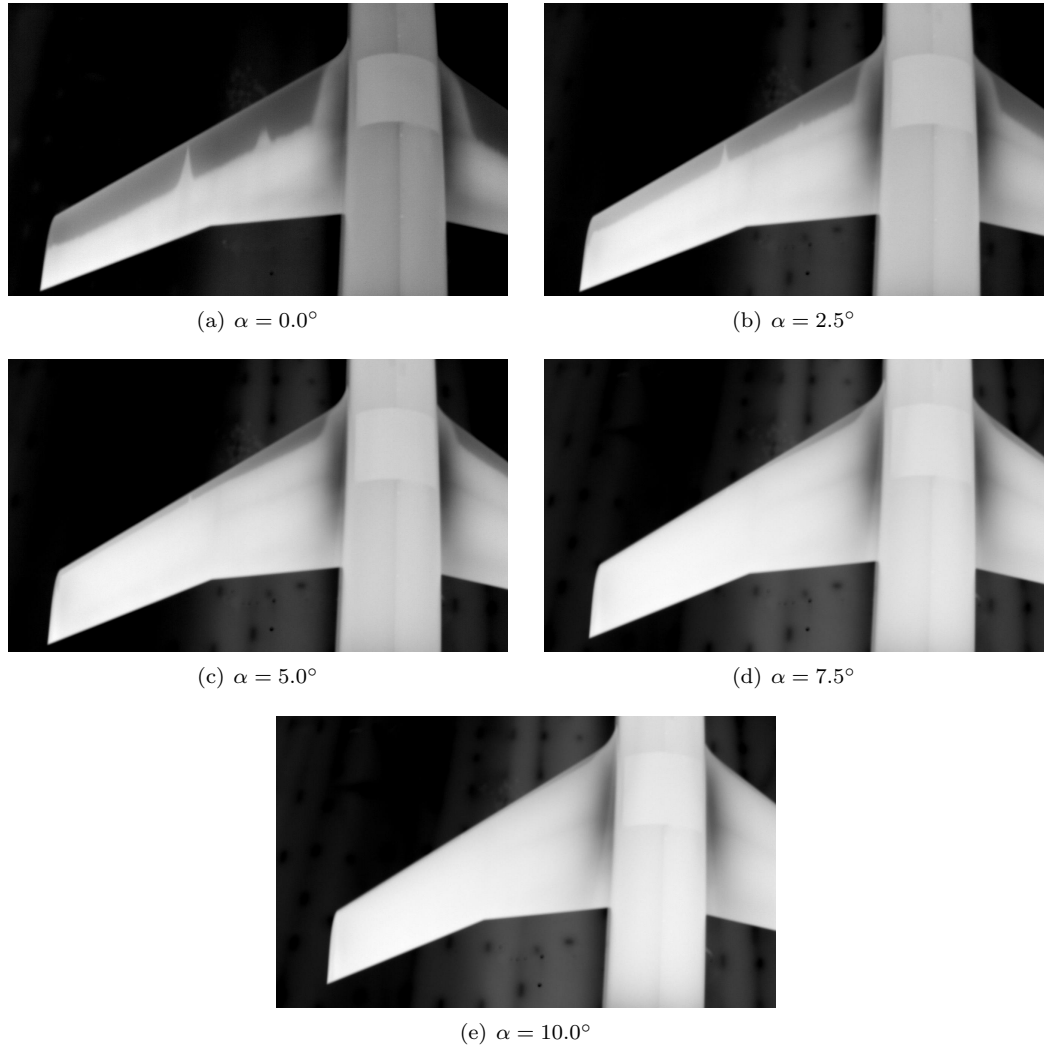


Figure 27. Infrared images of the NACA 0015 wing (port side) versus model angle of attack. The wing surface was clean (no trip elements) and the fuselage boundary layer was tripped. Configuration 2 at $Re_c = 2.4$ million.

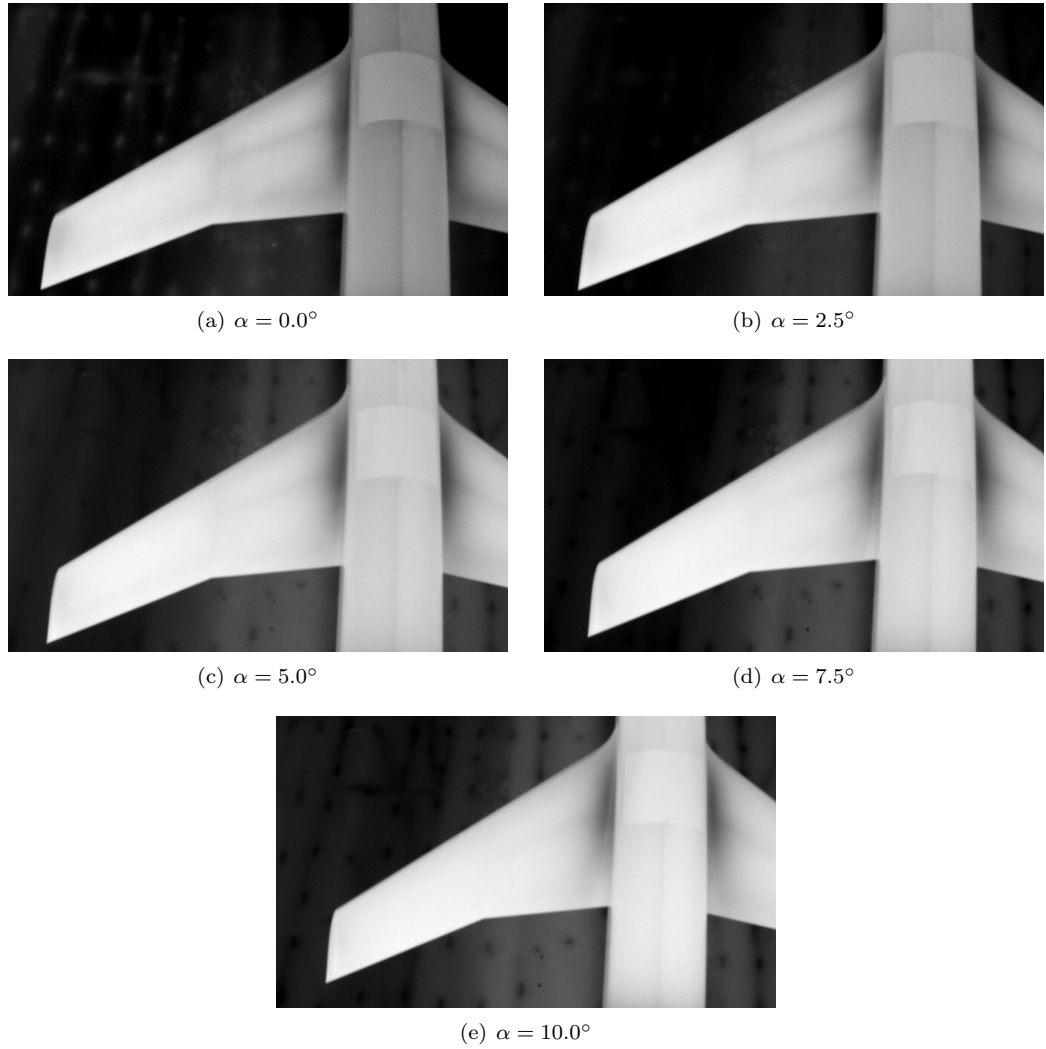


Figure 28. Infrared images of the NACA 0015 wing (port side) versus model angle of attack. The wing surface was tripped at 6.4% chord with $142.2 \mu\text{m}$ trip dots and the fuselage boundary layer was tripped. Configuration 2 at $Re_c = 2.4$ million.



(a) $\alpha = 2.5^\circ$



(b) $\alpha = 5.0^\circ$



(c) $\alpha = 10.0^\circ$

Figure 29. Planform view of the oil-flow visualization for configuration 2 versus model angle of attack. The NACA 0015 wing is on the port side and the NACA 0015mod wing is on the starboard side. $Re_c = 2.4$ million.

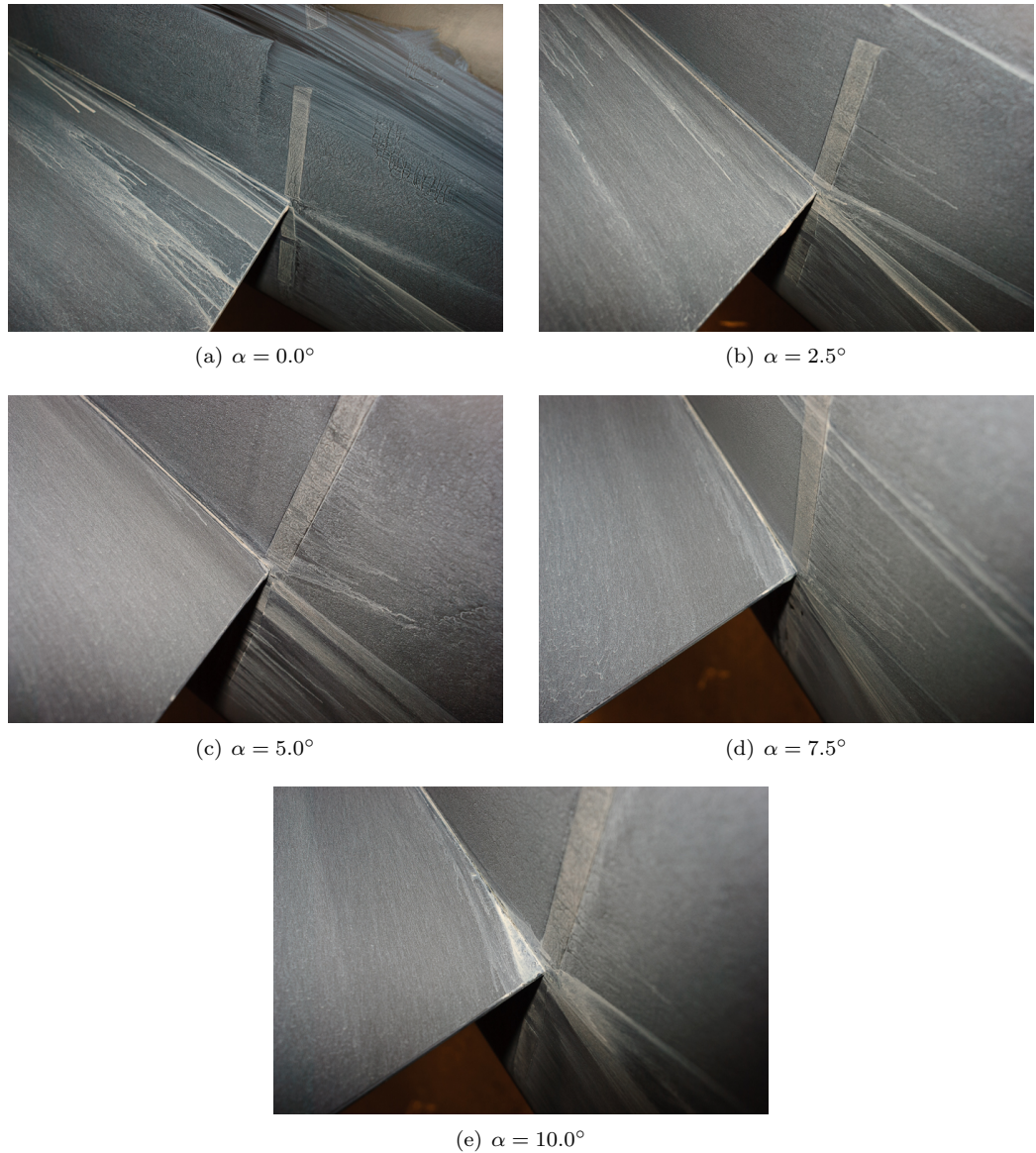


Figure 30. Oil-flow visualizations in the trailing-edge corner region of the NACA 0015 wing (port side) versus model angle of attack. Configuration 2 at $Re_c = 2.4$ million.

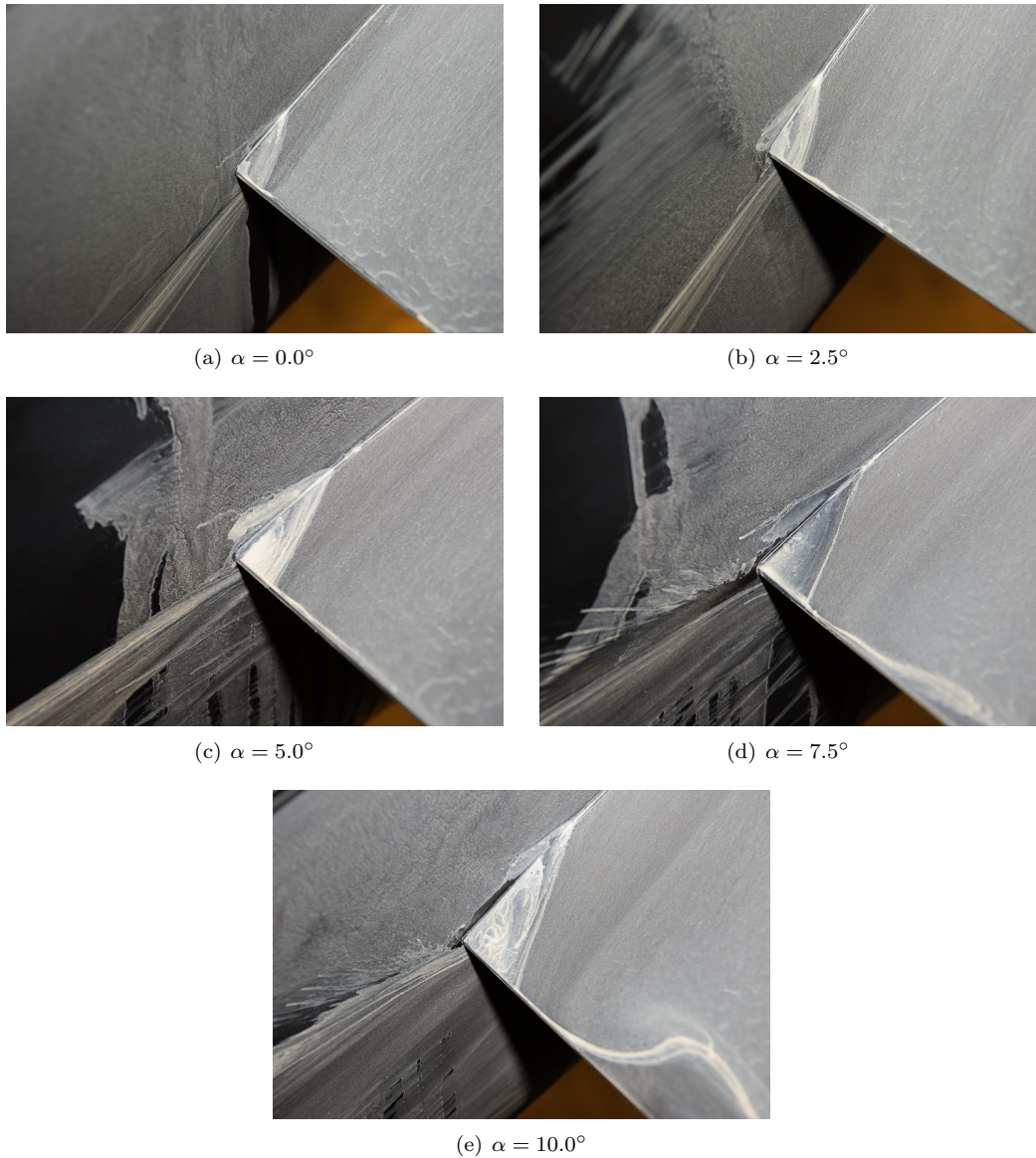


Figure 31. Oil-flow visualizations in the trailing-edge corner region of the NACA 0015mod wing (starboard side) versus model angle of attack. Configuration 2 at $Re_c = 2.4$ million.

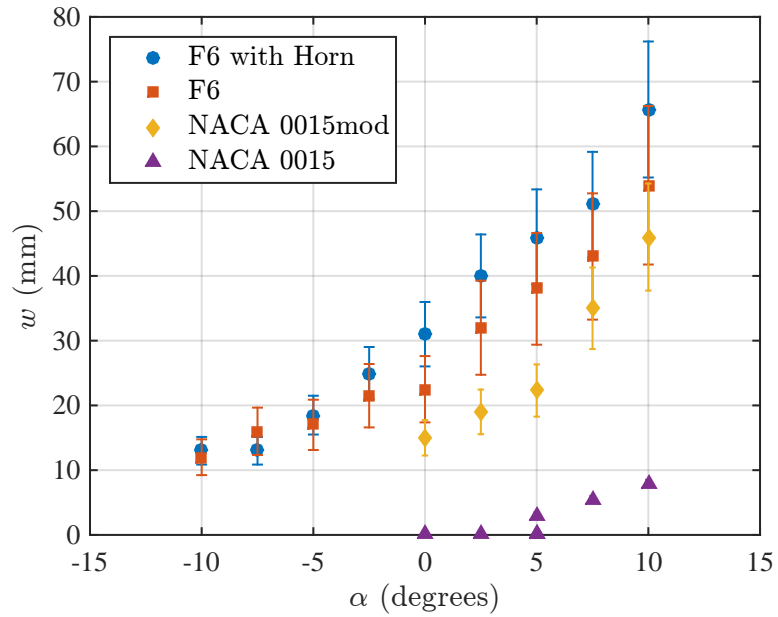


Figure 32. Corner-flow separation width versus model angle of attack for the F6 wings (configuration 1) and the NACA 0015 wings (configuration 2). $Re_c = 2.4$ million.

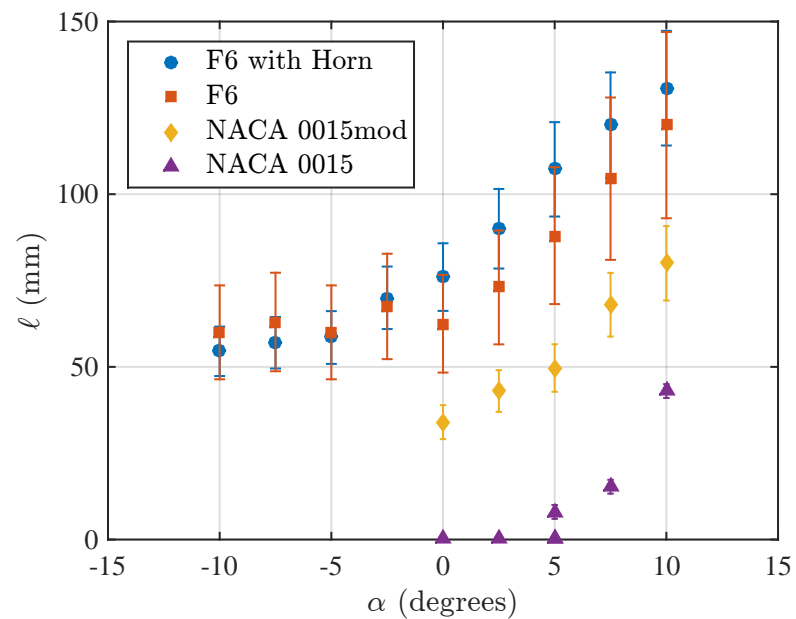


Figure 33. Corner-flow separation length versus model angle of attack for the F6 wings (configuration 1) and the NACA 0015 wings (configuration 2). $Re_c = 2.4$ million.



(a) Oil-flow visualization in the Virginia Tech Stability Tunnel at $Re_c = 0.62$ million.



(b) Oil-flow visualization in the 14x22 Subsonic Wind Tunnel at $Re_c = 2.4$ million.

Figure 34. Effect of Reynolds number on the surface-flow topology of the NACA 0015 wing (port side) and the NACA 0015mod wing (starboard side). Configuration 2 at $\alpha = 10^\circ$.

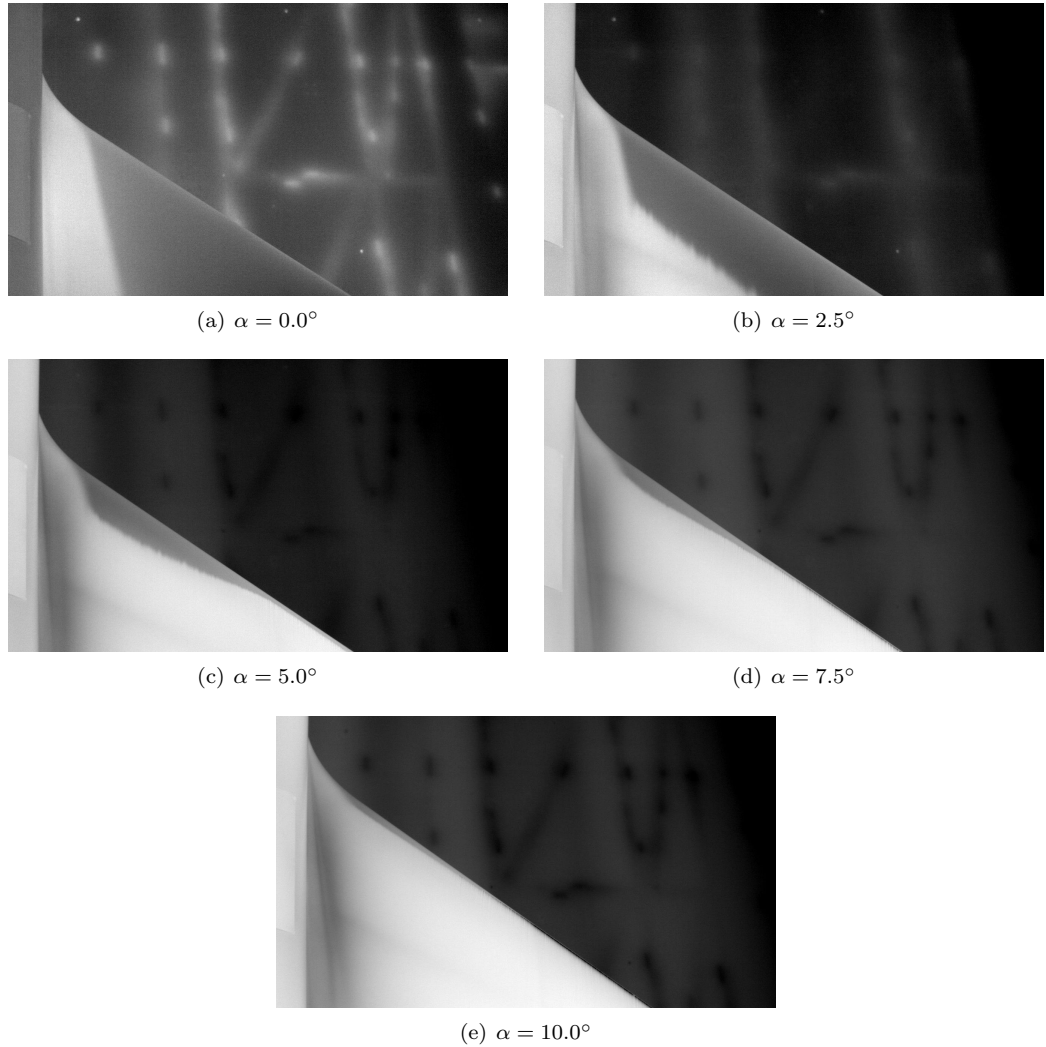


Figure 35. Infrared images of the COCA wing (starboard side) versus model angle of attack. The wing surface was clean (no trip elements) and the fuselage boundary layer was tripped. Configuration 3 at $Re_c = 2.4$ million.

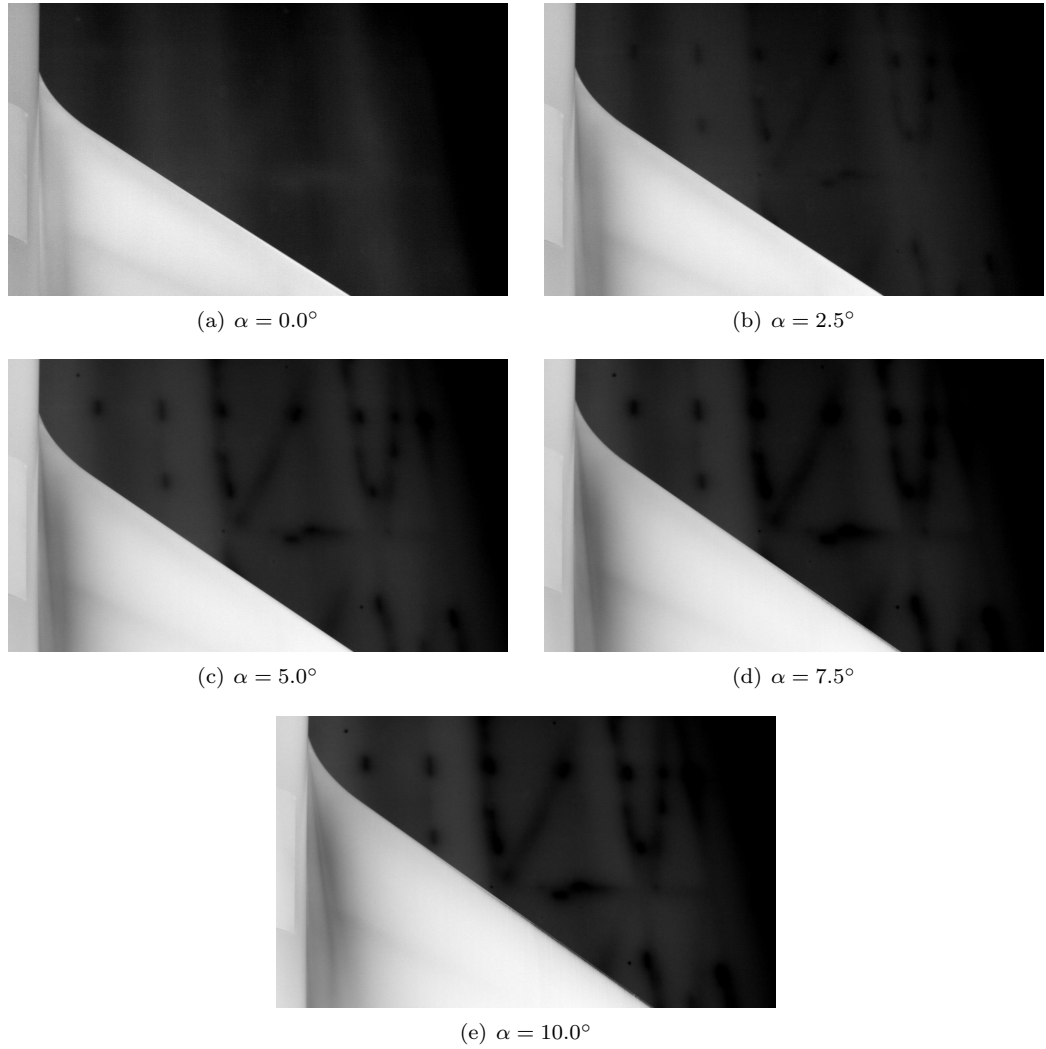


Figure 36. Infrared images of the COCA wing (starboard side) versus model angle of attack. The wing surface was tripped at 1.6% chord with $182.9 \mu\text{m}$ trip dots and the fuselage boundary layer was tripped. Configuration 3 at $Re_c = 2.4$ million.

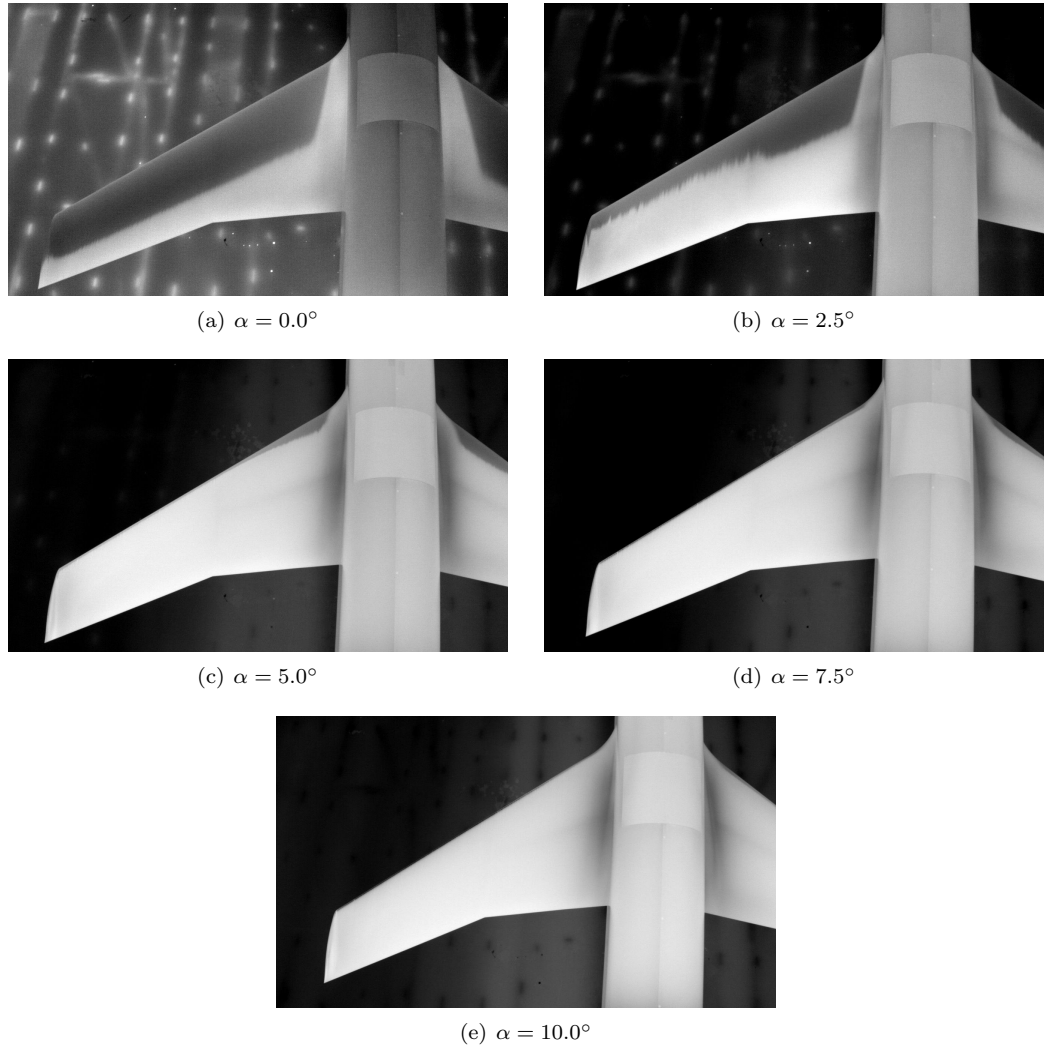


Figure 37. Infrared images of the F6 S12 wing (port side) versus model angle of attack. The wing surface was clean (no trip elements) and the fuselage boundary layer was tripped. Configuration 3 at $Re_c = 2.4$ million.

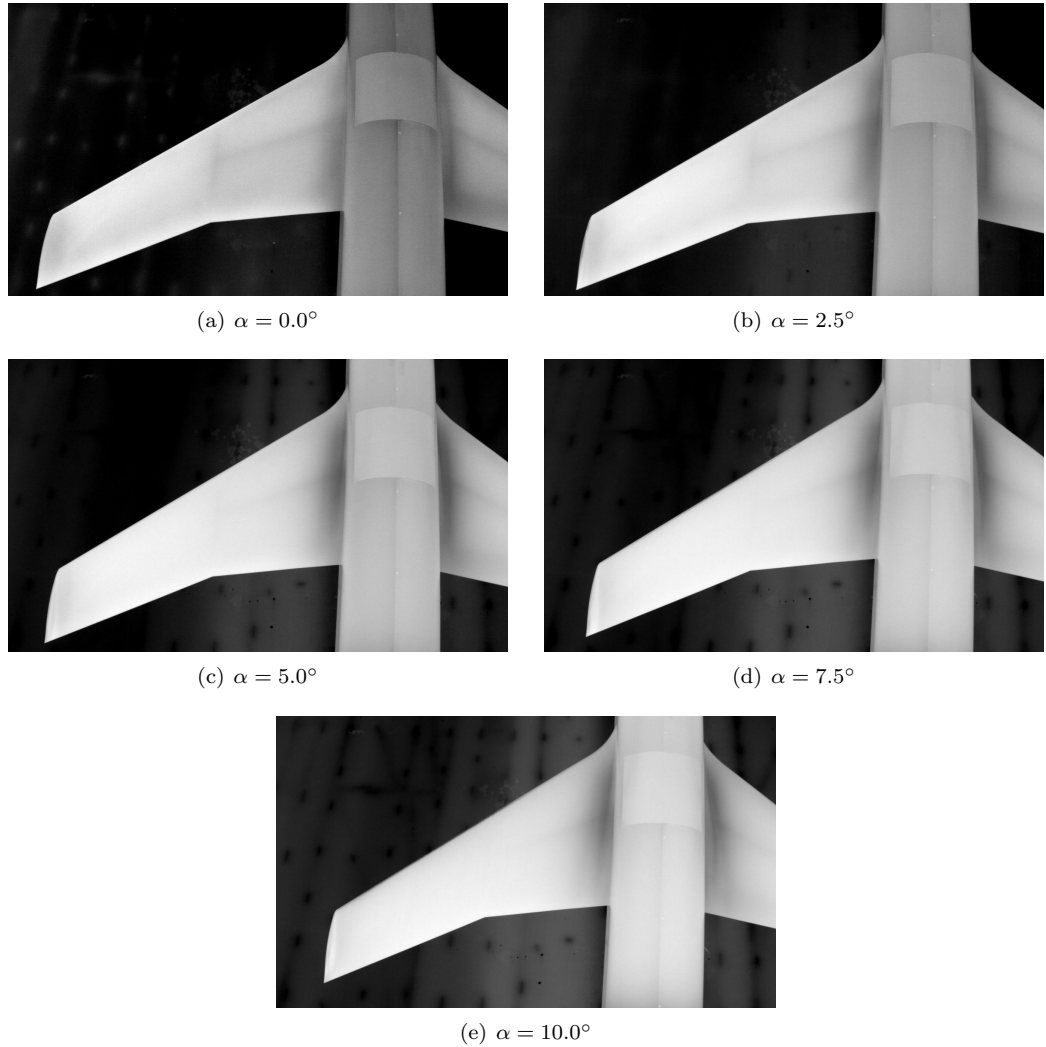


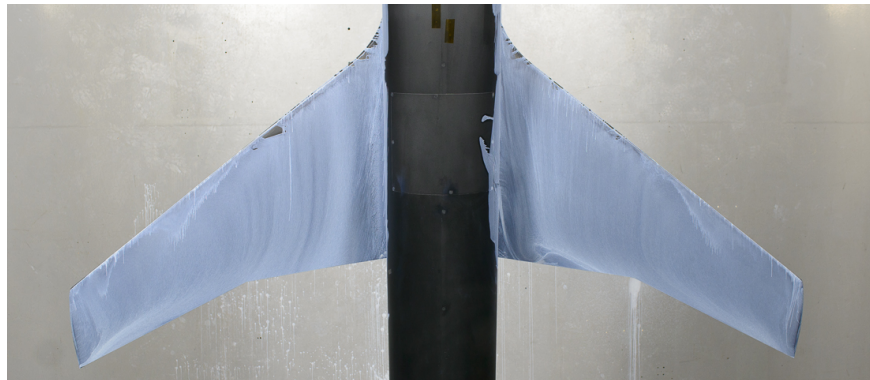
Figure 38. Infrared images of the F6 S12 wing (port side) versus model angle of attack. The wing surface was tripped at 1.6% chord with $182.9 \mu\text{m}$ trip dots and the fuselage boundary layer was tripped. Configuration 3 at $Re_c = 2.4$ million.



(a) $\alpha = 0.0^\circ$



(b) $\alpha = 5.0^\circ$



(c) $\alpha = 10.0^\circ$

Figure 39. Planform view of the oil-flow visualization for configuration 3 versus model angle of attack. The F6 S12 wing is on the port side and the COCA wing is on the starboard side. $Re_c = 2.4$ million.

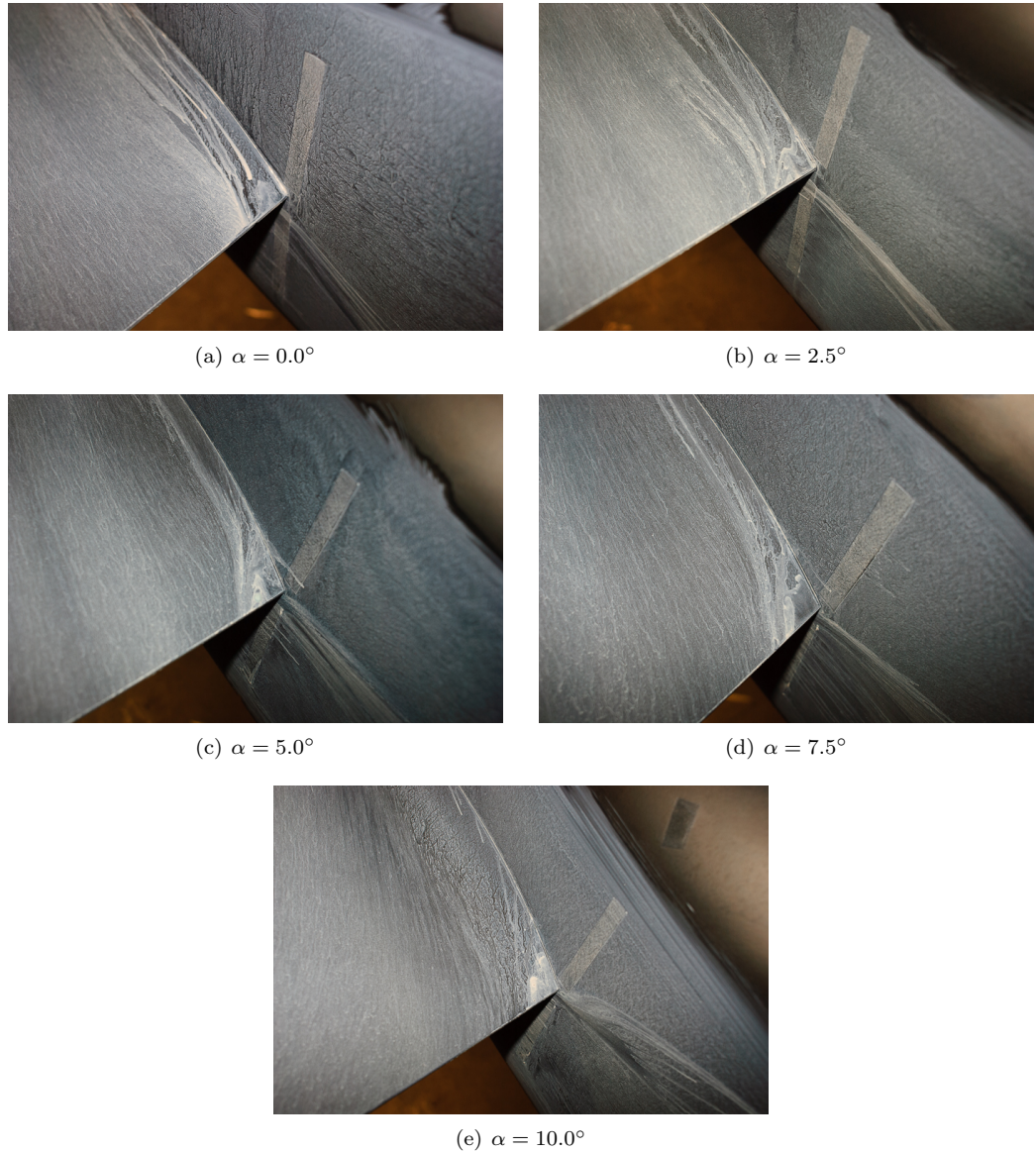


Figure 40. Oil-flow visualizations in the trailing-edge corner region of the F6 S12 wing (port side) versus model angle of attack. Configuration 3 at $Re_c = 2.4$ million.

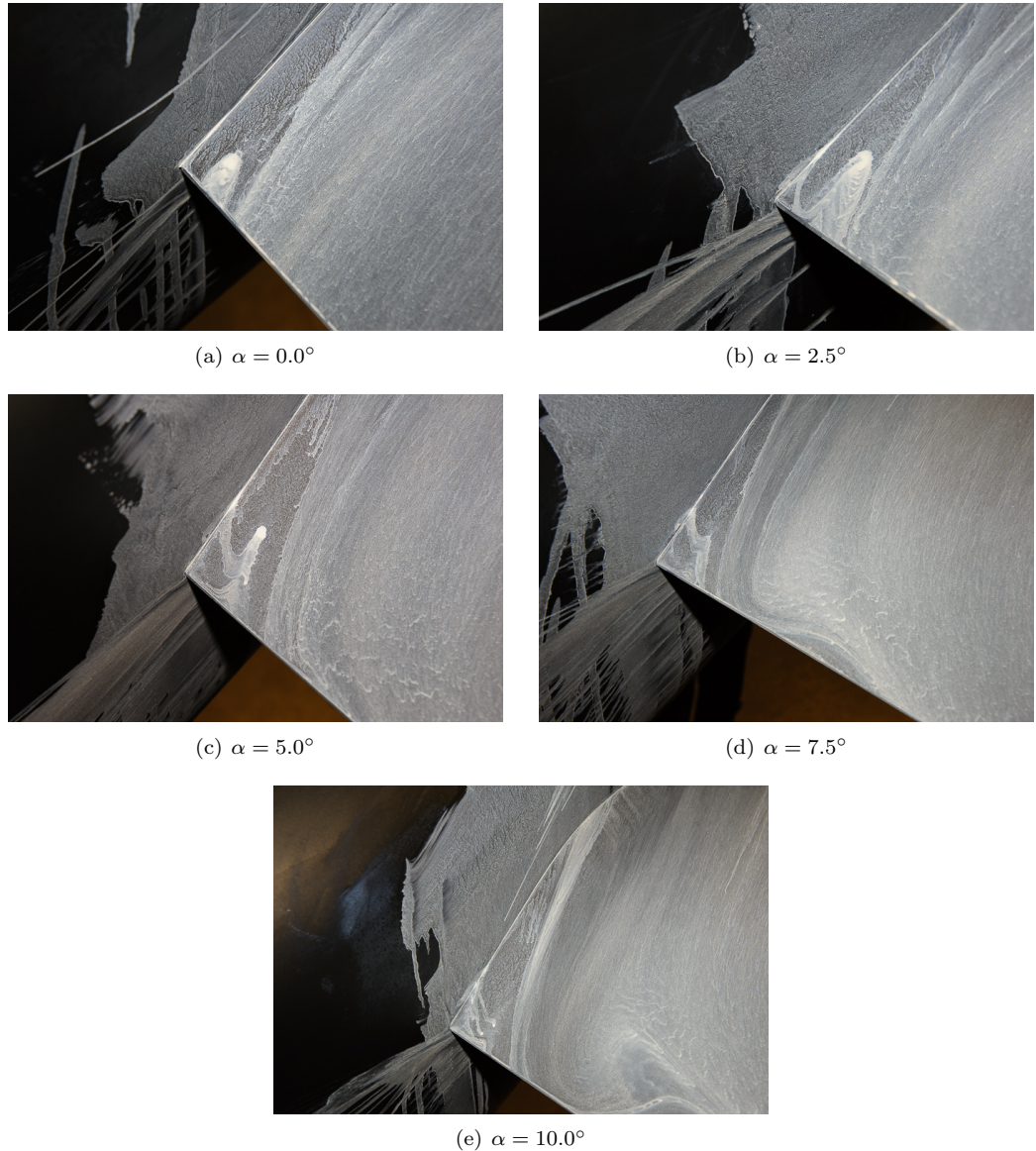


Figure 41. Oil-flow visualizations in the trailing-edge corner region of the COCA wing (port side) versus model angle of attack. Configuration 3 at $Re_c = 2.4$ million.



(a) $\alpha = -5.0^\circ$



(b) $\alpha = 0.0^\circ$



(c) $\alpha = 5.0^\circ$

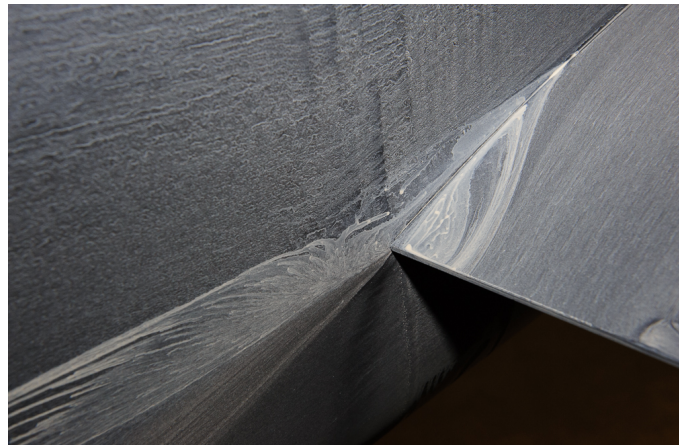


(d) $\alpha = 10.0^\circ$

Figure 42. Planform view of the oil-flow visualization for configuration 4 versus model angle of attack. Both F6 wings were configured with the leading-edge horn. $Re_c = 2.4$ million.



(a) Port side.



(b) Starboard side.

Figure 43. Oil-flow visualizations in the trailing-edge corner region of the F6 wings with leading-edge horn. Configuration 4 at $\alpha = 5^\circ$ and $Re_c = 2.4$ million.

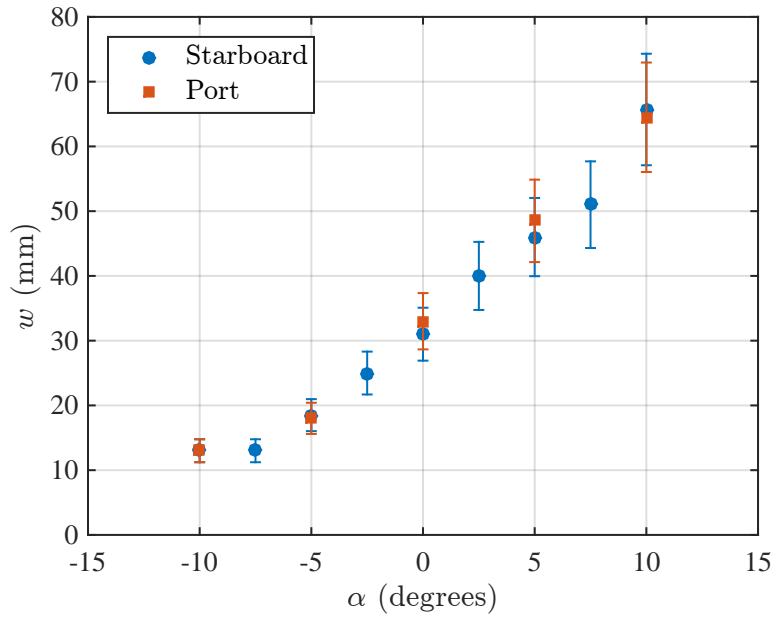


Figure 44. Corner-flow separation width versus model angle of attack for the F6 wings with leading-edge horn (configuration 4). $Re_c = 2.4$ million.

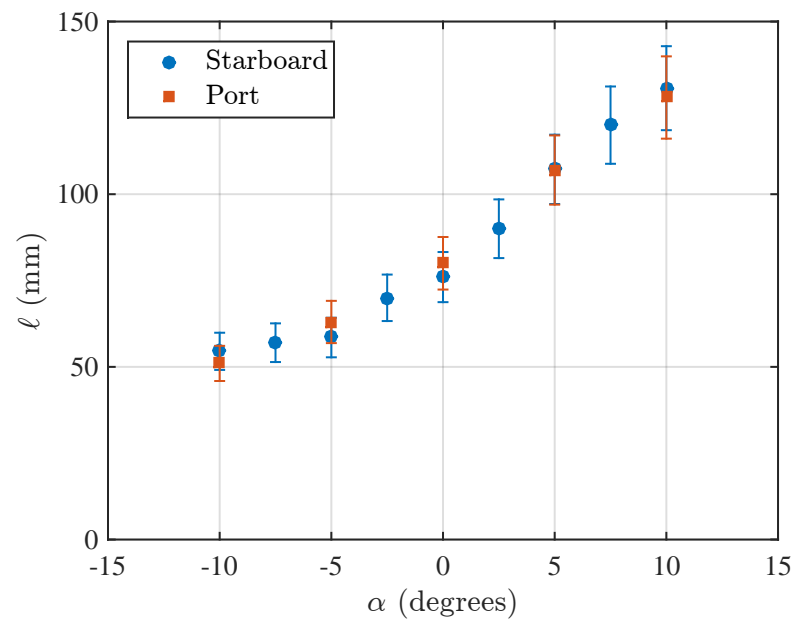


Figure 45. Corner-flow separation length versus model angle of attack for the F6 wings with leading-edge horn (configuration 4). $Re_c = 2.4$ million.

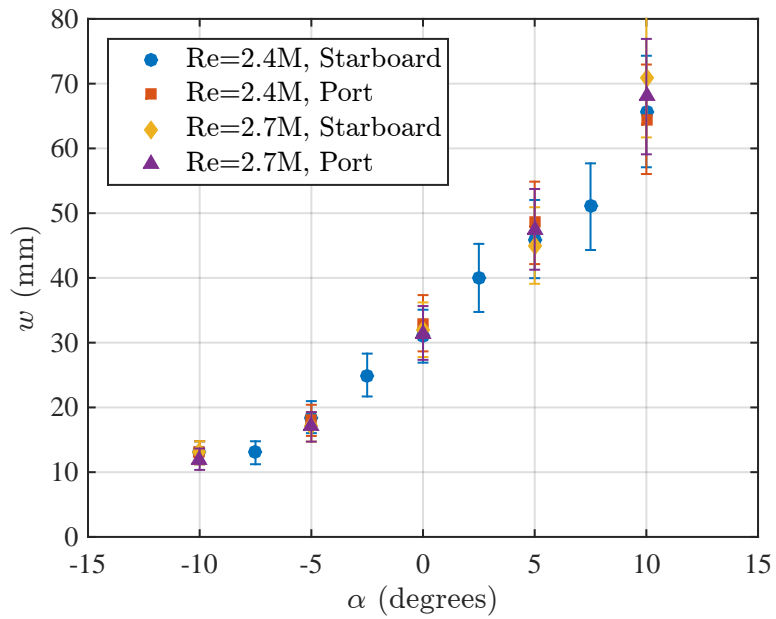


Figure 46. Effect of Reynolds number on the corner-flow separation width of the F6 wings with leading-edge horn (configuration 4).

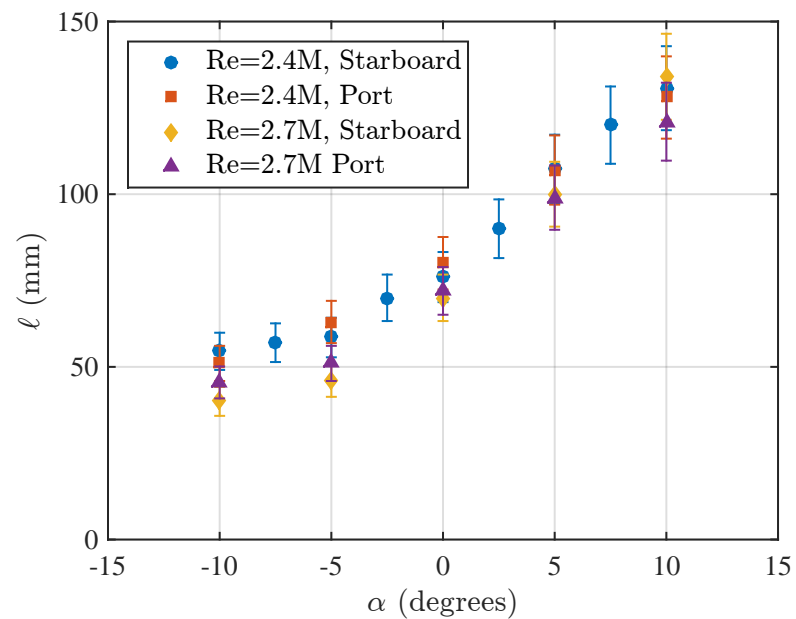


Figure 47. Effect of Reynolds number on the corner-flow separation length of the F6 wings with leading-edge horn (configuration 4).

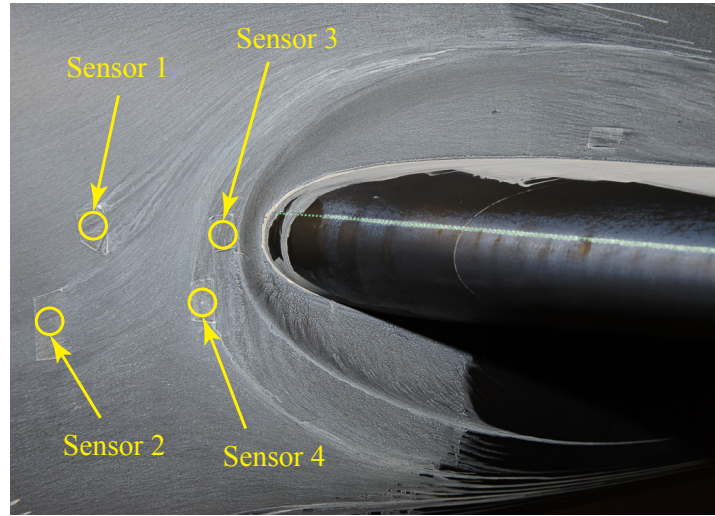


Figure 48. Pressure sensor locations in the the leading-edge region of the F6 wing. Oil-flow visualization at $\alpha = 5^\circ$ and $Re_c = 2.4$ million.

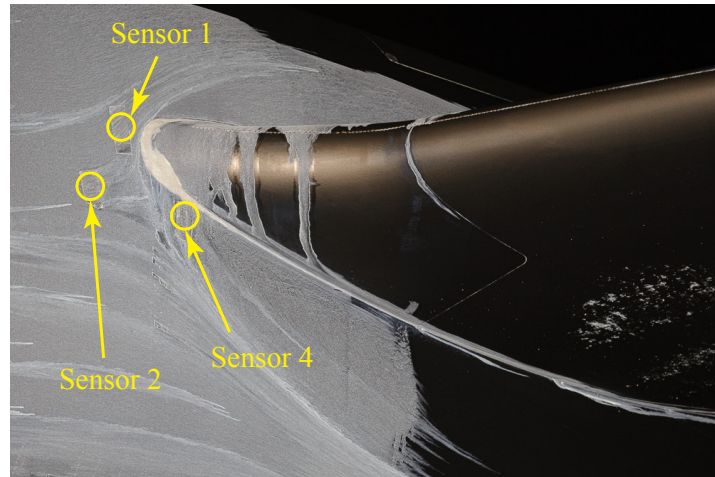


Figure 49. Pressure sensor locations in the the leading-edge region of the F6 wing with leading-edge horn. Oil-flow visualization at $\alpha = 5^\circ$ and $Re_c = 2.4$ million.

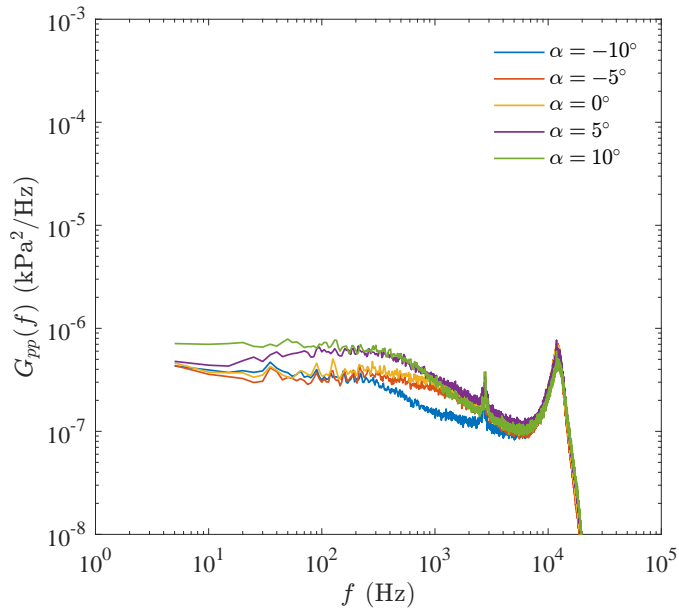


Figure 50. Auto spectral density of pressure sensor 1 versus angle of attack. F6 wing at $Re_c = 2.4$ million, with pressure sensor 2 as a reference for facility noise removal.

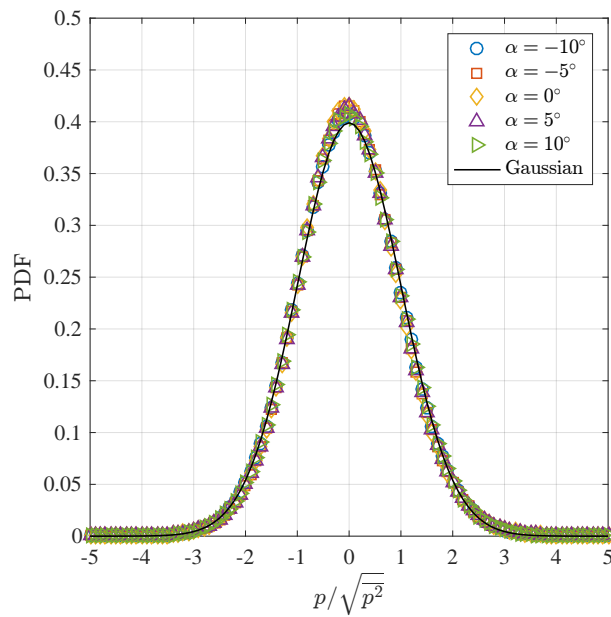


Figure 51. Probability density of pressure sensor 1 versus angle of attack. F6 wing at $Re_c = 2.4$ million, with pressure sensor 2 as a reference for facility noise removal.

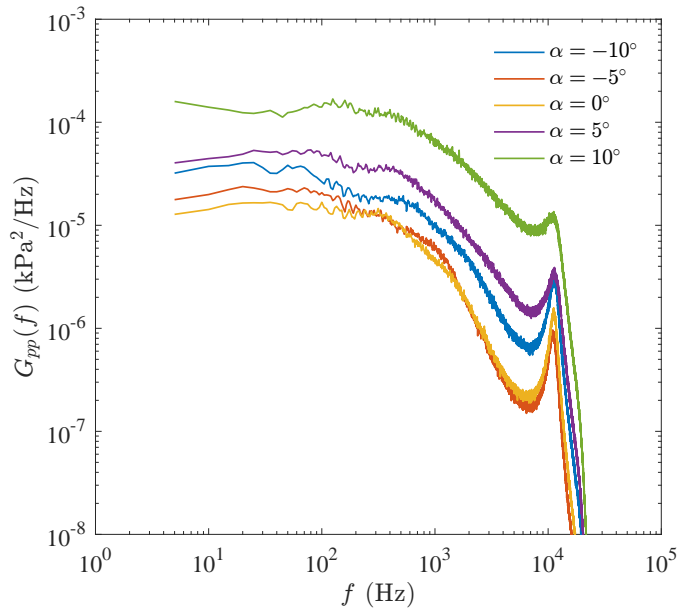


Figure 52. Auto spectral density of pressure sensor 3 versus angle of attack. F6 wing at $Re_c = 2.4$ million, with pressure sensor 2 as a reference for facility noise removal.

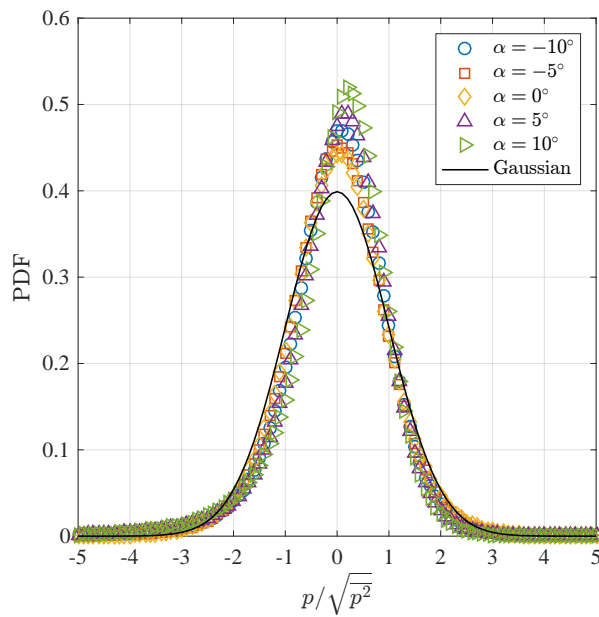


Figure 53. Probability density of pressure sensor 3 versus angle of attack. F6 wing at $Re_c = 2.4$ million, with pressure sensor 2 as a reference for facility noise removal.

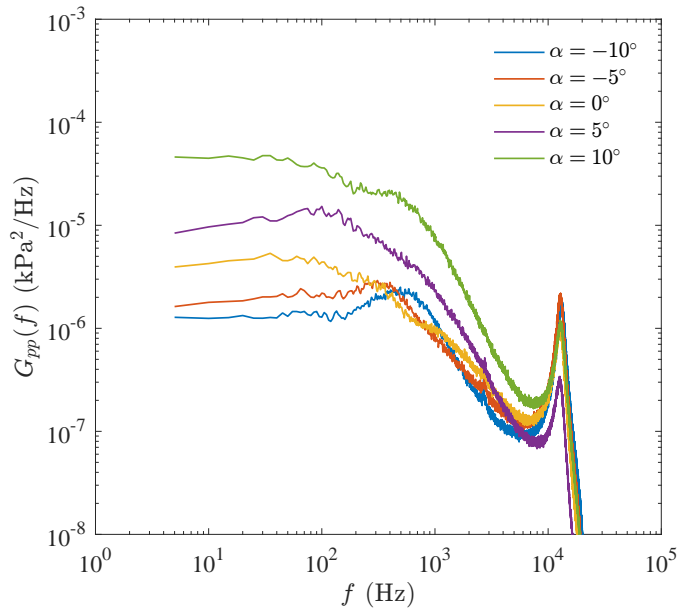


Figure 54. Auto spectral density of pressure sensor 4 versus angle of attack. F6 wing at $Re_c = 2.4$ million, with pressure sensor 2 as a reference for facility noise removal.

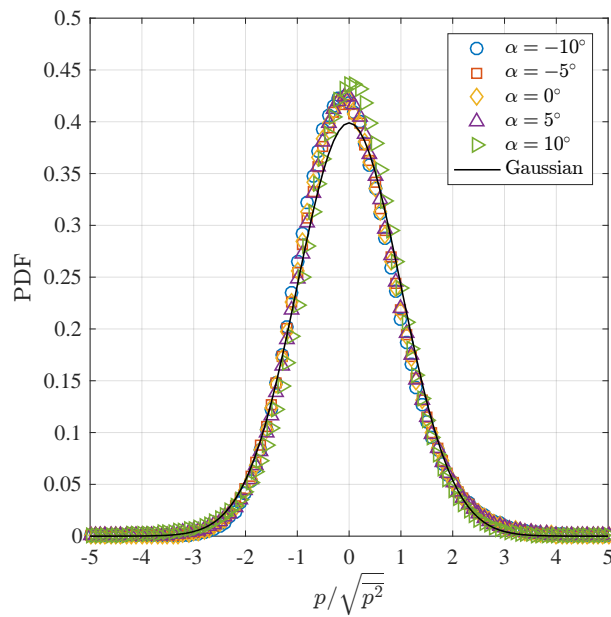


Figure 55. Probability density of pressure sensor 4 versus angle of attack. F6 wing at $Re_c = 2.4$ million, with pressure sensor 2 as a reference for facility noise removal.

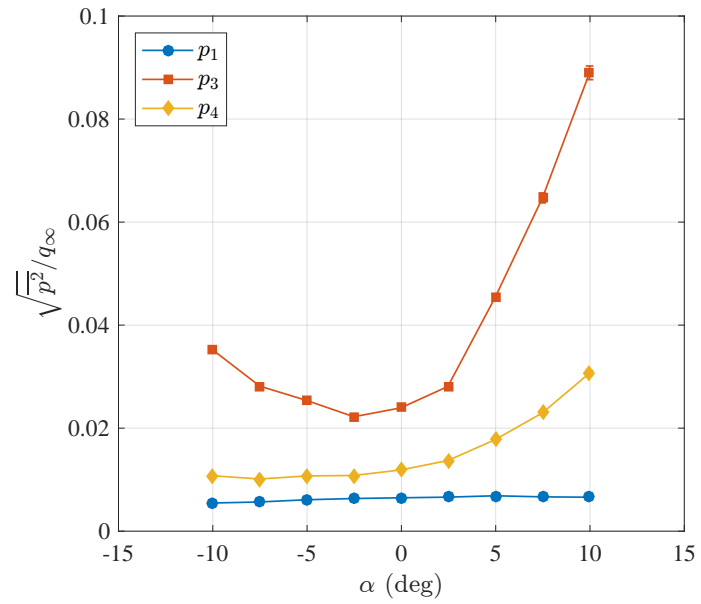


Figure 56. RMS for pressure sensors 1, 3, and 4 versus angle of attack. F6 wing at $Re_c = 2.4$ million, with pressure sensor 2 as a reference for facility noise removal.

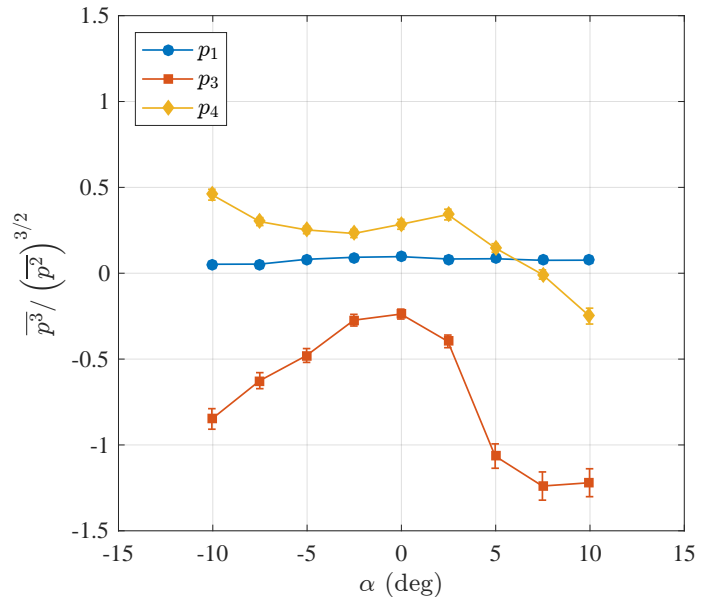


Figure 57. Skewness for pressure sensors 1, 3, and 4 versus angle of attack. F6 wing at $Re_c = 2.4$ million, with pressure sensor 2 as a reference for facility noise removal.

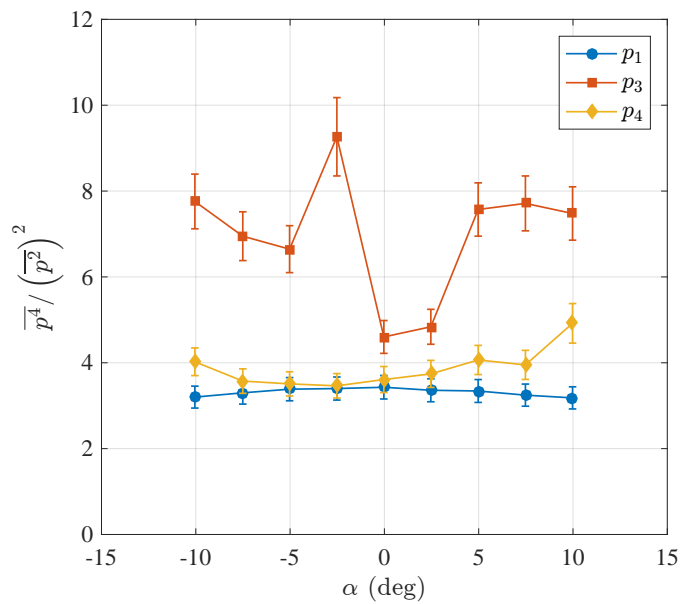


Figure 58. Flatness for pressure sensors 1, 3, and 4 versus angle of attack. F6 wing at $Re_c = 2.4$ million, with pressure sensor 2 as a reference for facility noise removal.

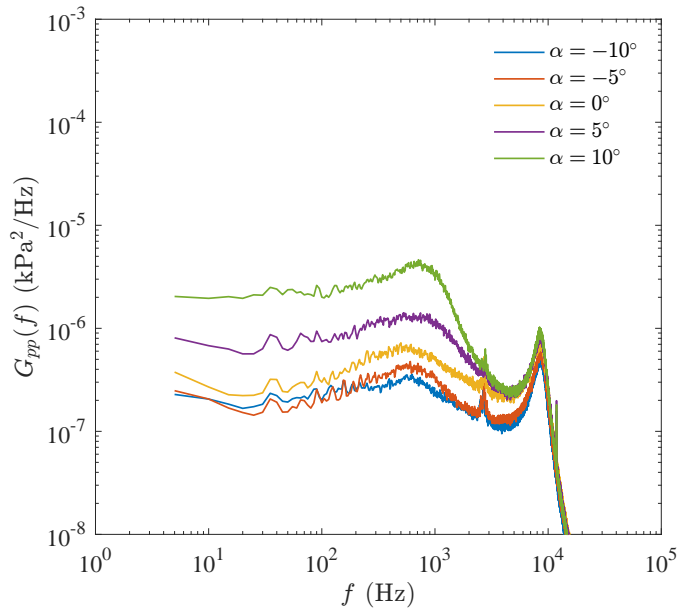


Figure 59. Auto spectral density of pressure sensor 7 versus angle of attack. F6 wing at $Re_c = 2.4$ million, with pressure sensor 6 as a reference for facility noise removal.

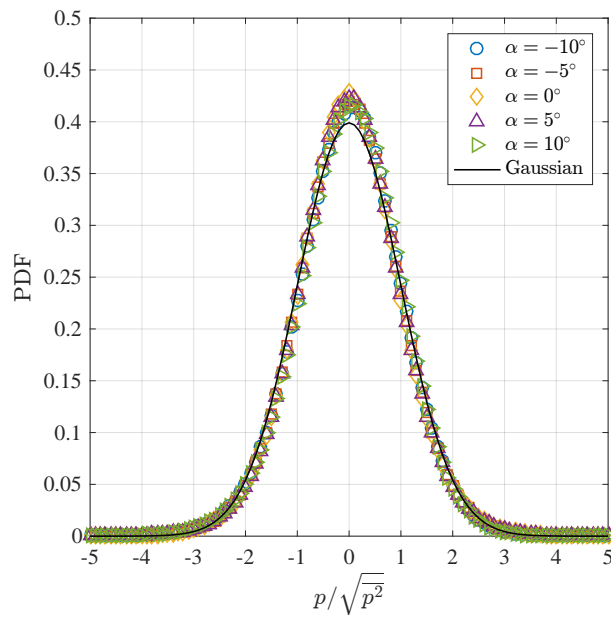


Figure 60. Probability density of pressure sensor 7 versus angle of attack. F6 wing at $Re_c = 2.4$ million, with pressure sensor 6 as a reference for facility noise removal.

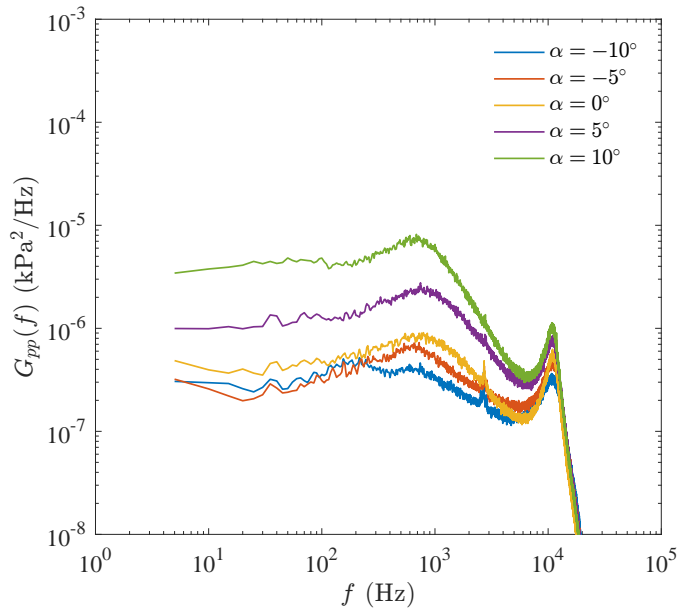


Figure 61. Auto spectral density of pressure sensor 8 versus angle of attack. F6 wing at $Re_c = 2.4$ million, with pressure sensor 6 as a reference for facility noise removal.

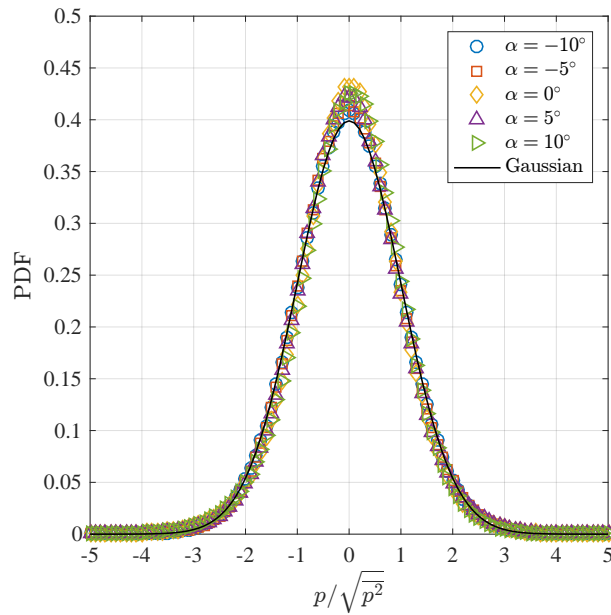


Figure 62. Probability density of pressure sensor 8 versus angle of attack. F6 wing at $Re_c = 2.4$ million, with pressure sensor 6 as a reference for facility noise removal.

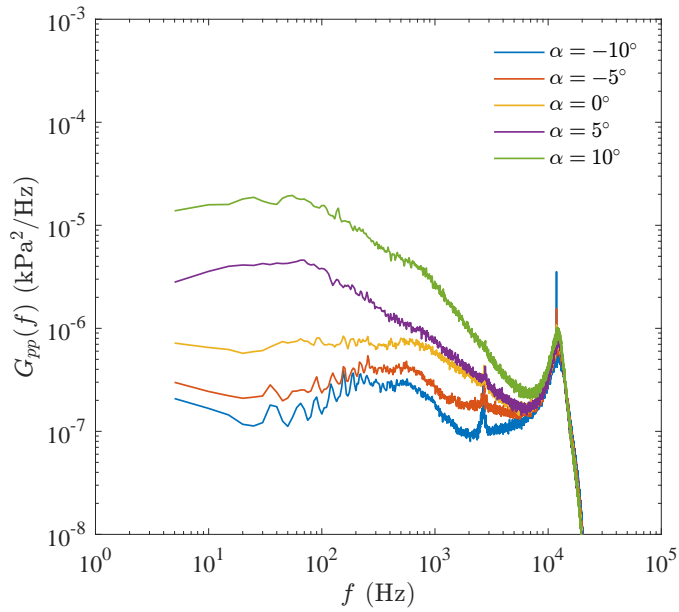


Figure 63. Auto spectral density of pressure sensor 9 versus angle of attack. F6 wing at $Re_c = 2.4$ million, with pressure sensor 6 as a reference for facility noise removal.

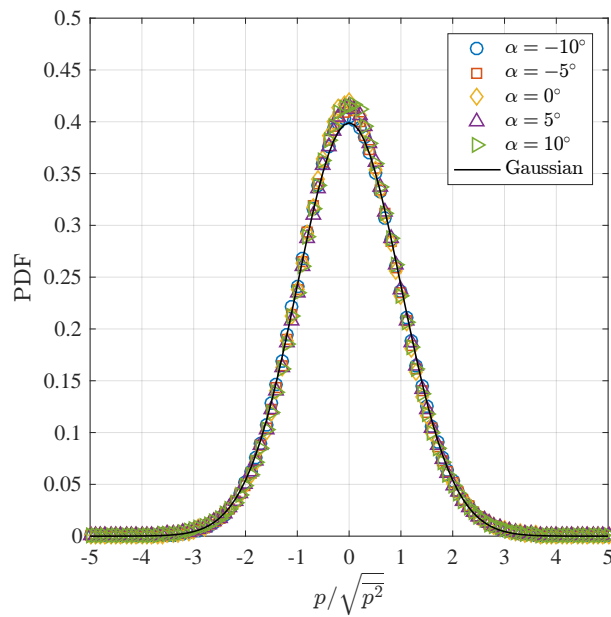


Figure 64. Probability density of pressure sensor 9 versus angle of attack. F6 wing at $Re_c = 2.4$ million, with pressure sensor 6 as a reference for facility noise removal.

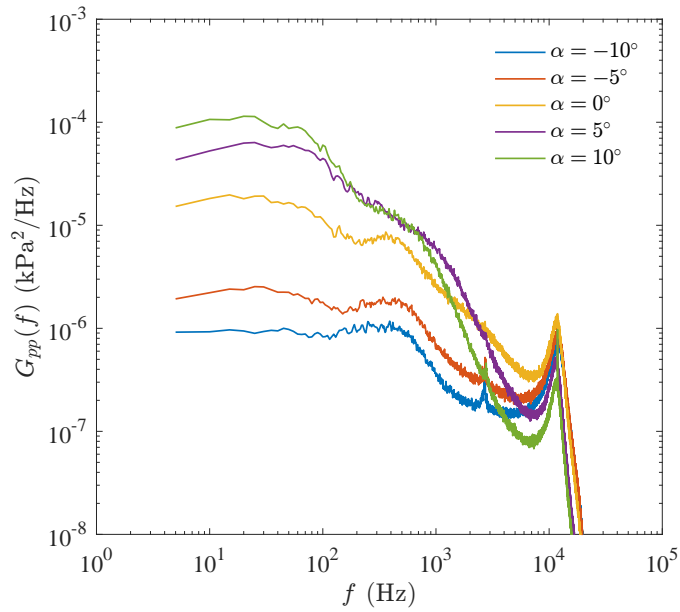


Figure 65. Auto spectral density of pressure sensor 10 versus angle of attack. F6 wing at $Re_c = 2.4$ million, with pressure sensor 6 as a reference for facility noise removal.

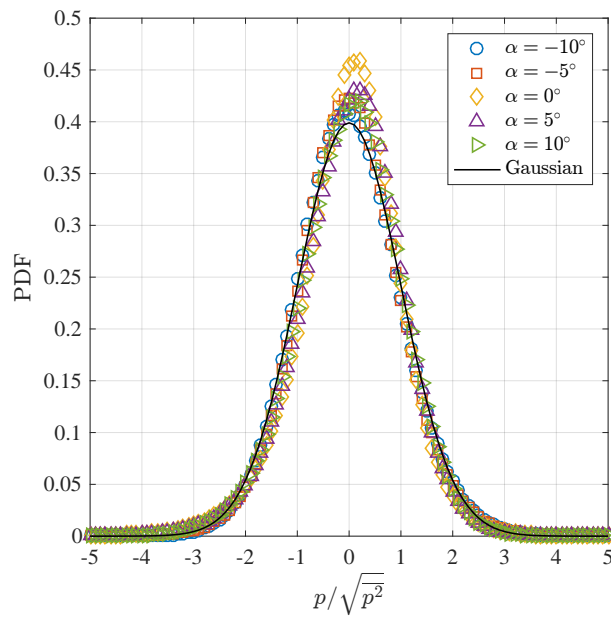


Figure 66. Probability density of pressure sensor 10 versus angle of attack. F6 wing at $Re_c = 2.4$ million, with pressure sensor 6 as a reference for facility noise removal.

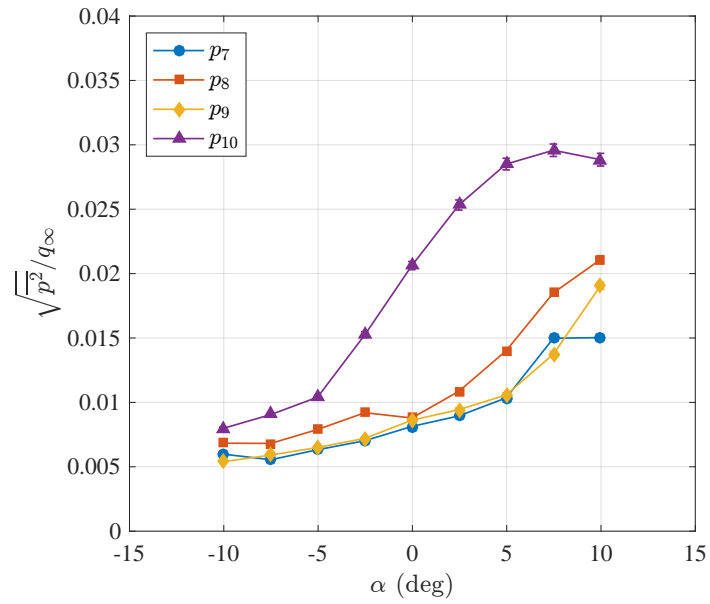


Figure 67. RMS for pressure sensors 7, 8, 9, and 10 versus angle of attack. F6 wing at $Re_c = 2.4$ million, with pressure sensor 6 as a reference for facility noise removal.

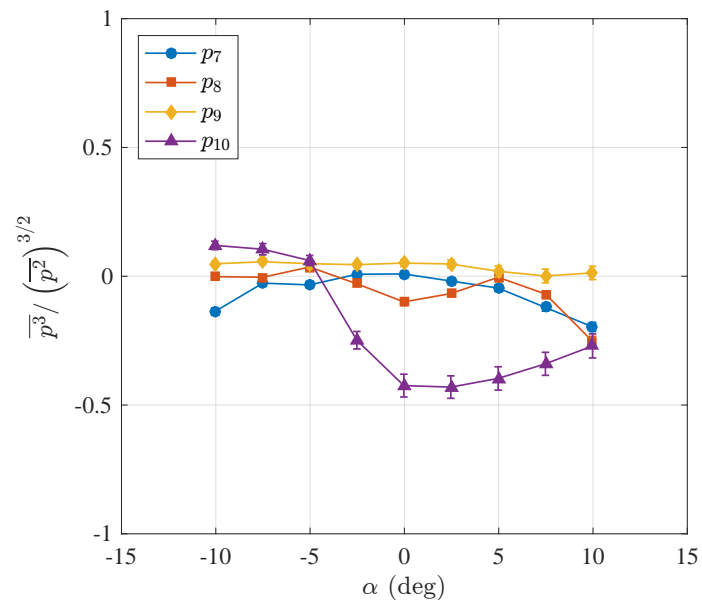


Figure 68. Skewness for pressure sensors 7, 8, 9, and 10 versus angle of attack. F6 wing at $Re_c = 2.4$ million, with pressure sensor 6 as a reference for facility noise removal.

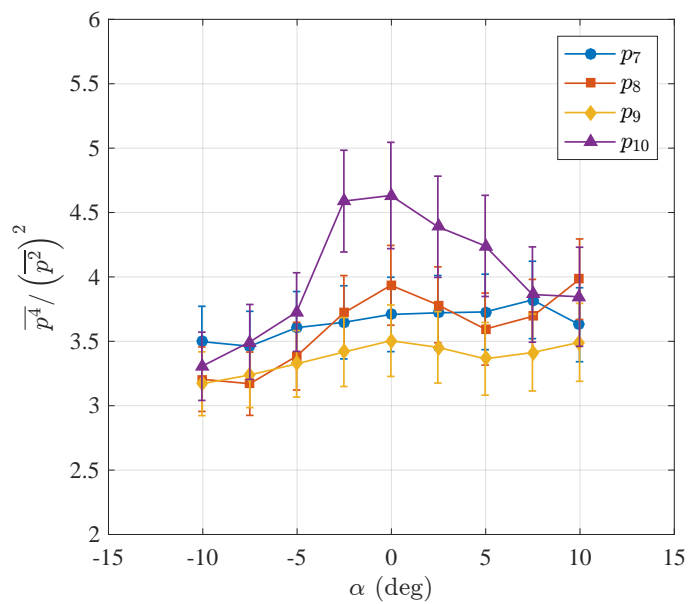


Figure 69. Flatness for pressure sensors 7, 8, 9, and 10 versus angle of attack. F6 wing at $Re_c = 2.4$ million, with pressure sensor 6 as a reference for facility noise removal.

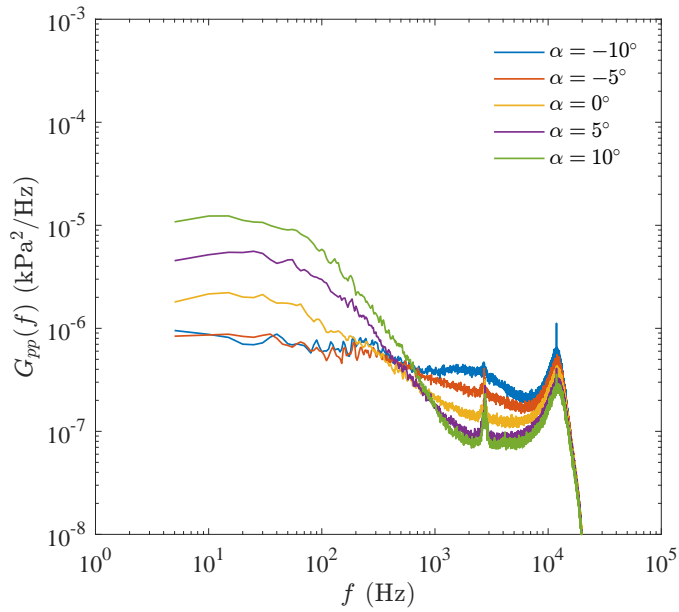


Figure 70. Auto spectral density of pressure sensor 11 versus angle of attack. F6 wing at $Re_c = 2.4$ million, with pressure sensor 14 as a reference for facility noise removal.

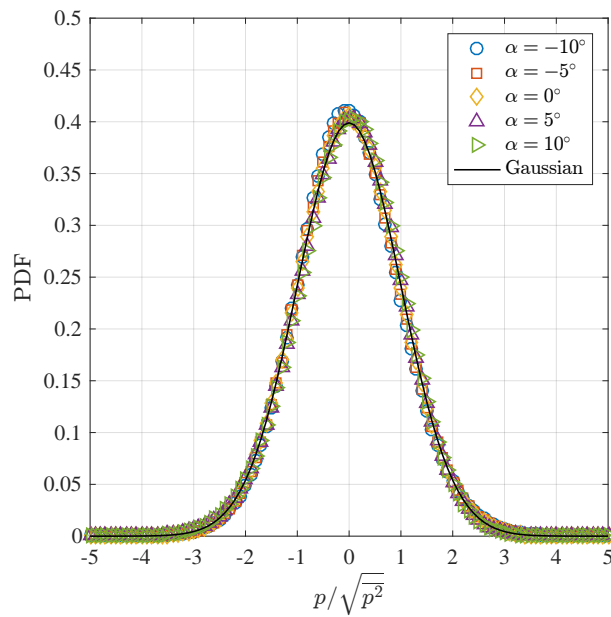


Figure 71. Probability density of pressure sensor 11 versus angle of attack. F6 wing at $Re_c = 2.4$ million, with pressure sensor 14 as a reference for facility noise removal.

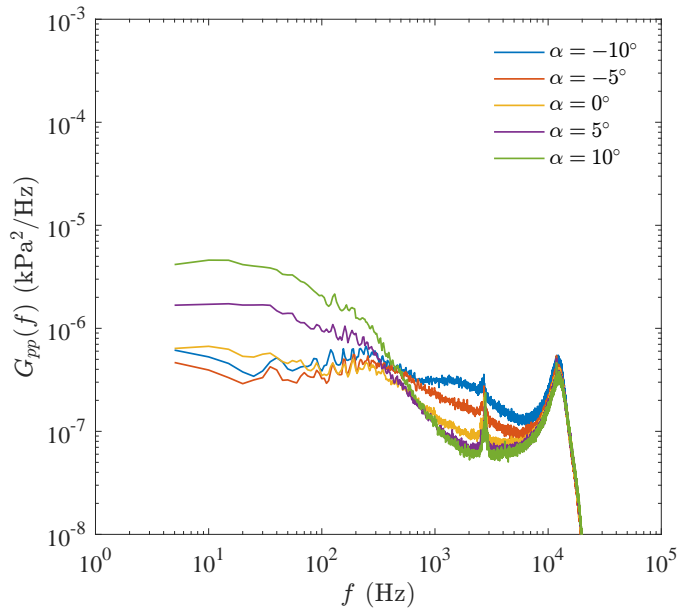


Figure 72. Auto spectral density of pressure sensor 12 versus angle of attack. F6 wing at $Re_c = 2.4$ million, with pressure sensor 14 as a reference for facility noise removal.

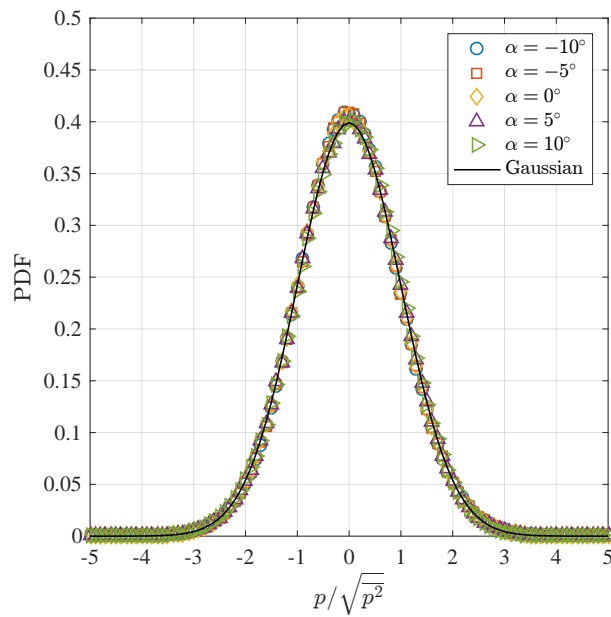


Figure 73. Probability density of pressure sensor 12 versus angle of attack. F6 wing at $Re_c = 2.4$ million, with pressure sensor 14 as a reference for facility noise removal.

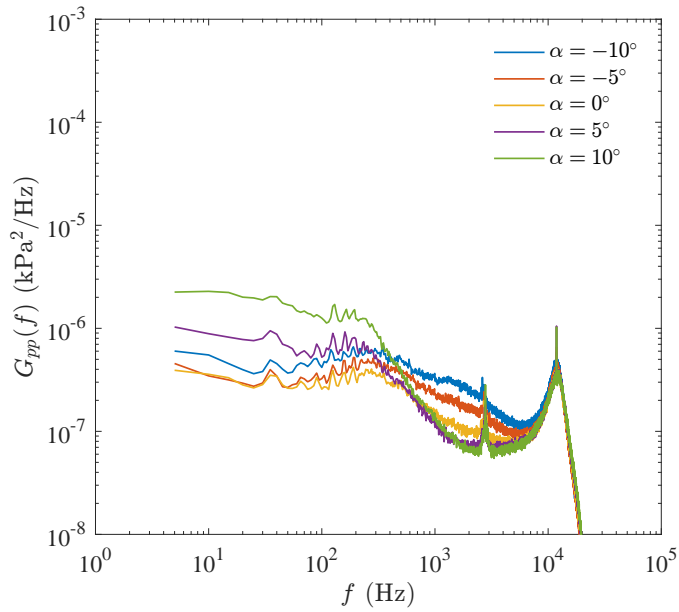


Figure 74. Auto spectral density of pressure sensor 13 versus angle of attack. F6 wing at $Re_c = 2.4$ million, with pressure sensor 14 as a reference for facility noise removal.

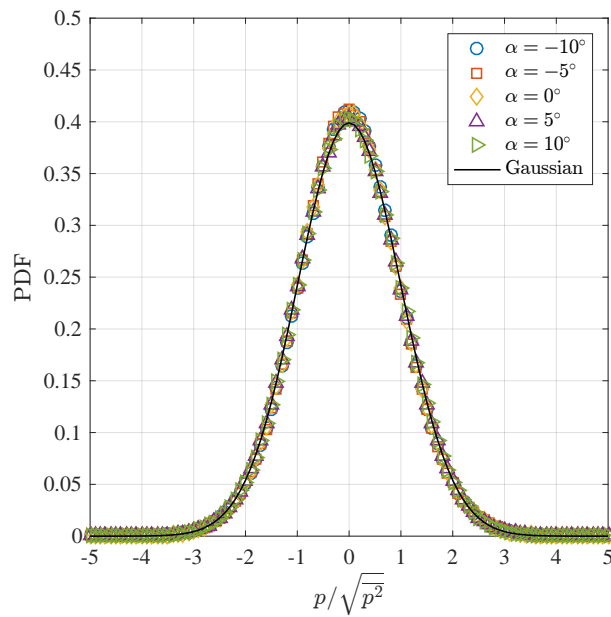


Figure 75. Probability density of pressure sensor 13 versus angle of attack. F6 wing at $Re_c = 2.4$ million, with pressure sensor 14 as a reference for facility noise removal.

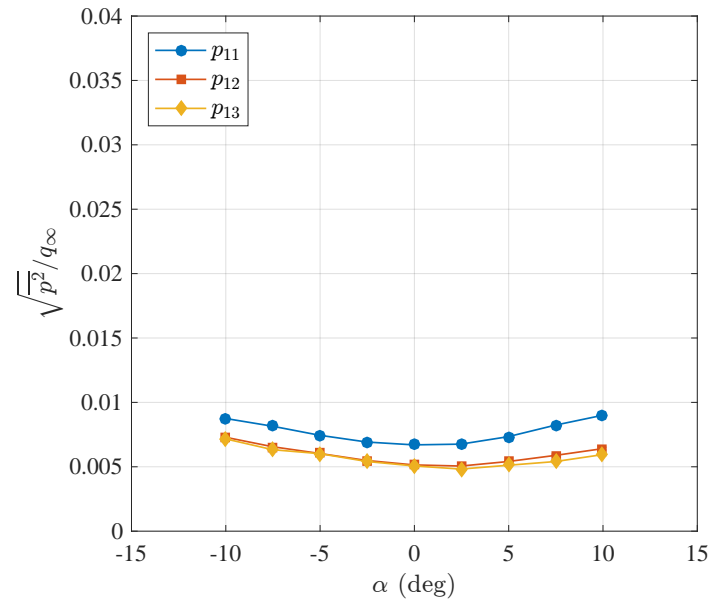


Figure 76. RMS for pressure sensors 11, 12, and 13 versus angle of attack. F6 wing at $Re_c = 2.4$ million, with pressure sensor 14 as a reference for facility noise removal.

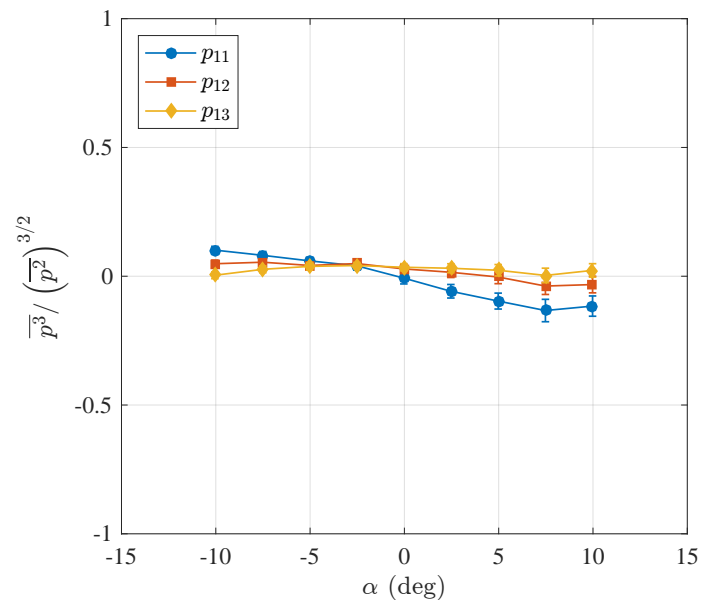


Figure 77. Skewness for pressure sensors 11, 12, and 13 versus angle of attack. F6 wing at $Re_c = 2.4$ million, with pressure sensor 14 as a reference for facility noise removal.

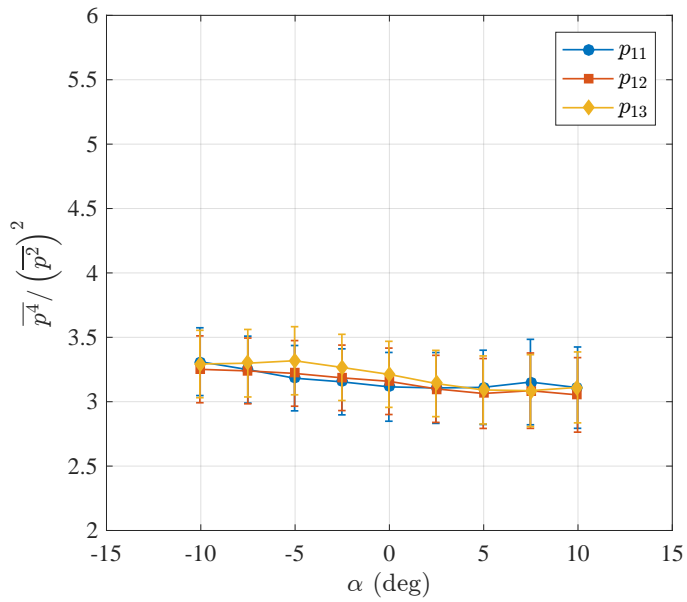


Figure 78. Flatness for pressure sensors 7, 8, 9, and 10 versus angle of attack. F6 wing at $Re_c = 2.4$ million, with pressure sensor 14 as a reference for facility noise removal.

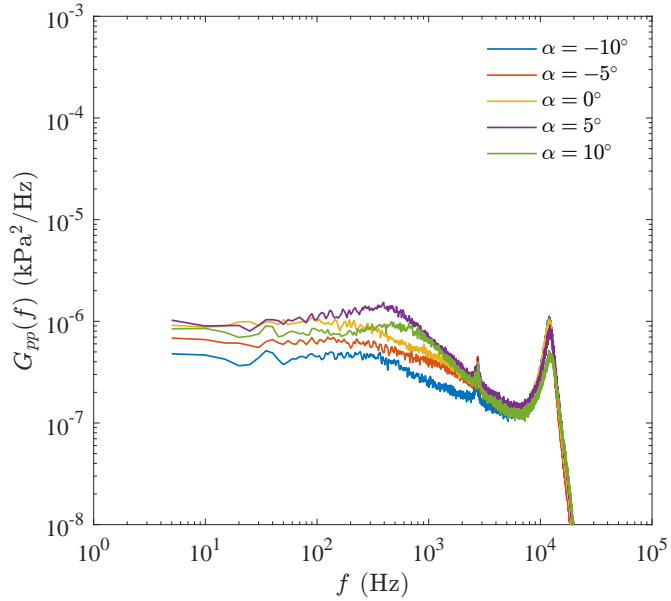


Figure 79. Auto spectral density of pressure sensor 1 versus angle of attack. F6 wing with leading-edge horn at $Re_c = 2.4$ million, with pressure sensor 2 as a reference for facility noise removal.

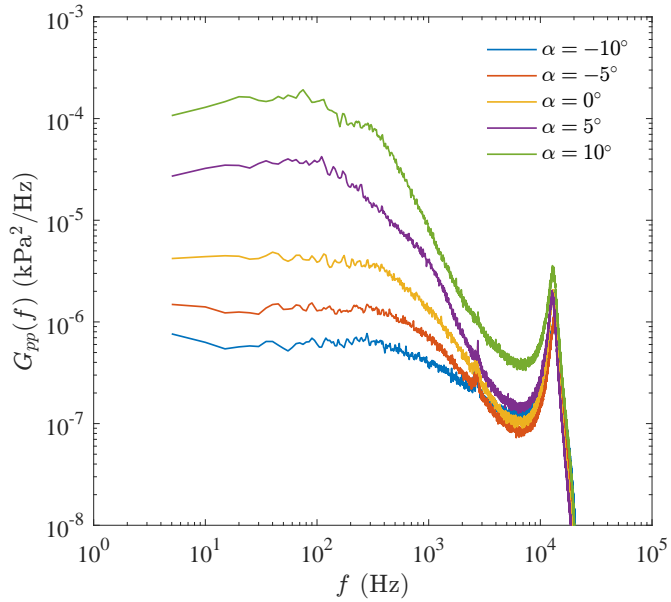


Figure 80. Auto spectral density of pressure sensor 4 versus angle of attack. F6 wing with leading-edge horn at $Re_c = 2.4$ million, with pressure sensor 2 as a reference for facility noise removal.

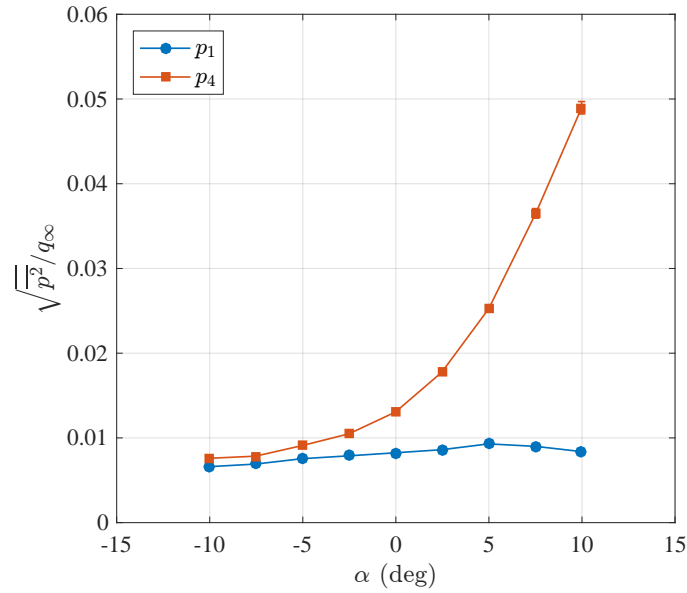


Figure 81. RMS for pressure sensors 1 and 4 versus angle of attack. F6 wing with leading-edge horn at $Re_c = 2.4$ million, with pressure sensor 2 as a reference for facility noise removal.

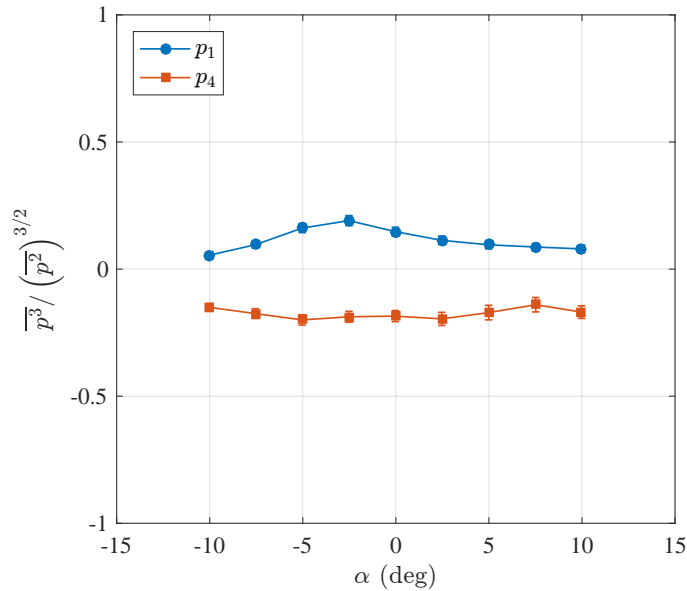


Figure 82. Skewness for pressure sensors 1 and 4 versus angle of attack. F6 wing with leading-edge horn at $Re_c = 2.4$ million, with pressure sensor 2 as a reference for facility noise removal.

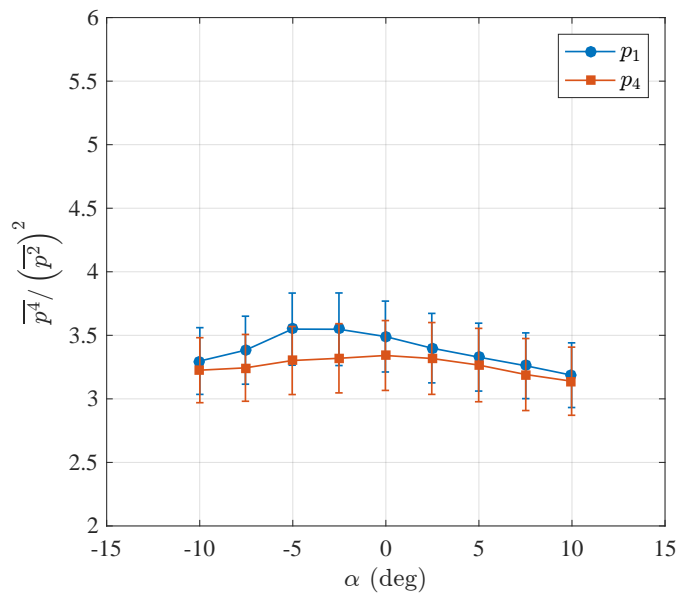


Figure 83. Flatness for pressure sensors 1 and 4 versus angle of attack. F6 wing with leading-edge horn at $Re_c = 2.4$ million, with pressure sensor 2 as a reference for facility noise removal.

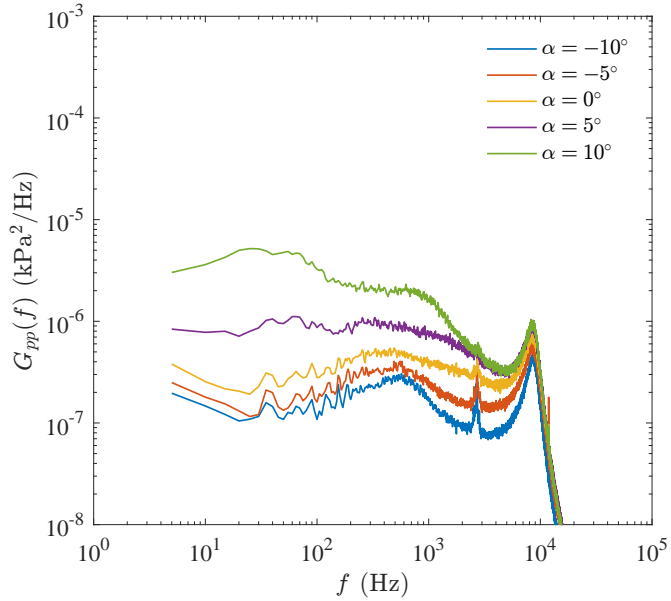


Figure 84. Auto spectral density of pressure sensor 7 versus angle of attack. F6 wing with leading-edge horn at $Re_c = 2.4$ million, with pressure sensor 6 as a reference for facility noise removal.

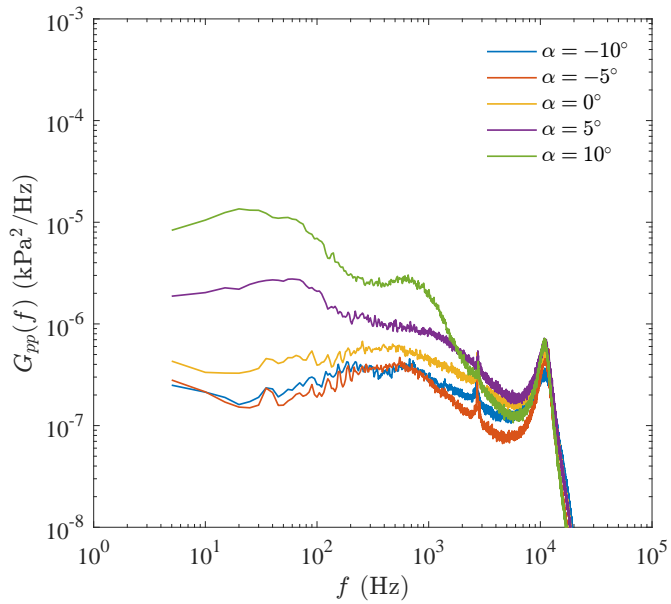


Figure 85. Auto spectral density of pressure sensor 8 versus angle of attack. F6 wing with leading-edge horn at $Re_c = 2.4$ million, with pressure sensor 6 as a reference for facility noise removal.

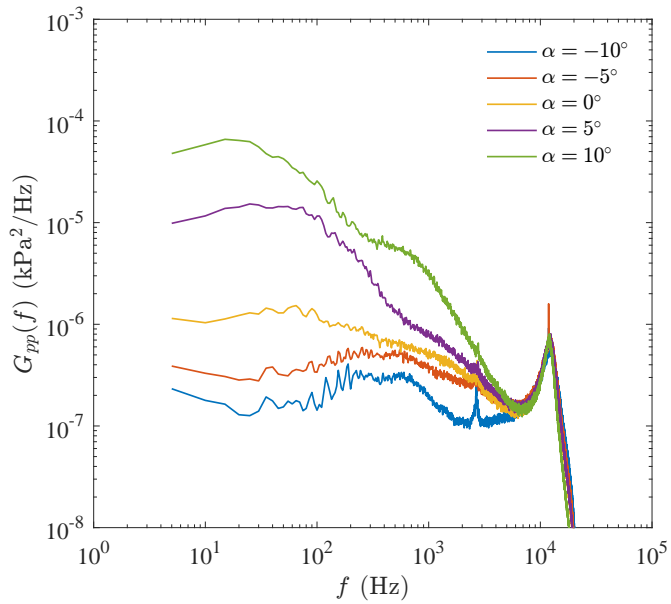


Figure 86. Auto spectral density of pressure sensor 9 versus angle of attack. F6 wing with leading-edge horn at $Re_c = 2.4$ million, with pressure sensor 6 as a reference for facility noise removal.

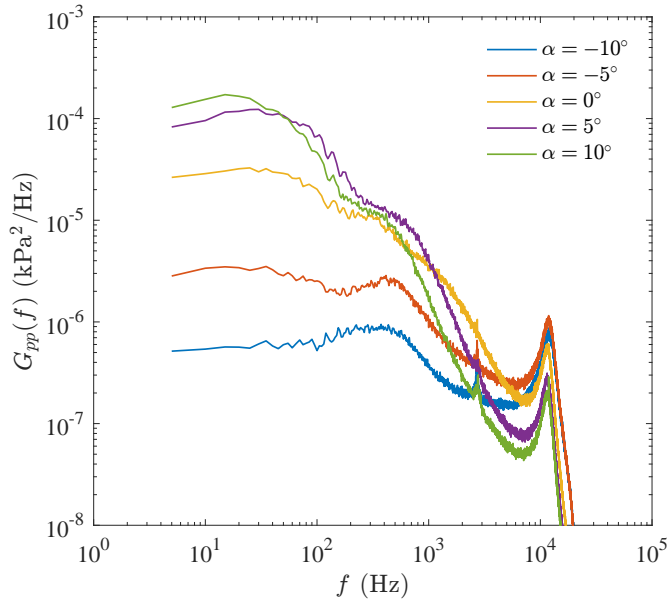


Figure 87. Auto spectral density of pressure sensor 10 versus angle of attack. F6 wing with leading-edge horn at $Re_c = 2.4$ million, with pressure sensor 6 as a reference for facility noise removal.

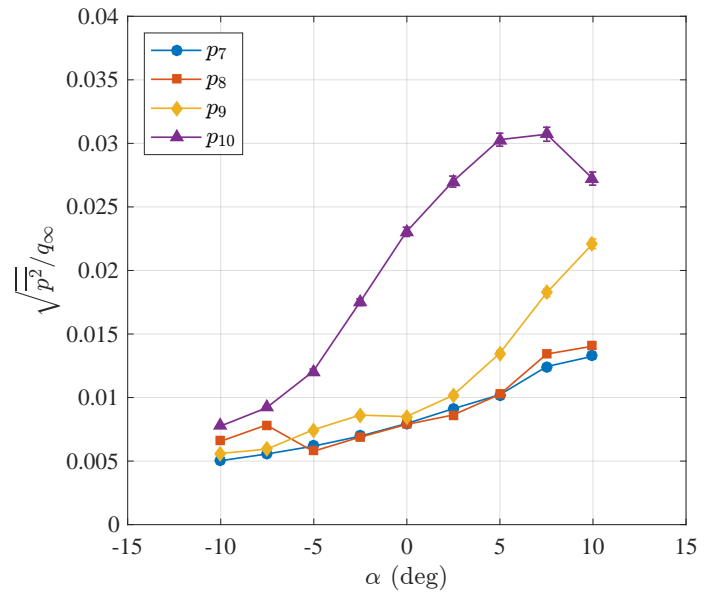


Figure 88. RMS for pressure sensors 7, 8, 9, and 10 versus angle of attack. F6 wing with leading-edge horn at $Re_c = 2.4$ million, with pressure sensor 6 as a reference for facility noise removal.

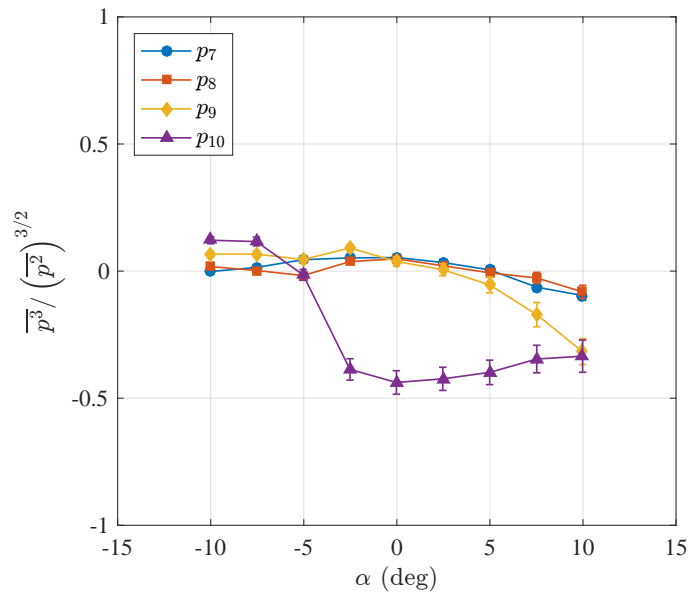


Figure 89. Skewness for pressure sensors 7, 8, 9, and 10 versus angle of attack. F6 wing with leading-edge horn at $Re_c = 2.4$ million, with pressure sensor 6 as a reference for facility noise removal.

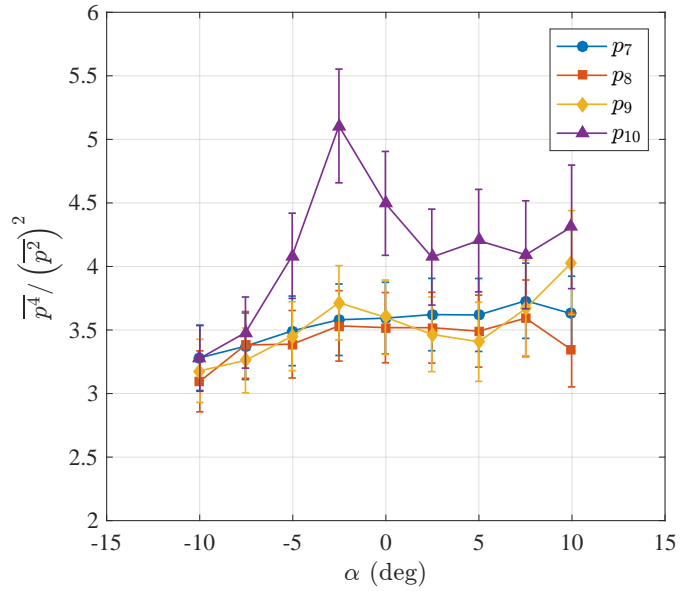


Figure 90. Flatness for pressure sensors 7, 8, 9, and 10 versus angle of attack. F6 wing with leading-edge horn at $Re_c = 2.4$ million, with pressure sensor 6 as a reference for facility noise removal.

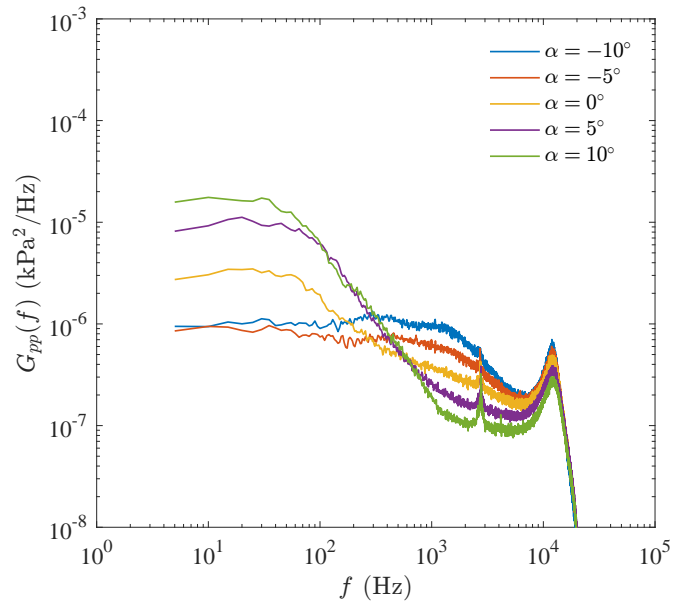


Figure 91. Auto spectral density of pressure sensor 11 versus angle of attack. F6 wing with leading-edge horn at $Re_c = 2.4$ million, with pressure sensor 14 as a reference for facility noise removal.

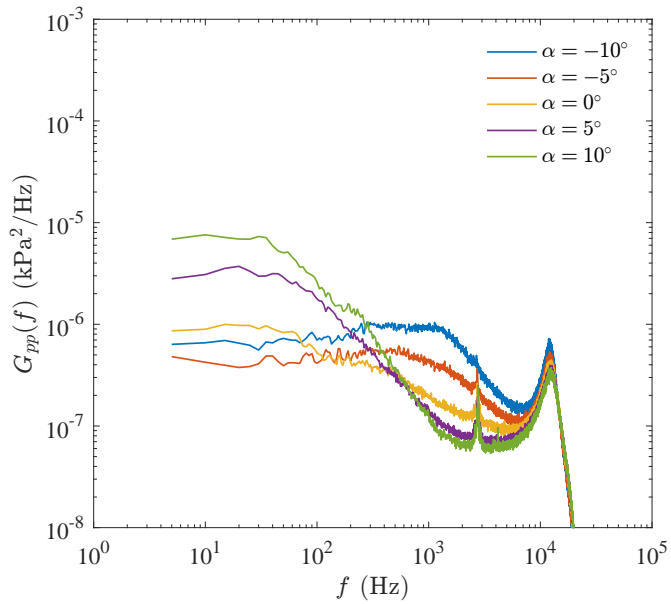


Figure 92. Auto spectral density of pressure sensor 12 versus angle of attack. F6 wing with leading-edge horn at $Re_c = 2.4$ million, with pressure sensor 14 as a reference for facility noise removal.

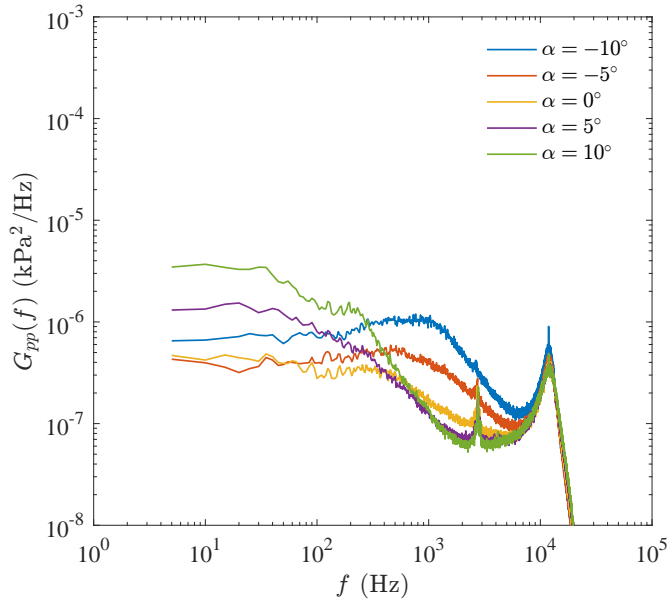


Figure 93. Auto spectral density of pressure sensor 13 versus angle of attack. F6 wing with leading-edge horn at $Re_c = 2.4$ million, with pressure sensor 14 as a reference for facility noise removal.

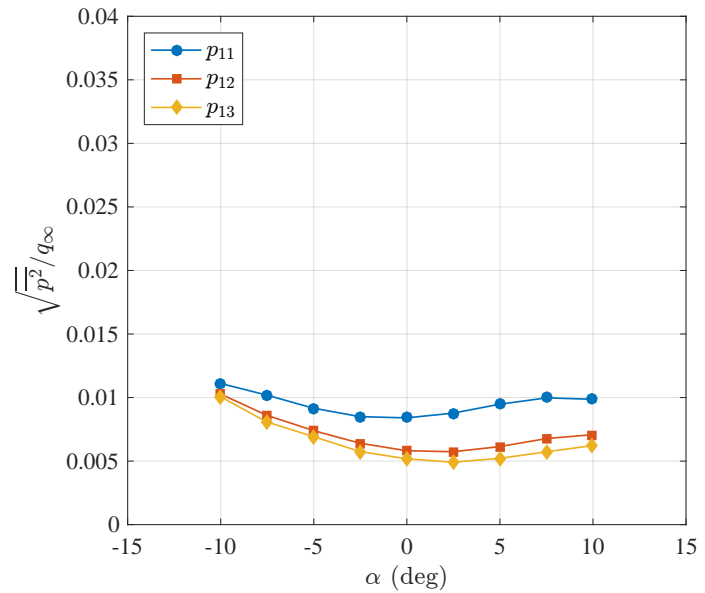


Figure 94. RMS for pressure sensors 11, 12, and 13 versus angle of attack. F6 wing with leading-edge horn at $Re_c = 2.4$ million, with pressure sensor 14 as a reference for facility noise removal.

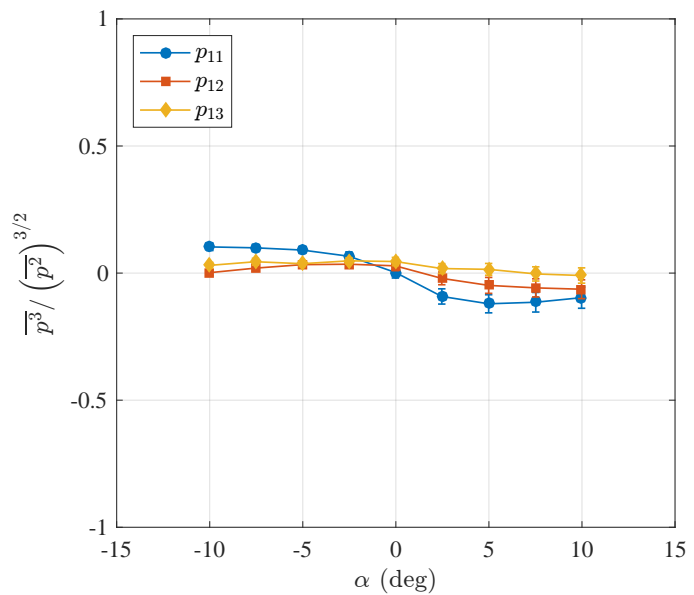


Figure 95. Skewness for pressure sensors 11, 12, and 13 versus angle of attack. F6 wing with leading-edge horn at $Re_c = 2.4$ million, with pressure sensor 14 as a reference for facility noise removal.

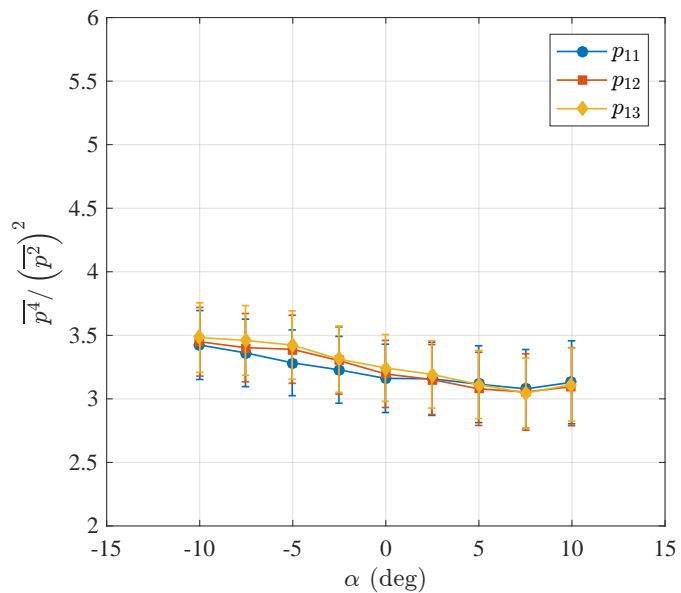


Figure 96. Flatness for pressure sensors 7, 8, 9, and 10 versus angle of attack. F6 wing with leading-edge horn at $Re_c = 2.4$ million, with pressure sensor 14 as a reference for facility noise removal.

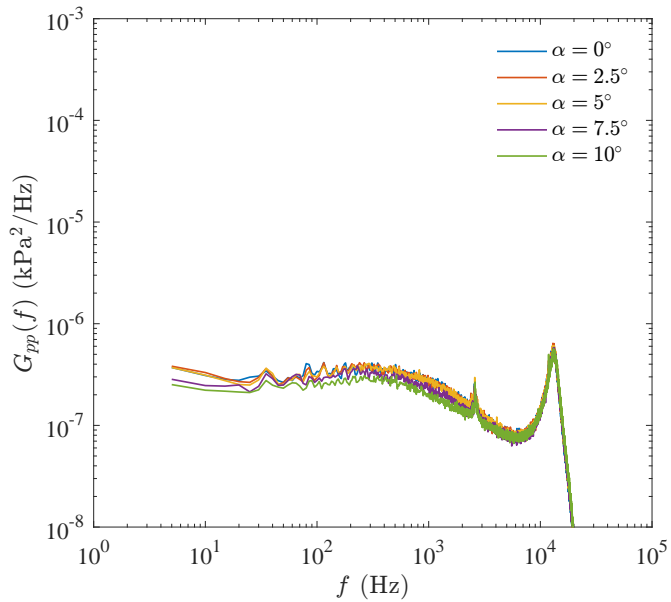


Figure 97. Auto spectral density of pressure sensor 2 versus angle of attack. NACA 0015 wing with leading-edge horn at $Re_c = 2.4$ million, with pressure sensor 1 as a reference for facility noise removal.

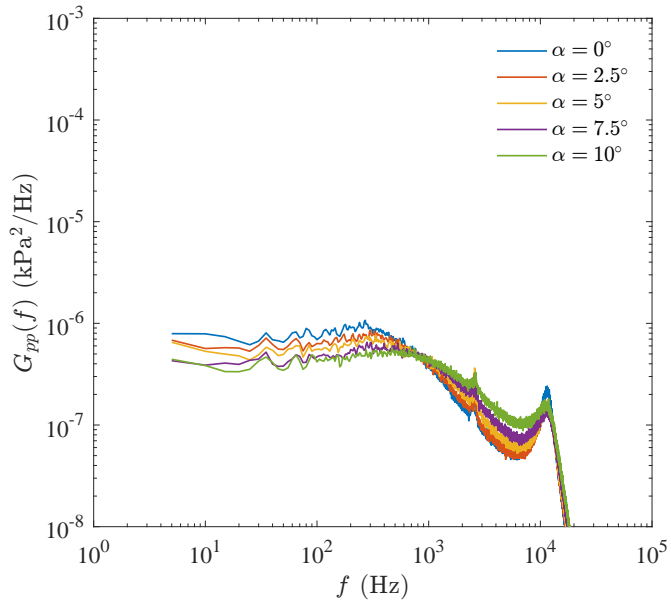


Figure 98. Auto spectral density of pressure sensor 3 versus angle of attack. NACA 0015 wing with leading-edge horn at $Re_c = 2.4$ million, with pressure sensor 1 as a reference for facility noise removal.

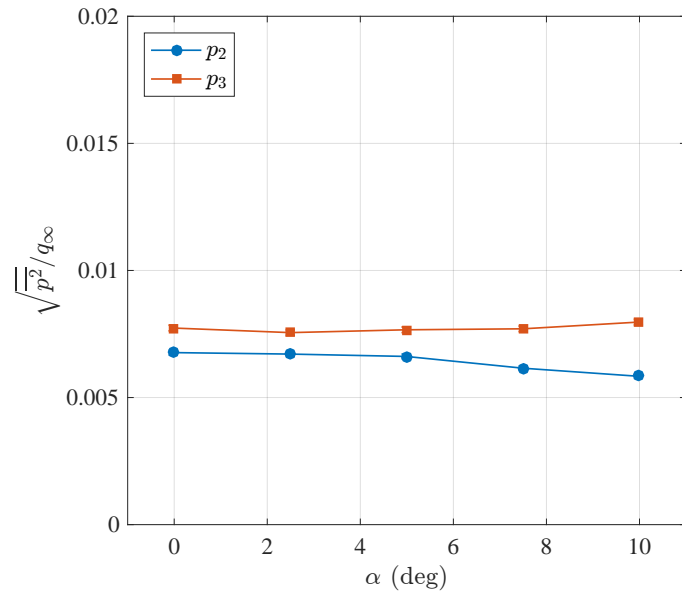


Figure 99. RMS for pressure sensors 2 and 3 versus angle of attack. NACA 0015 with leading-edge horn at $Re_c = 2.4$ million, with pressure sensor 1 as a reference for facility noise removal.

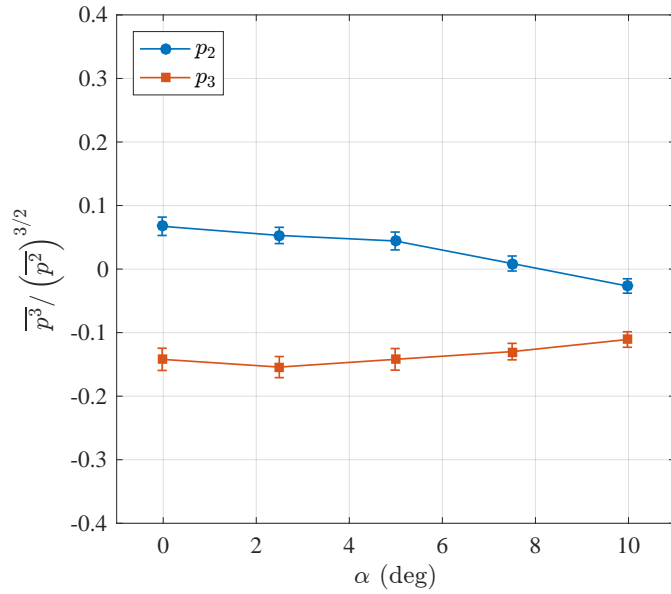


Figure 100. Skewness for pressure sensors 2 and 3 versus angle of attack. NACA 0015 with leading-edge horn at $Re_c = 2.4$ million, with pressure sensor 1 as a reference for facility noise removal.

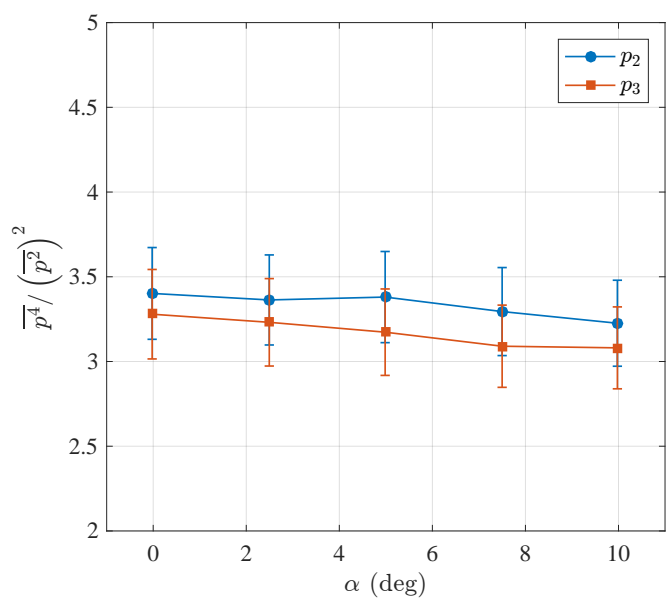


Figure 101. Flatness for pressure sensors 2 and 3 versus angle of attack. NACA 0015 with leading-edge horn at $Re_c = 2.4$ million, with pressure sensor 1 as a reference for facility noise removal.

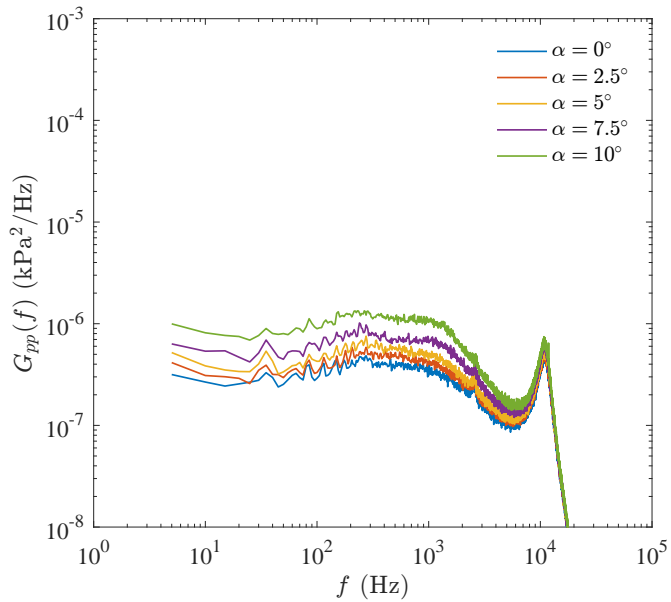


Figure 102. Auto spectral density of pressure sensor 8 versus angle of attack. NACA 0015 wing with leading-edge horn at $Re_c = 2.4$ million, with pressure sensor 6 as a reference for facility noise removal.

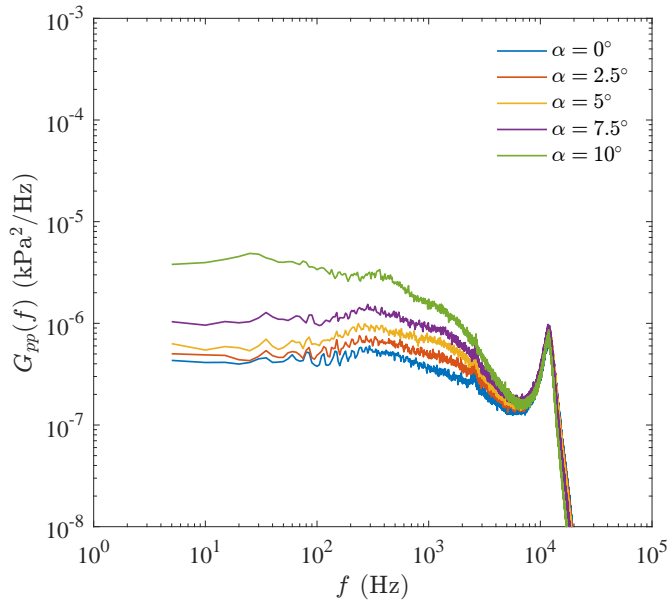


Figure 103. Auto spectral density of pressure sensor 9 versus angle of attack. NACA 0015 wing with leading-edge horn at $Re_c = 2.4$ million, with pressure sensor 6 as a reference for facility noise removal.

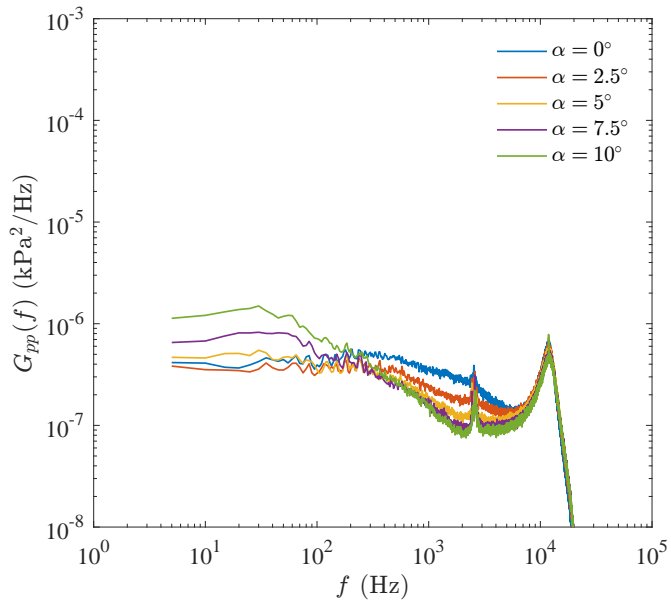


Figure 104. Auto spectral density of pressure sensor 10 versus angle of attack. NACA 0015 wing with leading-edge horn at $Re_c = 2.4$ million, with pressure sensor 14 as a reference for facility noise removal.

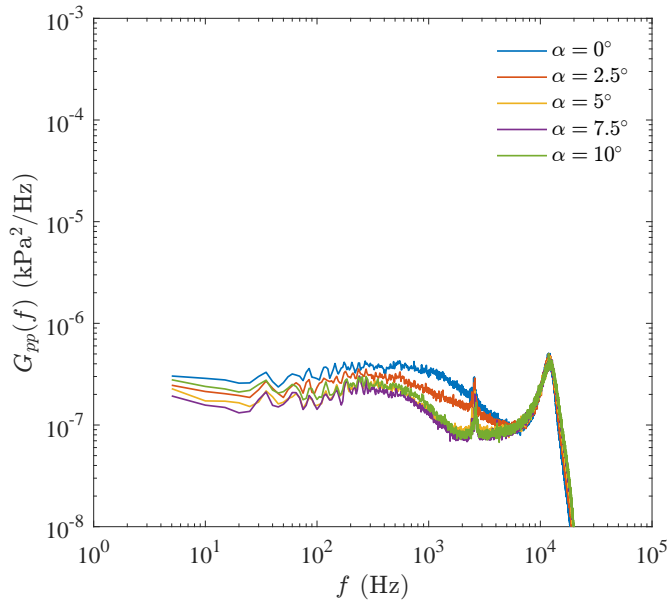


Figure 105. Auto spectral density of pressure sensor 11 versus angle of attack. NACA 0015 wing with leading-edge horn at $Re_c = 2.4$ million, with pressure sensor 14 as a reference for facility noise removal.

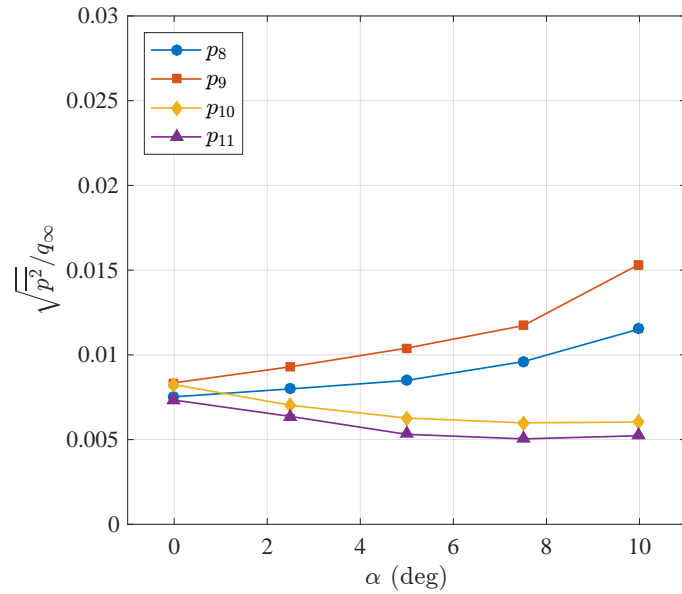


Figure 106. RMS for pressure sensors 8, 9, 10 and 11 versus angle of attack. NACA 0015 with leading-edge horn at $Re_c = 2.4$ million, with pressure sensors 6 (for sensors 8 and 9) and 14 (for sensors 10 and 11) as references for facility noise removal.

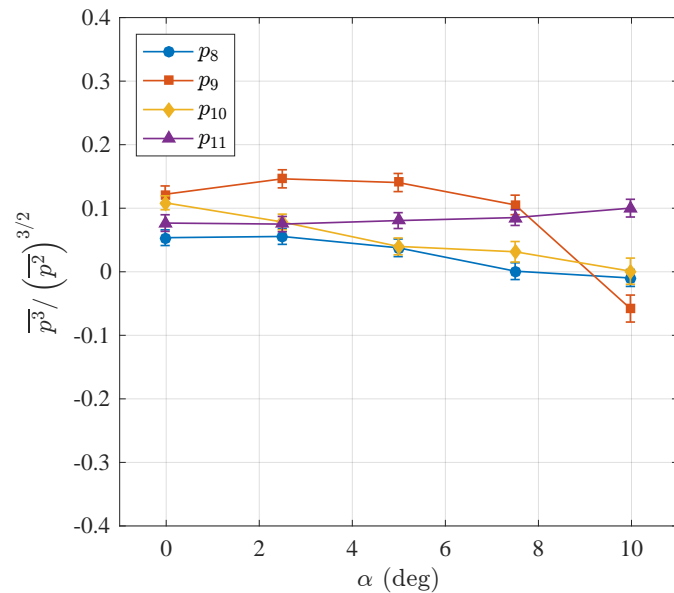


Figure 107. Skewness for pressure sensors 8, 9, 10 and 11 versus angle of attack. NACA 0015 with leading-edge horn at $Re_c = 2.4$ million, with pressure sensors 6 (for sensors 8 and 9) and 14 (for sensors 10 and 11) as references for facility noise removal.

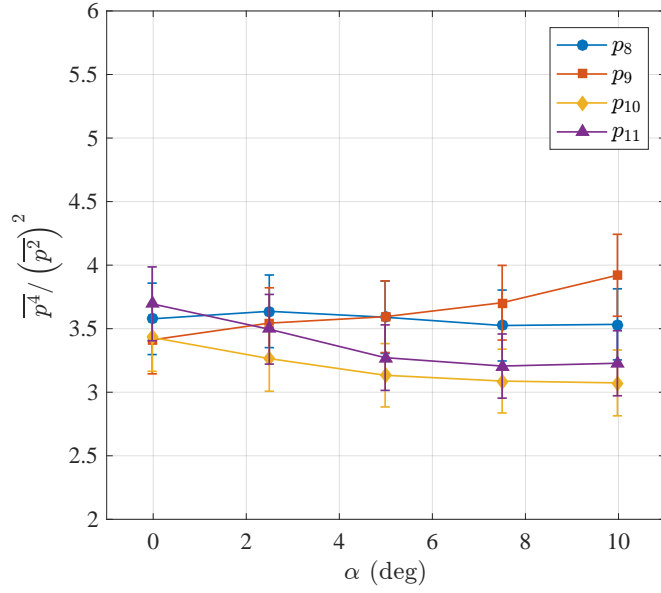


Figure 108. Flatness for pressure sensors 8, 9, 10 and 11 versus angle of attack. NACA 0015 with leading-edge horn at $Re_c = 2.4$ million, with pressure sensors 6 (for sensors 8 and 9) and 14 (for sensors 10 and 11) as references for facility noise removal.

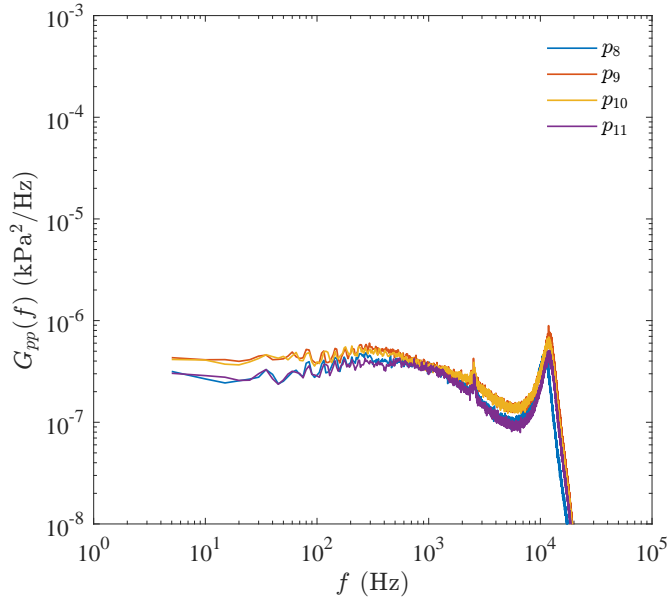


Figure 109. Auto spectral density of pressure sensors 8, 9, 10, and 11 at $\alpha = 0^\circ$. NACA 0015 wing with leading-edge horn at $Re_c = 2.4$ million, with pressure sensors 6 (for sensors 8 and 9) and 14 (for sensors 10 and 11) as references for facility noise removal.

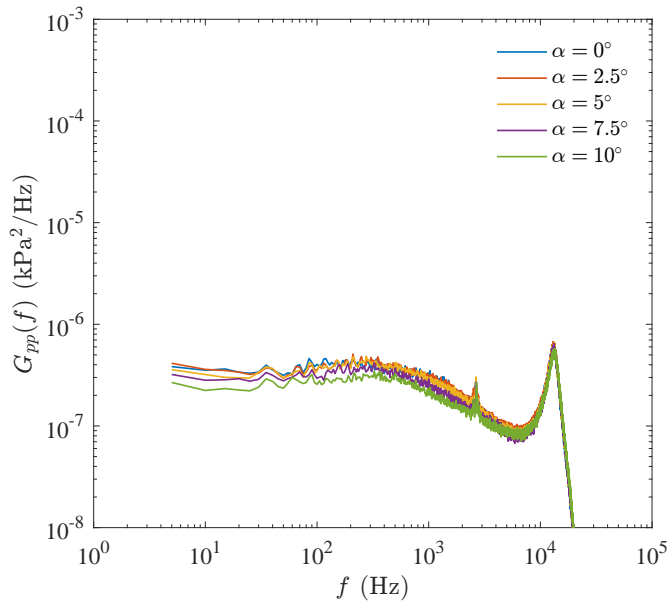


Figure 110. Auto spectral density of pressure sensor 2 versus angle of attack. F6 S12 wing with leading-edge horn at $Re_c = 2.4$ million, with pressure sensor 1 as a reference for facility noise removal.

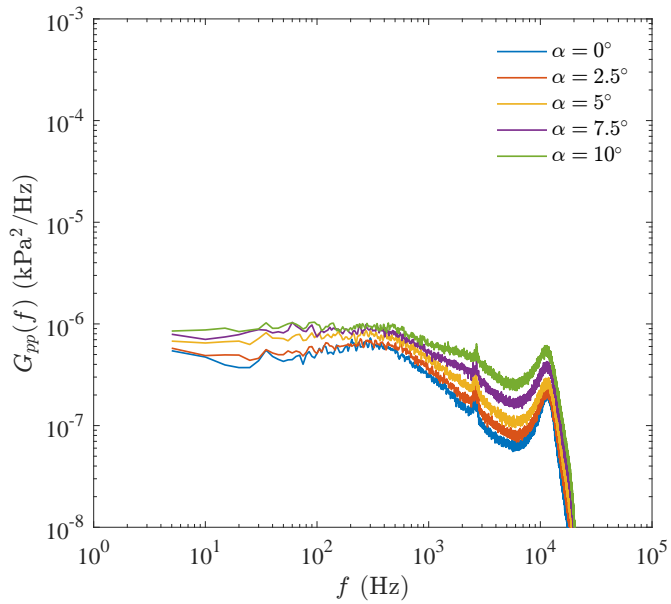


Figure 111. Auto spectral density of pressure sensor 3 versus angle of attack. F6 S12 wing with leading-edge horn at $Re_c = 2.4$ million, with pressure sensor 1 as a reference for facility noise removal.

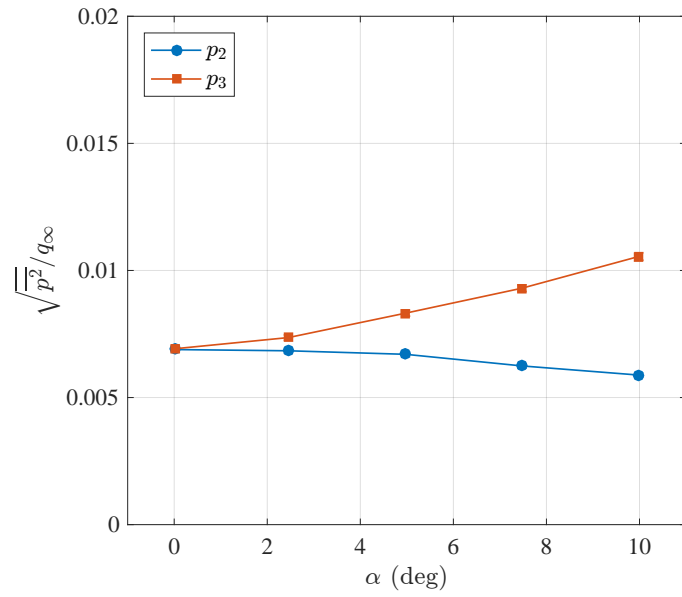


Figure 112. RMS for pressure sensors 2 and 3 versus angle of attack. F6 S12 with leading-edge horn at $Re_c = 2.4$ million, with pressure sensor 1 as a reference for facility noise removal.

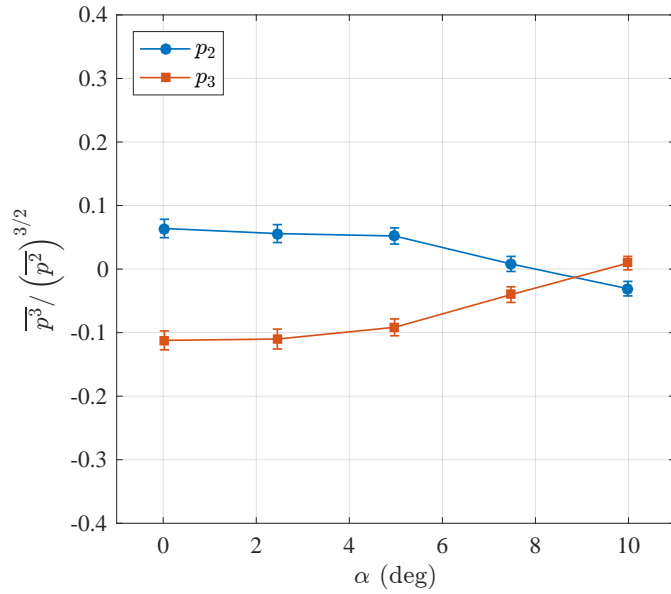


Figure 113. Skewness for pressure sensors 2 and 3 versus angle of attack. F6 S12 with leading-edge horn at $Re_c = 2.4$ million, with pressure sensor 1 as a reference for facility noise removal.

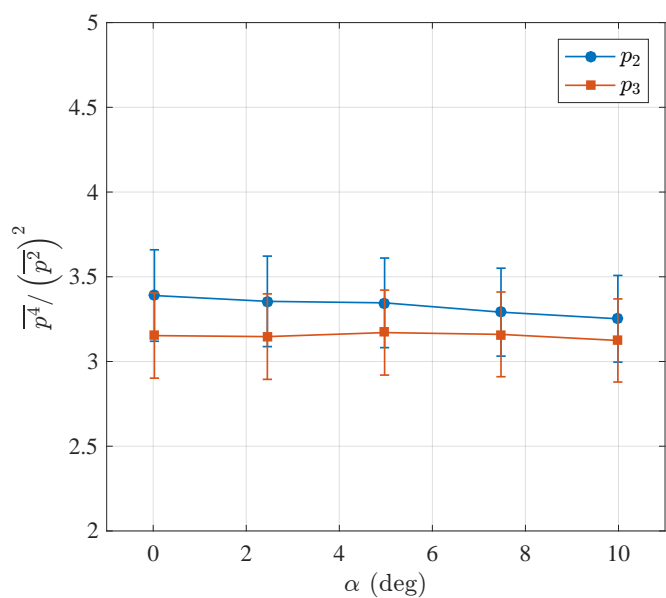


Figure 114. Flatness for pressure sensors 2 and 3 versus angle of attack. F6 S12 with leading-edge horn at $Re_c = 2.4$ million, with pressure sensor 1 as a reference for facility noise removal.

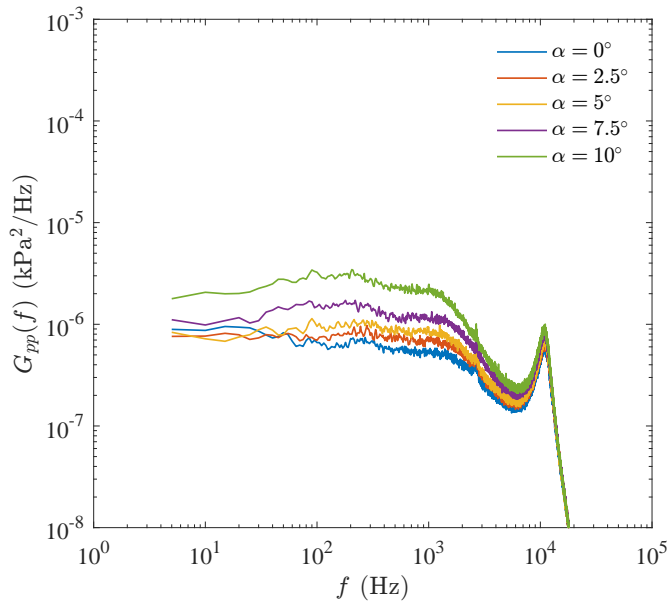


Figure 115. Auto spectral density of pressure sensor 8 versus angle of attack. F6 S12 wing with leading-edge horn at $Re_c = 2.4$ million, with pressure sensor 6 as a reference for facility noise removal.

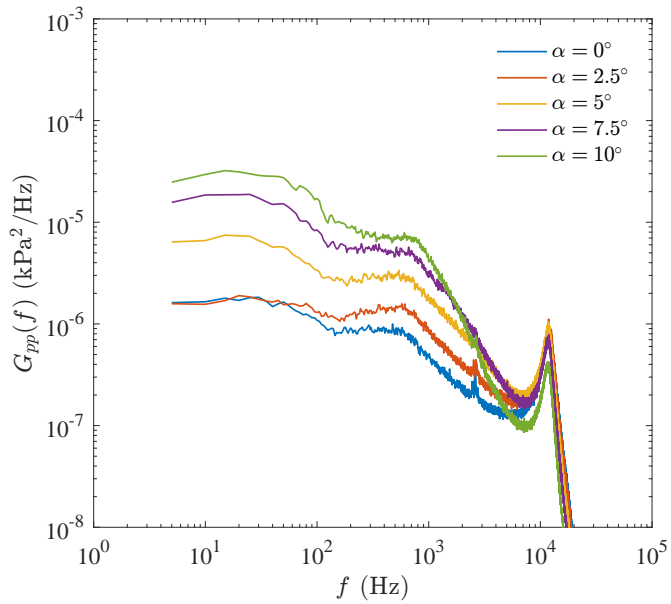


Figure 116. Auto spectral density of pressure sensor 9 versus angle of attack. F6 S12 wing with leading-edge horn at $Re_c = 2.4$ million, with pressure sensor 6 as a reference for facility noise removal.

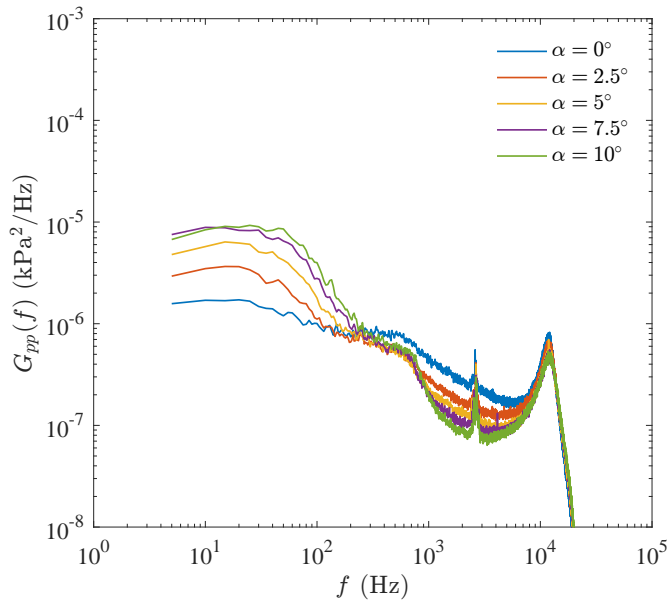


Figure 117. Auto spectral density of pressure sensor 10 versus angle of attack. F6 S12 wing with leading-edge horn at $Re_c = 2.4$ million, with pressure sensor 14 as a reference for facility noise removal.

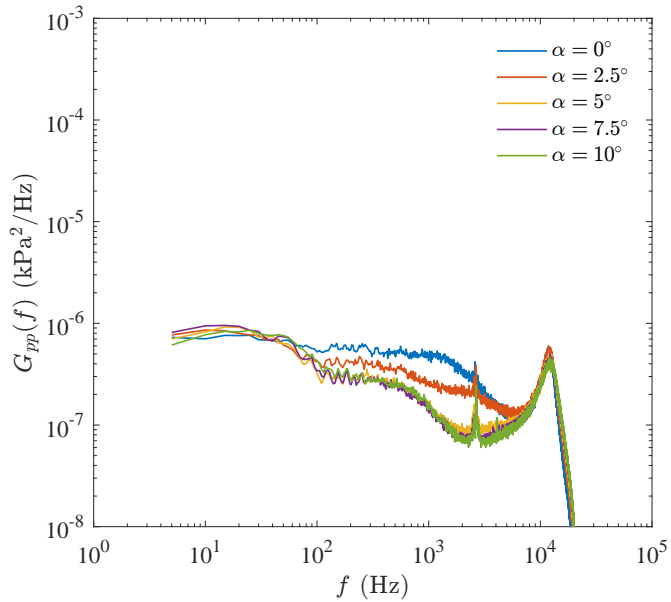


Figure 118. Auto spectral density of pressure sensor 11 versus angle of attack. F6 S12 wing with leading-edge horn at $Re_c = 2.4$ million, with pressure sensor 14 as a reference for facility noise removal.

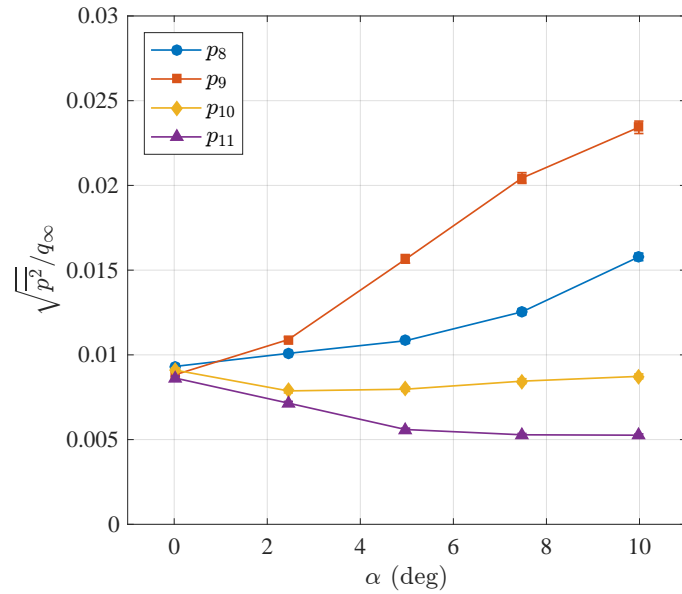


Figure 119. RMS for pressure sensors 8, 9, 10 and 11 versus angle of attack. F6 S12 with leading-edge horn at $Re_c = 2.4$ million, with pressure sensors 6 (for sensors 8 and 9) and 14 (for sensors 10 and 11) as references for facility noise removal.

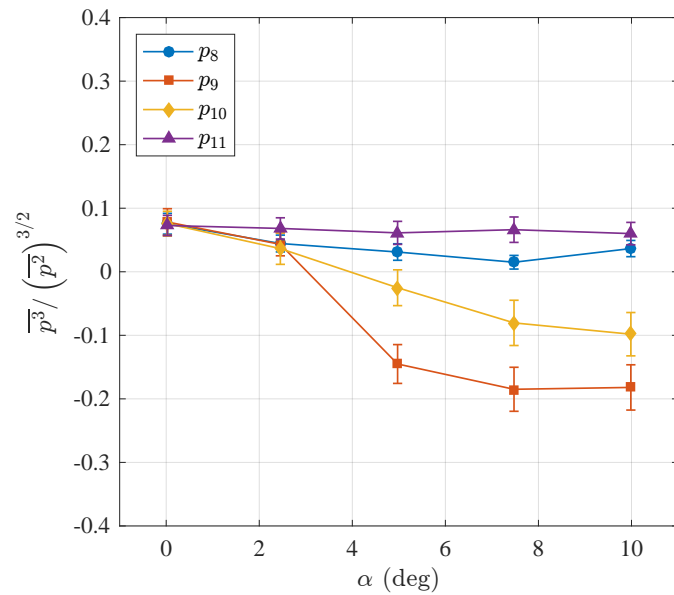


Figure 120. Skewness for pressure sensors 8, 9, 10 and 11 versus angle of attack. F6 S12 with leading-edge horn at $Re_c = 2.4$ million, with pressure sensors 6 (for sensors 8 and 9) and 14 (for sensors 10 and 11) as references for facility noise removal.

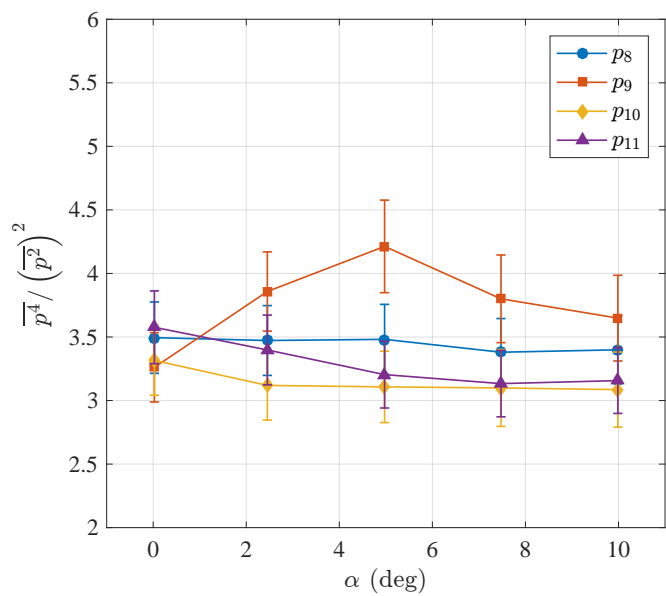


Figure 121. Flatness for pressure sensors 8, 9, 10 and 11 versus angle of attack. F6 S12 with leading-edge horn at $Re_c = 2.4$ million, with pressure sensors 6 (for sensors 8 and 9) and 14 (for sensors 10 and 11) as references for facility noise removal.

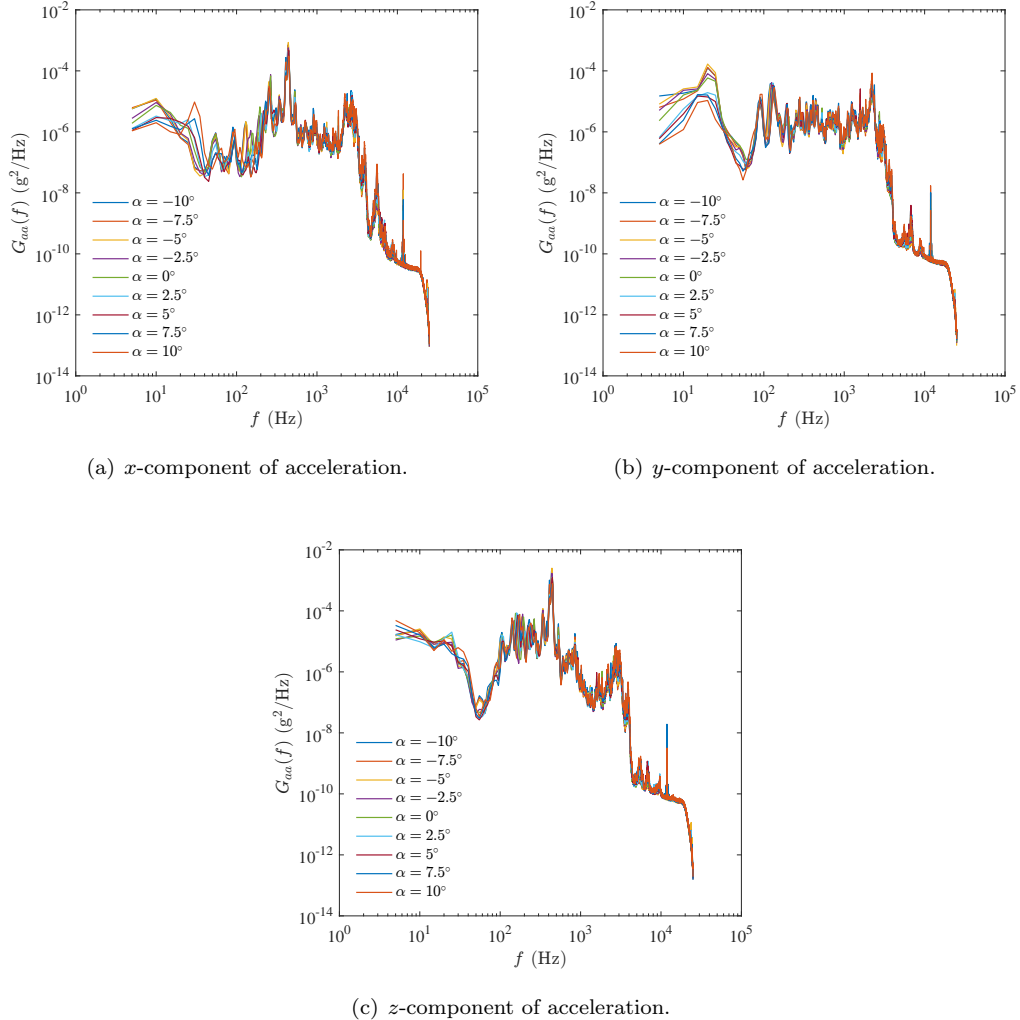


Figure 122. Auto spectral densities of acceleration components versus model angle of attack. F6 wing with leading-edge horn at $Re_c = 2.4$ million.

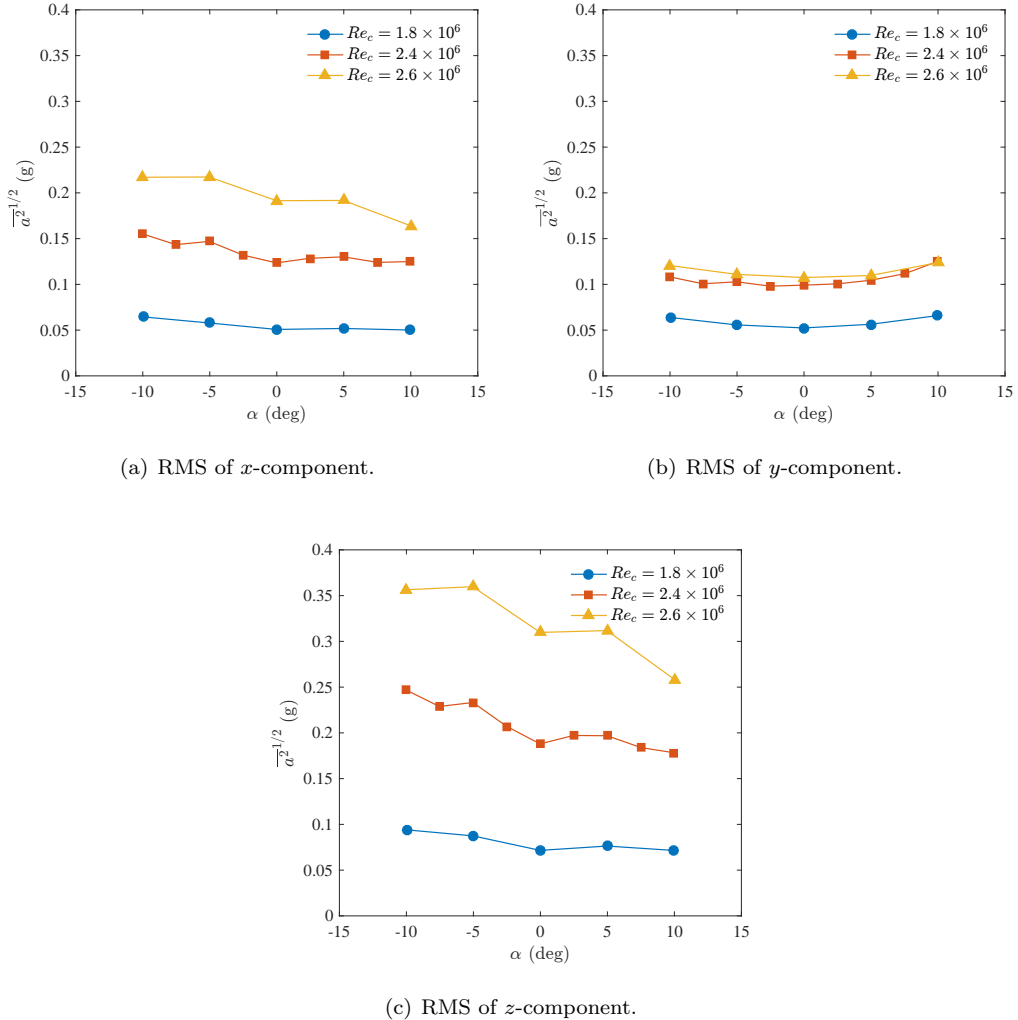


Figure 123. RMS of acceleration components versus model angle of attack. F6 wing with leading-edge horn at $Re_c = 2.4$ million.

REPORT DOCUMENTATION PAGE				Form Approved OMB No. 0704-0188	
<p>The public reporting burden for this collection of information is estimated to average 1 hour per response, including the time for reviewing instructions, searching existing data sources, gathering and maintaining the data needed, and completing and reviewing the collection of information. Send comments regarding this burden estimate or any other aspect of this collection of information, including suggestions for reducing this burden, to Department of Defense, Washington Headquarters Services, Directorate for Information Operations and Reports (0704-0188), 1215 Jefferson Davis Highway, Suite 1204, Arlington, VA 22202-4302. Respondents should be aware that notwithstanding any other provision of law, no person shall be subject to any penalty for failing to comply with a collection of information if it does not display a currently valid OMB control number.</p> <p>PLEASE DO NOT RETURN YOUR FORM TO THE ABOVE ADDRESS.</p>					
1. REPORT DATE (DD-MM-YYYY) 01-11-2016	2. REPORT TYPE Technical Memorandum	3. DATES COVERED (From - To)			
4. TITLE AND SUBTITLE Wind Tunnel Test of a Risk-Reduction Wing/Fuselage Model to Examine Juncture-Flow Phenomena		5a. CONTRACT NUMBER			
		5b. GRANT NUMBER			
		5c. PROGRAM ELEMENT NUMBER			
6. AUTHOR(S) Kegerise, Michael A; Neuhart, Dan H		5d. PROJECT NUMBER			
		5e. TASK NUMBER			
		5f. WORK UNIT NUMBER 109492.02.07.01.01			
7. PERFORMING ORGANIZATION NAME(S) AND ADDRESS(ES) NASA Langley Research Center Hampton, Virginia 23681-2199			8. PERFORMING ORGANIZATION REPORT NUMBER L-20760		
9. SPONSORING/MONITORING AGENCY NAME(S) AND ADDRESS(ES) National Aeronautics and Space Administration Washington, DC 20546-0001			10. SPONSOR/MONITOR'S ACRONYM(S) NASA		
			11. SPONSOR/MONITOR'S REPORT NUMBER(S) NASA/TM-2016-219348		
12. DISTRIBUTION/AVAILABILITY STATEMENT Unclassified-Unlimited Subject Category 02 Availability: NASA CASI (301) 621-0390					
13. SUPPLEMENTARY NOTES An electronic version can be found at http://ntrs.nasa.gov .					
14. ABSTRACT A wing/fuselage wind-tunnel model was tested in the Langley 14- by 22-foot Subsonic Wind Tunnel in preparation for a highly-instrumented Juncture Flow Experiment to be conducted in the same facility. This test, which was sponsored by the NASA Transformational Tool and Technologies Project, is part of a comprehensive set of experimental and computational research activities to develop revolutionary, physics-based aeronautics analysis and design capability. The objectives of this particular test were to examine the surface and off-body flow on a generic wing/body combination to: 1) choose a final wing for a future, highly instrumented model, 2) use the results to facilitate unsteady pressure sensor placement on the model, 3) determine the area to be surveyed with an embedded laser-doppler velocimetry (LDV) system, 4) investigate the primary juncture corner-flow separation region using particle image velocimetry (PIV) to see if the particle seeding is adequately entrained and to examine the structure in the separated region, and 5) to determine the similarity of observed flow features with those predicted by computational fluid dynamics (CFD). This report documents the results of the above experiment that specifically address the first three goals.					
15. SUBJECT TERMS					
16. SECURITY CLASSIFICATION OF:		17. LIMITATION OF ABSTRACT UU	18. NUMBER OF PAGES 124	19a. NAME OF RESPONSIBLE PERSON STI Help Desk (email: help@sti.nasa.gov)	
a. REPORT U	b. ABSTRACT U			c. THIS PAGE U	19b. TELEPHONE NUMBER (Include area code) (301) 621-0390
